HENRY'S LAW BEHAVIOR AND DENSITY FUNCTIONAL THEORY ANALYSIS OF ADSORPTION EQUILIBRIUM

by

Bryan Joseph Schindler

Dissertation

Submitted to the Faculty of the

Graduate School of Vanderbilt University

in partial fulfillment of the requirements

for the degree of

DOCTOR OF PHILOSOPHY

in

Chemical Engineering

December, 2008

Nashville, Tennessee

Approved:

Professor M. Douglas LeVan

Professor Peter T. Cummings

Professor G. Kane Jennings

Professor Eugene J. LeBoeuf

Professor Kenneth A. Debelak

To my parents

ACKNOWLEDGEMENTS

I would like to thank my advisor Dr. M. Douglas LeVan for all the time he spent helping and guiding me and keeping me on track. This work would not have happened without your help throughout.

I would like to thank Krista, Yu, Grant, and Joe and the rest of the people in the lab for all their help inside and outside of the lab over the years. For answering questions in the beginning, and distracting me when it was needed at the end. I also want to thank Trey Wince, B.J. Feuerhelm, Matt Garvey, and Mark and Emily Eberle for giving me a place to live during the last 6 months of my graduate experience.

I want to thank the US Army Edgewood Chemical and Biological Center for funding my research. In particular I would like to thank Leonard Buettner, John Mahle, David Tevault, Christopher Karwacki, and Tara Sewell for all of the help that they provided.

My deepest thanks go to Dr. Peter Cummings for help with the math and making sure that I maintained thermodynamic consistency. I also want to thank Dr. Clare McCabe for her help with SAFT, and also Dr. Maria Carolina dos Ramos for fitting the SAFT fluid parameters for nitrogen and n-pentane.

I would also like to thank the staff of the chemical engineering department. For answerering questions and trying to look out for my best interests, I want to thank Margarita Talavera and Mary Gilleran. Without the help from Mark Holmes, finishing my research would have been much more difficult.

Without the support and backing of my family none of this would have been possible. They were always there to listen and help in anyway that they could.

TABLE OF CONTENTS

LIST OF TABLES

LIST OF FIGURES

CHAPTER I

INTRODUCTION

Over the last few decades there has been an increased use of adsorption industrially in the separation of gases and liquids. One reason for this is the development and improvement of adsorption processes and materials. Adsorption can offer a more economically viable separation method for gases over other methods, such as cryogenic distillation. One of the reasons adsorption is gaining popularity as an alternative for separation is because of the diversity in adsorbent materials and how they operate at a variety of conditions. However, the large number of variables involved can make optimizing designs complex and require knowledge in a number of different aspects of adsorption.

Adsorption is used in many different types of processes. Some examples are bulk separation, gas storage, purification, and trace contaminant removal. Oxygen enrichment from air is an example of a bulk separation process. In the last few years there has been a increase in the amount of research done using adsorption for gas storage as a fuel supply for vehicular use. Specifically, the interest is in the ability to store large amounts of natural gas or hydrogen at moderate pressures and temperatures. Some examples of purification are the removal of by-products other than hydrogen from the process stream of the gas water shift reaction where carbon monoxide and water are reacted to form carbon dioxide and hydrogen, or the removal of nitrogen and carbon dioxide from a methane stream. Trace contaminant removal of impurities from a process stream is another common adsorption process that has seen an increase in interest, especially as part of a HVAC system.

All adsorption processes require knowledge of the two main separation mechanisms, equilibrium and kinetics, in order to achieve an effective design. When the

process is driven by the kinetics of the system the mechanisms can be steric, involving the exclusion of molecules based on size and shape, or by the differences in rate of adsorption and desorption. However, for most processes equilibrium factors are of primary concern. Equilibrium data in the form of adsorption isotherms gives the relative amounts that the adsorbent material can adsorb at a given pressure for single and multicomponent systems. Also the slopes of the isotherms in the regions of interest are important for design as they determine the regenerability of the solid adsorbent materials. Sets of isotherms at different temperatures allow the calculation of the isosteric heat of adsorption, which is important to the behavior of the system as it cycles between adsorption and desorption. Identifying the materials with the correct capacity, selectivity, and kinetics is extremely important to the design of an adsorption-based separation process.

Measurements of adsorption equilibrium and kinetics are achieved by a number of methods. The most commonly used methods for measuring adsorption equilibrium are volumetric and gravimetric. Volumetric methods fall into two different categories. In the first category, a known amount of adsorbate and adsorbent are introduced into a system of known volume and the resulting pressure is measured. This method works well for single component systems, but does not work as well for multicomponent systems. The second method of performing a volumetric experiment is by adding a gas chromatograph (GC) to the system allowing for an analysis of the gas phase. This setup works well for multi-component systems.

Gravimetric methods for measuring adsorption isotherms operate in a different manner. The loading of a sample in the system is measured by an accurate microbalance as adsorbate is introduced. Pressure is measured with a transducer.

However, both systems do not have the required accuracy to measure data into the Henry's law region except for light gases. The volumetric system is limited by the accuracy of the pressure transducer or by the lower limit of the detector on

the GC and the maximum volume injectable into the GC. Gravimetric systems are best reserved for single component systems. They are limited by the accuracy of the microbalance, typically 1.0 μg or 0.1 μg.

The kinetics of a system can be measured by a number methods. A commonly used method is the use of uptake curves from a gravimetric system; however, this method is not very accurate and cannot discriminate between mechanisms. Some of the newer methods are differential bed adsorption, zero-length column, and frequency response.

The ability to model complex systems accurately is a driving force behind adsorption research. It is desirous to have a model that can predict the behavior of single and multicomponent systems without having to do experiments, especially for systems that can be very dangerous or corrosive. In particular, it would be beneficial to have the model based on known parameters such as a Lennard-Jones diameter σ and well depth ϵ. A long term goal of adsorption theory is to be able to accurately predict adsorption equilibrium from first principles based on knowledge of the structure of the adsorbing molecule and the structure and composition of the adsorbent.

With the continual lowering of exposure levels to volatile organic compounds (VOCs) and toxic industrial compounds (TICs), the use of adsorption-based removal systems is receiving more attention as a viable option. However, there is scant data on most VOCs at and below the level that will be required to design these systems effectively. In many cases, adsorption isotherms will be required into the Henry's law region. An example of why data are needed is provided in Fig. 1.1, which shows two sets of hexane data[1,2] between saturation and 0.3 mol kg^{-1}. Also included are four different adsorption isotherms: group contribution theory,[3] virtual group theory,[4] Dubinin-Radushkevich (DR),[5] and the Toth equation.[6] There is considerable agreement between the data and the models over the range where there is data. How-

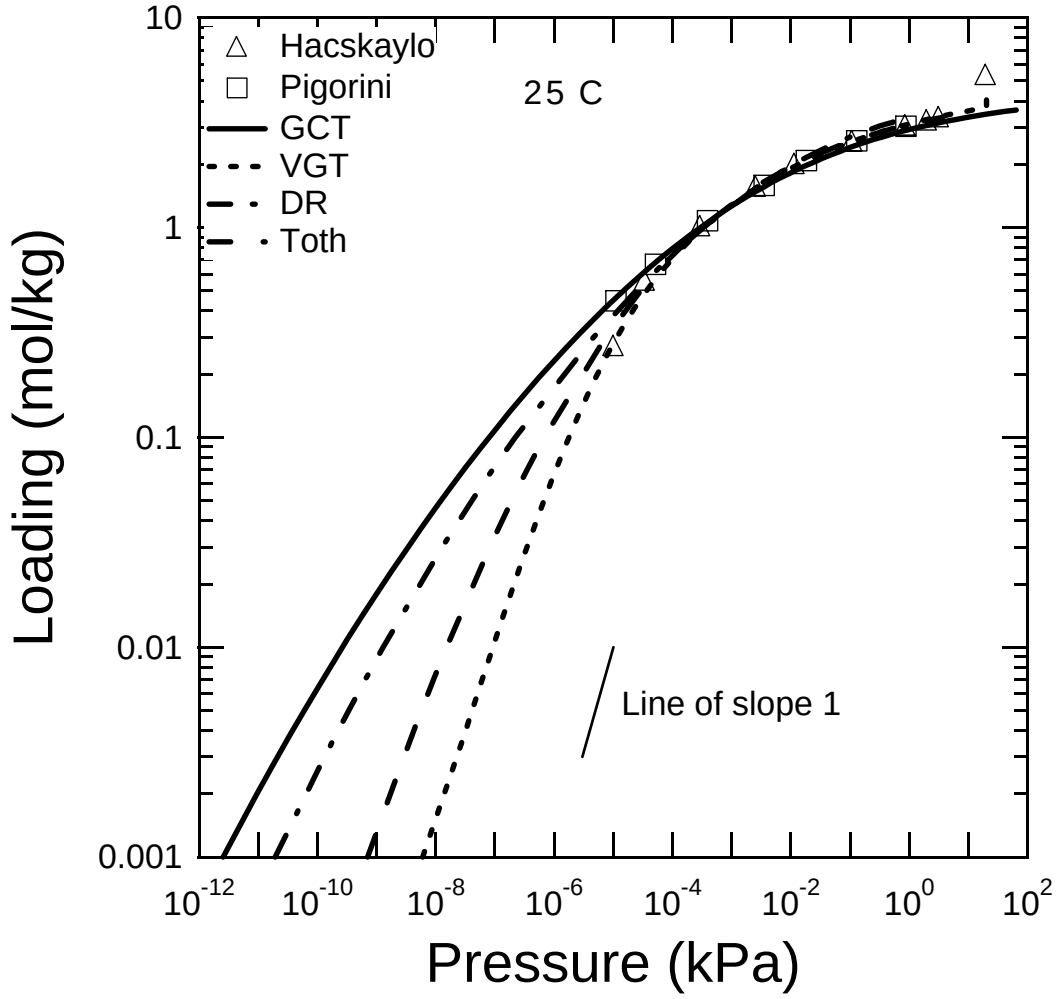

Figure 1.1: Isotherm of n-hexane on BPL activated carbon with the group contribution theory, virtual group theory, DR equation, and the Toth equation.

ever, when the isotherm is extended to lower loadings there is considerable spread between the predicted pressure of the models. If these models were used to design an adsorption filtration device for the removal to ultra-low concentrations there would be considerable differences between the four models. This demonstrates the need for adsorption data at much lower concentrations to determine which model, if any, is correct.

In Chapter II we discuss the development of a novel method for preparing samples at known loadings and analyzing these samples, which reach into the Henry's law region. Samples were prepared at loadings from 1.0 down to 0.0001 mol kg^{-1} for n-pentane on BPL activated carbon. The samples from 1.0 to 0.01 mol kg^{-1} were prepared using a liquid injection system. The samples below 0.01 mol kg^{-1} were prepared with a gas injection system. After a sample was prepared with either method it was sealed and allowed to come to equilibrium at an elevated temperature. The samples were then analyzed using a purge and trap method. Adsorption isotherms were measured over a wide range of temperatures, from 0 to 175 °C at constant loading, using a novel apparatus that concentrates the gas phase of n-pentane from a large volume to a much smaller volume. The measured data are used to analyze the behavior of three different adsorption isotherms, the DR equation, the Langmuir equation, and the Toth equation. We will discuss how these theories describe the data as they transition into the Henry's law region. The isosteric heat of adsorption is calculated and discussed as a function of the loading. This is the first time adsorption equilibrium has been measured in the Henry's law region for an adsorbate that is a liquid at room temperature.

In Chapter III the isosteric heat of adsorption in the Henry's law region is calculated as a function of pore width for a variety of gases. These values are compared with the isosteric heat of adsorption calculated from adsorption isotherms. These data, and specifically the maximum value, are important in the design of new mate-

rials. The isosteric heat of adsorption, in the Henry's law region in particular, gives important information about mechanisms and properties of adsorption. When designing a new material, especially if it is for a specific process, knowing which pore sizes to emphasize or avoid can be very helpful. In the design of a trace contaminant removal system you would want a system with pores as close as possible to the pore size that gives the maximum isosteric heat of adsorption. This would provide the system with the maximum amount of retention of the contaminants. However, if you are designing a pressure swing adsorption system a low isosteric heat of adsorption would be preferable to reduce heat effects and allow more efficient regeneration. In gas storage, heat of adsorption can be used as a screen to eliminate materials that would not reach the desired deliverable capacity because of overheating during vessel charging and overcooling during vessel discharge. The use of knowledge of the isosteric heat of adsorption in the Henry's law region in the initial design of new materials will allow for more targeted development to specific problems, which will result in more effective materials.

The ability to predict adsorption isotherms using fundamental information about the adsorbate and adsorbent is an important research goal. In Chapter IV, density functional theory (DFT) is modified to allow the modeling of chain molecules using the statistical associating fluid theory (SAFT) equation of state. This will be the first time that a mean-field for the first order attractive term is not assumed, and it is also the first time that the second order term is included. DFT has been widely used to model the adsorption of spherical molecules in parallel or cylindrical pores. By changing the equation of state from a spherical to SAFT we are able to model the behavior for a much larger array of molecules. This allows us to predict adsorption behavior given the bulk parameters, the interaction of the adsorbate molecule with graphite, and the pore size distribution of the adsorbent.

Parameters were estimated to describe the bulk behavior and the interaction

with a carbon wall for nitrogen and n-pentane. Density profiles for nitrogen show the adsorption behavior of nitrogen in a variety of pore sizes at different pressures. The monolayer transition, capillary condensation, and the freezing transition are discussed. This is the first time, that we are aware of, that such a sharp freezing transition is demonstrated. The density profiles are used to calculate a pore size distribution for BPL activated carbon. Density profiles were then calculated for n-pentane. Using the density profiles and the calculated pore size distribution, an isotherm for n-pentane was determined.

In Chapter V, the conclusions from this work are summarized. Also included are recommendations for follow up work that result from this dissertation.

References

[1] Hacskaylo JJ. Thermodynamic Studies of Vapor-Solid Adsorption Equilibria. Charlottesville VA USA, University of Virginia , Ph.D. thesis, 1987.

[2] Pigorini G. Periodic Behavior of Pressure Swing Adsorption Cycles and Coadsorption of Light and Heavy n–alkanes on Activated Carbon. Charlottesville VA USA, University of Virginia , Ph.D. thesis, 2000.

[3] Walton KS, Pigorini G, and LeVan MD. Simple group contribution theory for adsorption of alkanes in nanoporous carbons. Chem. Eng. Sci. 2004: 59:(4425–4432)

[4] Ding Y. Periodic adsorber optimization and adsorption equilibrium measurement and prediction. Nashville TN USA, Vanderbilt University , Ph.D. thesis, 2002.

[5] Ye XH, Qi N, Ding YQ, LeVan MD. Prediction of Adsorption Equilibrium using a Modified D-R Equation: Pure Organic Compounds on BPL Carbon. Carbon 2003; 41:681–686

[6] Do DD. Adsorption Analysis: Equilbria and Kinetics. London: Imperial College Press; 1998

CHAPTER II

TRANSITION TO HENRY'S LAW IN ULTRA-LOW CONCENTRATION ADSORPTION EQUILIBRIUM FOR N-PENTANE ON BPL ACTIVATED CARBON

2.1 Introduction

The use of adsorption for the removal of volatile organic compounds (VOCs) and toxic industrial chemicals (TICs) has drawn considerable attention in recent years. With rising health concerns leading to the continual lowering of allowable exposure levels for VOCs and TICs, the use of microporous adsorbent materials to remove these chemicals will increase. To design air filters to remove ultra-low concentrations of contaminants, adsorption equilibrium data will be required at lower concentrations than are currently available, including into the Henry's law region. Also, contaminants bleed through filters receiving occasional exposures to VOCs and TICs, and low concentration adsorption equilibrium is necessary to analyze this process accurately. However, standard volumetric and gravimetric methods do not have the sensitivity necessary to obtain these measurements, especially for low-vapor pressure compounds, e.g., chemicals that are liquids at room temperature and pressure.

Most adsorption data at low concentrations are measured by either gravimetric or volumetric methods. Foster *et al.*,[1] Pinto *et al.*,[2] and Kuro-Oka[3] used a gravimetric method to measure adsorption of light and heavy gases on activated carbons. See Table 2.1 for details. The resolution of gravimetric methods is limited by the accuracy of the microbalance, which is typically 1.0 μg or 0.1 μg.

The volumetric method has also been used extensively. Eissmann and LeVan,[4] Kaul,[5] Mahle *et al.*,[6] Russell and LeVan,[7] Karwacki and Morrison,[8] Pigorini,[9–11] Zhu *et al.*[12,13] and many others have measured adsorption equilibria for high-vapor pressure gases on activated carbons. Golden and Kumar[14] measured trace concentrations

Table 2.1: Previously measured low concentration data by descending pure component vapor pressure of chemical

Adsorbate	Adsorbent	Lowest pressure (kPa)	Lowest loading (mol/kg)	Reference
Methane	BPL	2.0	0.012	9
	KF-1500	0.4	0.034	3
	Kureha beads	18.5	0.04	5
Ethene	Kureha	2.5×10^{-3}	0.25	13
	Kureha beads	2.3	0.095	5
SF_6	Kureha	0.004	0.5	12
Ethane	BPL	0.18	0.28	7
	BPL	0.6	0.026	9
	Kureha	1.5×10^{-3}	0.25	13
	Norit R3	2.1	0.38	22
	Ajax	1.6	0.17	21
	KF-1500	0.0007	0.003	3
	Kureha beads	0.55	0.11	5
Trichloroethylene	BPL	4.5×10^{-6}	0.027	24
	A10	9.0×10^{-6}	0.09	24
Propene	Kureha	4.0×10^{-3}	0.2	13
	BPL	107	0.003	14
	Kureha beads	0.0011	0.007	5
R-22	BPL	6.9×10^{-4}	0.0055	6
Propane	BPL	9.7×10^{-4}	0.12	7
	Kureha	3.0×10^{-3}	0.2	13
	Norit R3	0.022	0.17	22
	Ajax	1.0	0.6	15
	Kureha beads	0.34	0.12	5
R-134a	BPL	3.8×10^{-4}	0.007	8
R-12	BPL	67	0.008	14
	BPL	0.21	0.24	8
$C_3H_3F_5$	BPL	0.0017	0.085	8
C_4F_8	BPL	1.5×10^{-4}	0.014	8
	BPL	2.3×10^{-5}	0.0026	6
n-Butane	BPL	0.001	0.22	1
	BPL	34.7	0.02	14
	Kureha	0.002	0.5	12
	Ajax	2.7	0.63	21
R-11	BPL	2.3×10^{-4}	0.0088	6
	BPL	5.8×10^{-4}	0.14	8
Methylene Mhloride	BPL	21.67	0.59	14
n-Pentane	Ajax	1.6	0.83	21
	Ajax	0.5	0.6	15
	KF-1500	0.0003	0.197	3
Dichloromethane	BPL	2.9×10^{-4}	0.266	4
	BPL	4.0×10^{-4}	0.031	24
	A10	10×10^{-3}	0.15	24
1,1,1-Thichloroethane	BPL	7.9×10^{-6}	0.024	24
1,1,2-Trichloro-1,2,2-Trifluoroethane	BPL	1.5×10^{-4}	0.186	4
	BPL	1.9×10^{-5}	0.013	6
$C_5H_2F_{10}$	BPL	3.4×10^{-4}	0.16	8
Acetone	BPL	0.001	0.086	1
	BPL	2.0×10^{-4}	0.16	16
	BPL	8.4	0.14	14
	A10	1.4×10^{-4}	0.07	24
n-Hexane	BPL	1.0×10^{-5}	0.27	16
	BPL	5	0.77	14
	Norit R3	1.6×10^{-3}	0.72	22
Methanol	BPL	1.4×10^{-2}	0.77	18
	BPL	3.8×10^{-4}	0.02	24
	A10	5.4×10^{-3}	0.05	24
Carbontetrachloride	BPL	2.2×10^{-5}	0.023	24
Benzene	BPL	0.0057	1.79	1
	BPL	3.0×10^{-6}	0.012	24
	A10	2.0×10^{-5}	0.26	24
	Carbon Fiber	3.6×10^{-3}	.719	17
	Ajax	0.1	0.3	15
Methyl Ethyl Ketone	BPL	2.1×10^{-5}	0.27	19
Ethanol	BPL	6.8×10^{-3}	0.81	18
Toluene	BPL	1.45	1.1	14
	BPL	1.1×10^{-6}	0.32	19
	BPL	6.6×10^{-5}	1.1	24
	RB3			2
	Carbon Fiber	3.5×10^{-3}	1.47	17
Propanol	BPL	0.018	2.1	18
Methyl Isobutyl Ketone	BPL	7.3×10^{-7}	0.38	19
Ethyl Benzene	RB3		1.0	2
Butanol	BPL	0.048	2.0	18
2-Hexanol	BPL	8.0×10^{-6}	0.2	25
Isopropyl Methylphosphonofluoridate	CSC	8.4×10^{-7}	0.07	26

of high and low vapor pressure gases in a carbon dioxide stream. Do and Do[15] measured adsorption isotherms for both low and high vapor pressure gases. Rudisill *et al.*,[16] Yun *et al.*,[17] Taqvi *et al.*,[18] Qi and LeVan,[19] and others have measured adsorption equilibria for low-vapor pressure gases on activated carbons, with the lowest pressures and loadings given in Table 2.1.

Other methods for measuring adsorption isotherms have also been used. Yang *et al.*[20] used temperature programmed desorption to estimate an adsorption isotherm for dioxins on activated carbon. Mayfield and Do[21] used a differential adsorption bed to measure isotherms for ethane, butane, and pentane on Ajax activated carbon. Linders *et al.*[22] used head space gas chromatography to measure nitrogen, ethane, propane, and hexane isotherms on Norit R3. Himeno and Urano[23] and Himeno and Kohei[24] used headspace gas chromatography for benzene, dichloromethane, trichloroethylene, carbon tetrachloride, 1,1,1-trichloroethane, and methanol on BPL, CQS, and A10 carbons. Karwacki *et al.* [25] used a purge and trap method to measure 2-hexanol equilibrium on BPL carbon. Karwacki *et al.* [26] also measured isotherms for isopropyl methylphosphonofluoidate (GB) on a coconut-based activated carbon using the same method.

Prior measurements of low limits for adsorption equilibrium of VOCs can be indicated in terms of pressure or loading. From Table 2.1, the lowest pressure measured previously for a high-vapor pressure VOC, obtained by Himeno and Kohei[24] for trichloroethylene on BPL carbon, is 4.5×10^{-6} kPa and for a low-vapor pressure VOC, measured by Qi and LeVan[19] for methyl isobutyl ketone on BPL carbon, is 7×10^{-7} kPa. The lowest loading previously measured for a high-vapor pressure gas, obtained by Mahle *et al.* [6] for R-318 on BPL carbon, is 0.0026 mol kg^{-1} and for a low-vapor pressure gas, reported by Himeno and Kohei[24] for benzene on BPL carbon, is 0.012 mol kg^{-1}.

Measuring adsorption data in the Henry's law region has been difficult. There

have been reported instances where Henry's law was achieved for light gases. For example, Pigorini[9] measured data into the Henry's law region for methane and ethane on BPL activated carbon. Eissmann and LeVan[4] reached the Henry's law region for R-113 and approached Henry's law for dichloromethane on BPL activated carbon. Kaul[5] measured methane, ethane, ethene, and propene on Kureha beads into the Henry's law region. Mahle[6] achieved Henry's law for R-22 and approached Henry's law for R-318 on BPL activated carbon. There are no reported cases of adsorption of low-vapor pressure gases in the Henry's law region.

In this paper, we use a purge and trap method to extend the lower limits of adsorption equilibria into the Henry's law region for a low-vapor pressure gas. We propose new methods to prepare pre-equilibrated samples at known loadings from 1.0 to 0.0001 mol kg^{-1}. To analyze the samples we use the method described by Karwacki *et al.*[26] The adsorption isotherms will be compared with the Dubinin-Radushkevich (DR) equation, the Langmuir equation, and the Toth equation. The transition into the Henry's law region will be discussed for each of the theories. The isosteric heat of adsorption will also be evaluated and discussed. To our knowledge this is the first report of adsorption equilibrium being measured into the Henry's law region for a low-vapor pressure gas.

2.2 Experiments

Materials

The activated carbon used in these experiments was type BPL (Calgon Carbon Corp., Lot No. 4814-J) in 40 × 50 mesh. The adsorbate was n-pentane (HPLC Grade, 99% min). The adsorbents used in the thermal desorption unit were Carbotrap™ Graphitized Carbon Black in 20 × 40 mesh in the sample tube and Carbopack™ X in 20 × 40 mesh in the focusing trap.

Sample Preparation

For these experiments, pre-equilibrated samples were prepared at known loadings. The methods used to prepare these samples involved a liquid injection or a gas injection into an evacuated glass ampule containing regenerated carbon. The liquid injection system was used for samples with loadings greater than or equal to 0.01 mol kg^{-1}, while the gas injection system was used for samples with loading less than or equal to 0.01 mol kg^{-1}. Samples were prepared by both methods at a loading of 0.01 mol kg^{-1} to verify that the injection methods were equivalent.

BPL activated carbon was regenerated at 200 °C with a helium purge at a flow rate of 0.5 L min^{-1} for at least 8 h. Then, approximately 2 g of carbon was placed in a pre-numbered, pre-weighed glass ampule and weighed. The ampules were then connected to a dosing apparatus for liquid or gas injection.

A diagram of the dosing apparatus used to prepare a sample by liquid injection is shown in Figure 2.1a. The ampule was connected, heated to 150 °C, and placed under vacuum for eight hours to regenerate the sample a second time. A rotary-vane vacuum pump was used to achieve a vacuum of approximately 0.05 mbar. The ampule was removed from the heat, placed in an ice bath, and the valve shown in Figure 2.1a was closed, removing the sample from the vacuum. A syringe was used to inject a known amount of adsorbate into the ampule. The syringe was weighed before and after injection to determine the mass injected. The glass ampule was then sealed with a micro-torch and weighed with waste glass for calculation of the mass of adsorbent.

A diagram of the gas dosing system used to prepare samples at the lowest loadings is shown if Figure 2.1b. Instead of injecting liquid with a syringe, a saturated vapor was generated and injected using a gas sampling loop. To accomplish this, the ampule was connected to the apparatus, heated to 150 °C, and placed under vacuum for eight hours to regenerate it a second time as described above. The temperature of the temperature bath shown in Figure 2.1b and the size of the sample loop were

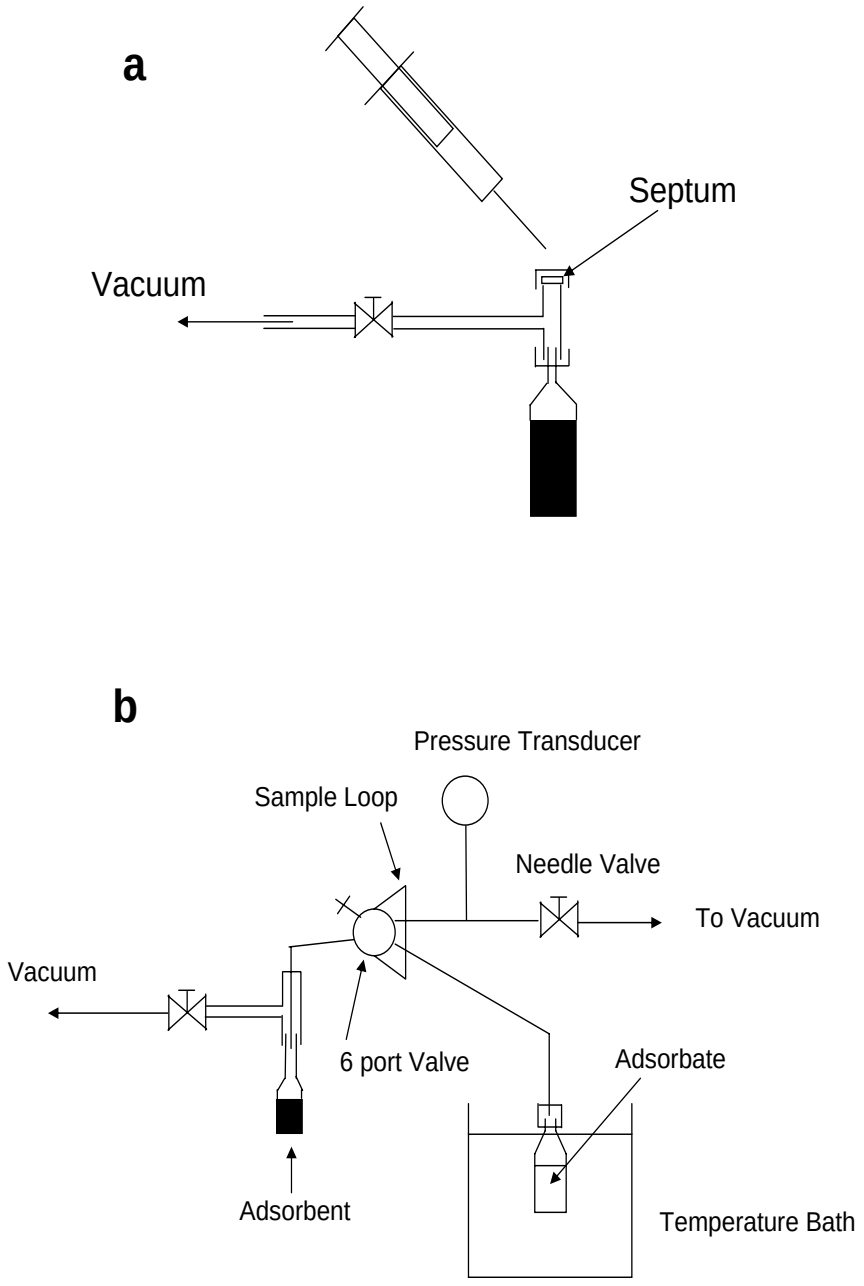

Figure 2.1: Schematic of the sample preparation apparatus: (a) liquid injection and (b) gas injection.

determined by the desired loading with minimums of –4.0 °C and 25 μl used for the lowest loading. A vacuum was connected to the adsorbate vapor generator to remove any impurities (e.g., dissolved gases) from the system, and the pressure transducer was used as a check on the vapor pressure. When the adsorbate was at the expected vapor pressure, the adsorbent sample was removed from the vacuum and was placed in an ice bath. The six-port valve was switched, thereby isolating the loop from the vapor generating side and exposing the adsorbent to the n-pentane vapor. The ampule was then sealed with the micro-torch and weighed with waste glass to determine the mass of adsorbent used.

After a sample had been prepared by the methods described above, the sealed glass ampule was leak tested by submerging it in water. Ampules were then strapped to a ferris wheel arrangement in an environmental chamber, heated to 150 °C, and rotated end-over-end at 4 rpm for days to months to increase the mixing of the solid and gas phases as equilibrium was established.

Purge and Trap Apparatus

A diagram of the apparatus used to analyze the equilibrated samples is shown in Figure 2.2. The adsorption bed was placed inside an environmental chamber (Thermotron SE-300-2-2) to control the temperature of the sample. A mass flow controller was used to set the flow rate of nitrogen carrier gas through the sample. As the carrier gas flowed through the sample in the adsorption bed, the adsorbate in the gas phase was removed from the small fixed bed. A nitrogen bypass line was created by use of the open tee, which maintained the pressure in the system. The bypass line was set at a flow rate such that there was always a positive flow out of the open tee, keeping the system clean of any impurities.

The carrier gas containing n-pentane vapor flowed into the thermal desorption unit (Dynatherm model ACEM 900), which has two adsorption beds in series, the

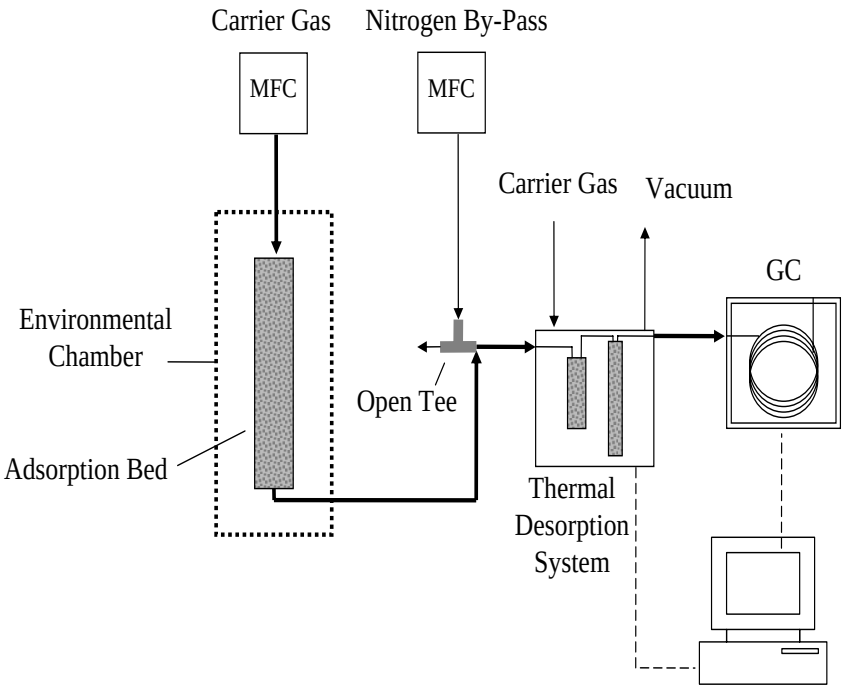

Figure 2.2: Schematic of the apparatus to analyze the samples.

sample tube and the focusing trap. The materials for these adsorption beds were chosen to remove the n-pentane from the gas phase at room temperature and release the n-pentane at high temperature. The n-pentane is first adsorbed in the sample tube, which is then heated to pass the n-pentane in a more concentrated gas into the focusing trap. Heating the focusing trap concentrates the n-pentane further for analysis. The quantity of n-pentane collected in the thermal desorption unit was determined using a gas chromatograph (HP 5890A series II) with a flame ionization detector.

Operating Procedure

The overall procedure to analyze an equilibrated sample was similar to the method described by Karwacki *et al.*[26] The glass ampule containing the equilibrated sample was opened. The sample was placed in the desorption column with plugs of glass wool used before and after the bed. When the ampule was opened, it was exposed to air for a brief period of time. This is not believed to change the results significantly because the transfer was done quickly, and any trace adsorption of water would be predominantly around oxide sites, while the n-pentane is adsorbed on carbonaceous sites.[7,16] The flow rate of the carrier gas was set at 50 cm^3 min^{-1} for most samples. For samples at high temperatures the flow rate was reduced to flow rates as low as 1 cm^3 min^{-1}. Checks were performed when the flow rate was changed to insure that the effluent concentration was not flow rate dependent, i.e., that it was the equilibrium value. At high concentrations and high temperatures the carrier flow rate was shut off between runs to minimize the amount of n-pentane flushed from the system. The carrier gas flow was restarted and allowed to stabilize before the start of the next run.

The n-pentane partial pressure for each run was calculated using the ideal gas law. The mass of n-pentane collected by the thermal desorption unit was calculated

from the chromatograph signal. The volume of carrier gas containing the n-pentane was calculated from the carrier gas flow rate, the length of time of the experiment, and was adjusted for the temperature of the experiment. The temperature was set by the environmental chamber.

Each ampule was used to measure the partial pressure over the entire temperature range. The system was first cooled to 0 °C and held until the temperature and gas-phase concentration of n-pentane were constant. A minimum of three experiments were run at each temperature with varying volumes passed through the bed to determine the fluid-phase concentration. This was preformed to show that the fluid-phase concentration was stable and that there was no breakthrough of the adsorbent beds in the thermal desorption unit. The temperature was increased in 25 °C increments, and the procedure was repeated up to a temperature of 175 °C. The amount of adsorbate desorbed during each experiment was calculated as a percent of the initial loading, and the average amount desorbed for all ampules was 1.4%, with 80% of this occurring at 150 °C and 175 °C. This illustrates that the loading does not change significantly over the course of all experiments.

Key to these experiments was the fluid-phase concentration remaining constant, i.e., that the mass transfer zone did not leave the bed throughout the length of the experiment. According to local equilibrium theory, for a uniformly loaded bed, the break from the initially uniformly saturated plateau (i.e., the point where this plateau joins the gradual wave tail) is described by[27]

$$\frac{\tau}{\zeta} = \rho_b \frac{dn}{dc} \tag{2.1}$$

where τ is the number of superficial column volumes, ζ is the non-dimensional bed length, and $\rho_b = 480$ kg m^{-3} is the bulk packing density of the adsorbent. To determine the number of column volumes that can be passed through the bed before the concentration in the head space changes, eq. 2.1 was evaluated at the outlet of the bed, $\zeta = 1$. We examine two different cases, which represent extremes. First, we

consider a loading of 0.0001 mol kg^{-1} and temperature of 25 °C. If the Toth equation, which is described later, is used for the isotherm, the number of column volumes that can be passed through the bed before the effluent concentration declines is $\tau = 2.9\times10^8$. Thus, the system at low concentrations and low temperatures was stable at flow rates of 50 cm^3 min^{-1}, well beyond any times involved in the experiments.. Second, we consider a loading of 0.97 mol kg^{-1} and temperature of 175 °C, for which the time for elution of the constant concentration was the shortest. Eq. 2.1 for this case gives $\tau = 460$. With the carrier gas turned off between runs, this is greater than the number of column volumes that we passed through the bed. We never observed a decrease in effluent concentration because of depletion of the adsorbate.

2.3 Results and Models

Adsorption equilibrium of n-pentane

Adsorption isotherms for n-pentane were measured in 25 °C increments from 0 to 175 °C. All of the experimental data are summarized in Table 2.2. To emphasize different aspects of the data, they are plotted in two different ways. First, the data are shown in Figure 2.3a as an adsorption isotherm (n vs. p) using the Toth equation. Then, the data are shown in Figure 2.3b using a Henry's law plot (n/P vs. n). For this plot, when the isotherm is in the Henry's law region, the slope is zero and the y-intercept is the Henry's constant. Of major interest in this plot, which could not be predicted from existing isotherm equations, is that the transition into the Henry's law region occurs for all temperatures near the same n-pentane loading of 0.01 mol kg^{-1}. The approach to the Henry's law regime occurs asymptotically, but at a loading of 0.01 mol kg^{-1}, the asymptotic behavior is clear from the data. There are multiple data points at all of the low concentrations, corresponding to different replicates of ampules used. For a given temperature, most of the data points at 0.0001 mol kg^{-1} were indistinguishable from one another, as were the data at 0.030 mol kg^{-1}.

Table 2.2: Experimental data for adsorption of n-pentane on BPL activated carbon

Loading	Pressure (kPa)							
(mol/kg)	$T = 0$ °C	$T = 25$ °C	$T = 50$ °C	$T = 75$ °C	$T = 100$ °C	$T = 125$ °C	$T = 150$ °C	$T = 175$ °C
0.97	3.70×10^{-4}	3.50×10^{-3}	2.01×10^{-2}	9.26×10^{-2}	3.79×10^{-1}	1.06	2.96	6.37
0.35	1.14×10^{-5}	1.16×10^{-4}	8.65×10^{-4}	4.58×10^{-3}	1.96×10^{-2}	6.93×10^{-2}	2.32×10^{-1}	6.58×10^{-1}
0.093	4.47×10^{-7}	5.84×10^{-6}	4.48×10^{-5}	2.80×10^{-4}	1.37×10^{-3}	5.23×10^{-3}	1.67×10^{-2}	4.38×10^{-2}
0.030	4.24×10^{-8}	5.58×10^{-7}	5.32×10^{-6}	3.64×10^{-5}	2.00×10^{-4}	8.62×10^{-4}	3.10×10^{-3}	9.31×10^{-3}
0.030	3.53×10^{-8}	6.21×10^{-7}	5.41×10^{-6}	3.64×10^{-5}	1.98×10^{-4}	8.58×10^{-4}	3.03×10^{-3}	8.91×10^{-3}
0.014	1.10×10^{-8}	1.73×10^{-7}	1.79×10^{-6}	1.32×10^{-5}	7.48×10^{-5}	3.34×10^{-4}	1.18×10^{-3}	3.72×10^{-3}
0.013	7.85×10^{-9}	1.04×10^{-7}	1.05×10^{-6}	7.59×10^{-6}	4.25×10^{-5}	1.93×10^{-4}	7.42×10^{-4}	2.34×10^{-3}
0.01		5.99×10^{-8}	6.63×10^{-7}	4.29×10^{-6}	4.69×10^{-5}	2.33×10^{-4}	8.25×10^{-4}	2.51×10^{-3}
0.001		8.80×10^{-9}	9.66×10^{-8}	7.17×10^{-7}	4.12×10^{-6}	1.80×10^{-5}	6.50×10^{-5}	1.91×10^{-4}
0.0001		4.73×10^{-10}	5.04×10^{-9}	5.59×10^{-8}	2.94×10^{-7}	1.38×10^{-6}	6.17×10^{-6}	1.85×10^{-5}
0.0001		4.81×10^{-10}	5.29×10^{-9}	5.05×10^{-8}	2.90×10^{-7}	1.35×10^{-6}	5.09×10^{-6}	1.57×10^{-5}

The samples at 0.013 and 0.014 mol kg^{-1} were prepared with a liquid injection and show some inaccuracy. Each data point in Table 2.2 is the average of three different experimental runs with the same sample where different volumes of the carrier gas were used. The average standard deviation on n-pentane partial pressure for all of the data points is less than two orders of magnitude lower than the data point for all but one point.

In the next three subsections, we will describe the data using three different adsorption isotherm models. A good objective function to fit the Henry's law data is

$$e_1 = \sum_m \left[\ln\left(\frac{n_m^{cal}}{p_m^{exp}}\right) - \ln\left(\frac{n_m^{exp}}{p_m^{exp}}\right) \right]^2 \tag{2.2}$$

where n_m^{exp} is the experimental loading, m is the number of data points, n_m^{cal} is the calculated loading, and p_m^{exp} is the experimental pressure. It should be noted that eq (2.2) is exactly equivalent to

$$e_2 = \sum_m \left(\ln n_m^{cal} - \ln n_m^{exp} \right)^2 \tag{2.3}$$

The model parameters were fit by minimizing eq. (2.3).

The adsorption isotherms were measured with nitrogen as the carrier gas, which adsorbs to a small extent. The Henry's law constant is therefore

$$K_{\text{pentane}} = \left. \frac{\partial n}{\partial P_{\text{pentane}}} \right|_{P_{\text{pentane}} \to 0} \tag{2.4}$$

which depends on the nitrogen pressure, i.e., $K_{pentane} = K_{pentane}(P_{N_2})$.

An ideal adsorbed solution theory[28] calculation was performed to determine the influence of the adsorbed nitrogen at 25 °C. The pure component nitrogen isotherm was taken from Meredith and Plank.[29] At n-pentane loadings of 0.0001 mol kg^{-1}, for every n-pentane molecule in the gas phase there are approximately 2×10^{11} nitrogen molecules, and approximately 4000 nitrogen molecules adsorb for every adsorbed n-pentane molecule. For a given adsorbed-phase loading of n-pentane, the effect of adsorbed nitrogen will be to raise the partial pressure of n-pentane. We estimate that

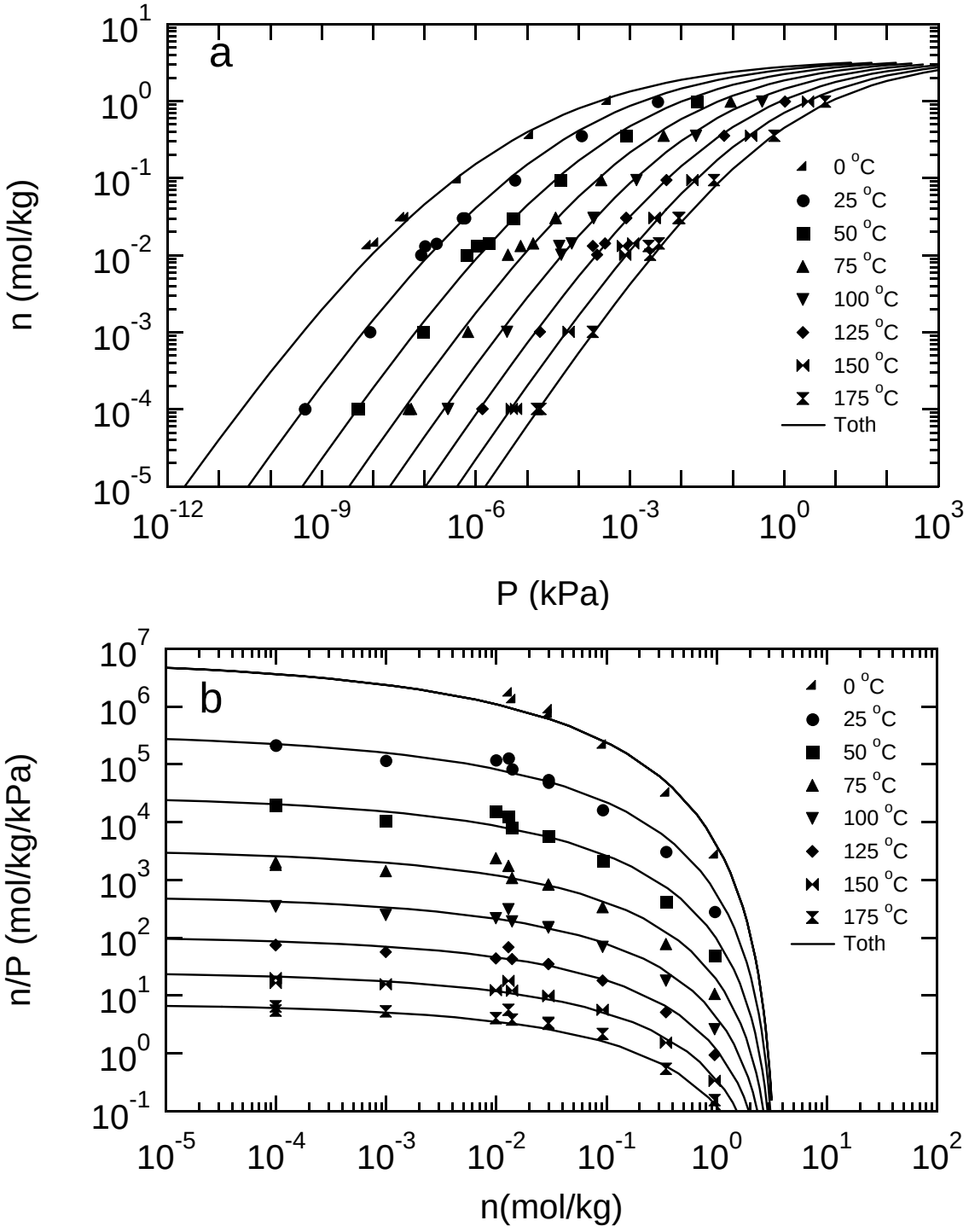

Figure 2.3: n-Pentane on BPL activated carbon with the Toth equation: (a) isotherm and (b) Henry's law plot.

the Henry's law slope approached at the left edge of Figure 2.3b for 25 °C is approximately one twenty-fifth of what it would be with no coadsorption of nitrogen. The use of nitrogen as a carrier gas corresponds to a practical problem, i.e., the adsorption of an ultra-low concentration contaminant from a weakly adsorbing carrier gas, such as dry air.

Dubinin–Radushkevich (DR) Equation

The DR equation,[30] like the more general Dubinin–Astakov equation, is a well known adsorption isotherm model. It fits data very well for many different adsorbates,[1,2,6,14,17,22–24] but does not have a proper Henry's law limit, as is well known. Nevertheless, its deviation from experimental results at low loadings has not been shown. The DR equation is represented by

$$n = \frac{V_o}{V_m} \exp\left[-\left[\left(\frac{RT}{\beta E_o} \right) \ln\left(\frac{P_s}{P} \right) \right]^2 \right] \tag{2.5}$$

where P_s is the saturated vapor pressure, V_m is the saturated liquid molar volume of the adsorbate at temperature T. The scaling constant $\beta = 0.79$ and the characteristic adsorption energy for a reference vapor $E_o = 26{,}500$ J mol^{-1} were obtained using the objective function in eq (2.3), and the maximum active volume in the adsorbent that the adsorbate can occupy was $V_o = 481.1$ cm^3 kg^{-1}, which was obtained from previous work.[30]

The DR equation is plotted in Figure 2.4a. It fits the data well for temperatures below 100 °C and loadings above 0.01 mol kg^{-1}. Below this loading the DR equation over predicts the pressure for high temperatures and under predicts the pressure at low temperatures.

The DR equation fails in the limit of the pressure approaching zero, where the slope of the isotherm incorrectly approaches zero. This can be seen in Figure 2.4, in which the DR equation and the data in the Henry's law region are plotted. Since the DR equation does not have proper Henry's law behavior, the curve goes through a

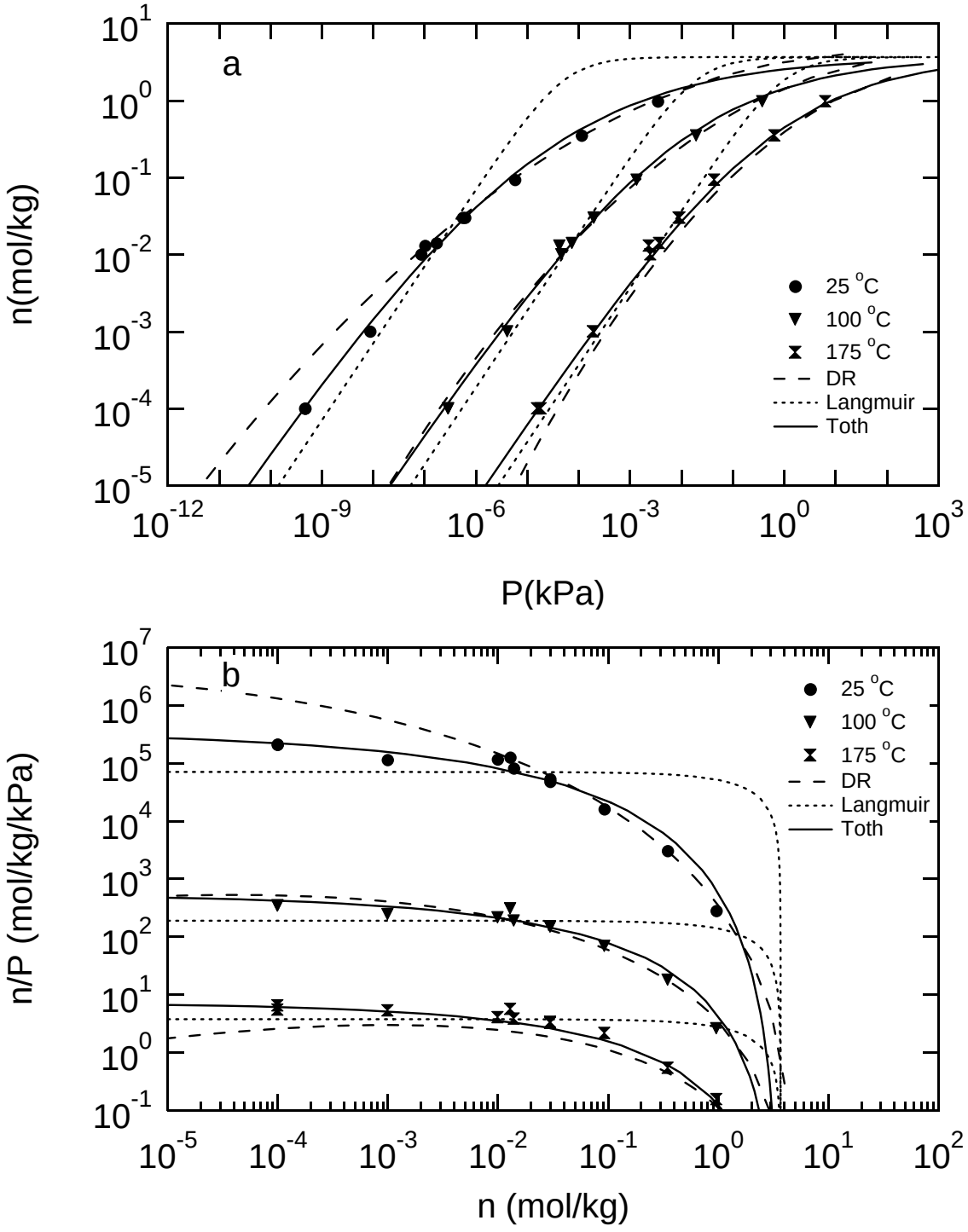

Figure 2.4: n-Pentane on BPL activated carbon with the DR, Langmuir, and Toth equations: (a) isotherm and (b) Henry's law plot.

maximum. This behavior can be seen to shift to higher loadings at higher temperatures, becoming very pronounced at 175 °C and loadings below 0.01 mol kg^{-1}. For lower temperatures the DR equation has not yet gone through a maximum.

Langmuir Equation

The Langmuir equation was developed for a homogeneous surface, where the adsorption is localized, but is used more broadly. The equation is[31]

$$n = \frac{n_o b P}{1 + bP} \tag{2.6}$$

with

$$b = b_o \sqrt{T} \exp\left(Q/RT\right) \tag{2.7}$$

where n_o is the saturation loading, and Q is the isosteric heat of adsorption at zero loading. The parameters for the Langmuir equation are given in Table 2.3 and were obtained using the objective function. The Langmuir equation has a proper Henry's law region where the Henry's constant is $K_H = n_o b$. The saturation loading for n-pentane was set to 3.68 mol kg^{-1} based on previous work.[30]

The Langmuir equation is plotted with the data in Figure 2.4a. It is readily apparent that it does not fit the data well. BPL activated carbon is a heterogeneous material, and the Langmuir equation does not describe the data over the wide range of the measurements.

The Henry's law plot for the Langmuir equation is shown in Figure 2.4b. The equation shows the Henry's law region being entered at all temperatures near 1 mol kg^{-1}, based on the parameters regressed from the objective function. However, there is wide disagreement with the data.

Toth Equation

The Toth equation is a well known isotherm equation that was developed for heterogeneous materials. We use the multi-temperature Toth equation[32] in the form

$$n = \frac{n_s b P}{[1 + (bP)^t]^{(1/t)}} \tag{2.8}$$

where the saturation loading is

$$n_s = n_o \exp\left[\chi(1 - T/T_o)\right] \tag{2.9}$$

with

$$b = b_o \exp\left(Q/RT\right) \tag{2.10}$$

and

$$t = t_o + \alpha(1 - T_o/T) \tag{2.11}$$

with T_o = 298.15 K. The Toth equation, like the Langmuir equation, has a proper Henry's law limit and a finite saturation loading. The parameters obtained by regression are shown in Table 2.3. The saturation loading was fixed at 3.68 mol kg^{-1} for the same reason as described for the Langmuir equation. The saturation loading is a very weak function of temperature, and the parameters b and t are strong functions of temperature.

The Toth equation is shown with all of the data in Figure 2.3 where it fits the data reasonably well over a wide range of loadings and temperatures. Figure 2.4 shows the Toth equation in comparison with the DR and Langmuir equations. The Toth equation overcomes the shortcomings of the DR and Langmuir equations for this system – a proper Henry's law slope and the transition from Henry's law toward non-linear adsorption, respectively. For all temperatures, the Toth equation enters the Henry's law region at loadings near 0.01 mol kg^{-1}.

The measured isotherms were used to calculated the isosteric heat of adsorp-

tion using the thermodynamic relationship

$$\Delta H_a = -R \left. \frac{\partial \ln P}{\partial (1/T)} \right|_n \tag{2.12}$$

Figure 2.5 shows $\ln P$ plotted versus $1/T$ at constant n with the Toth equation and the vapor pressure of n-pentane. The values of the isosteric heat for specific loadings are shown in Table 2.4, where the values have been assumed to be independent of temperature.

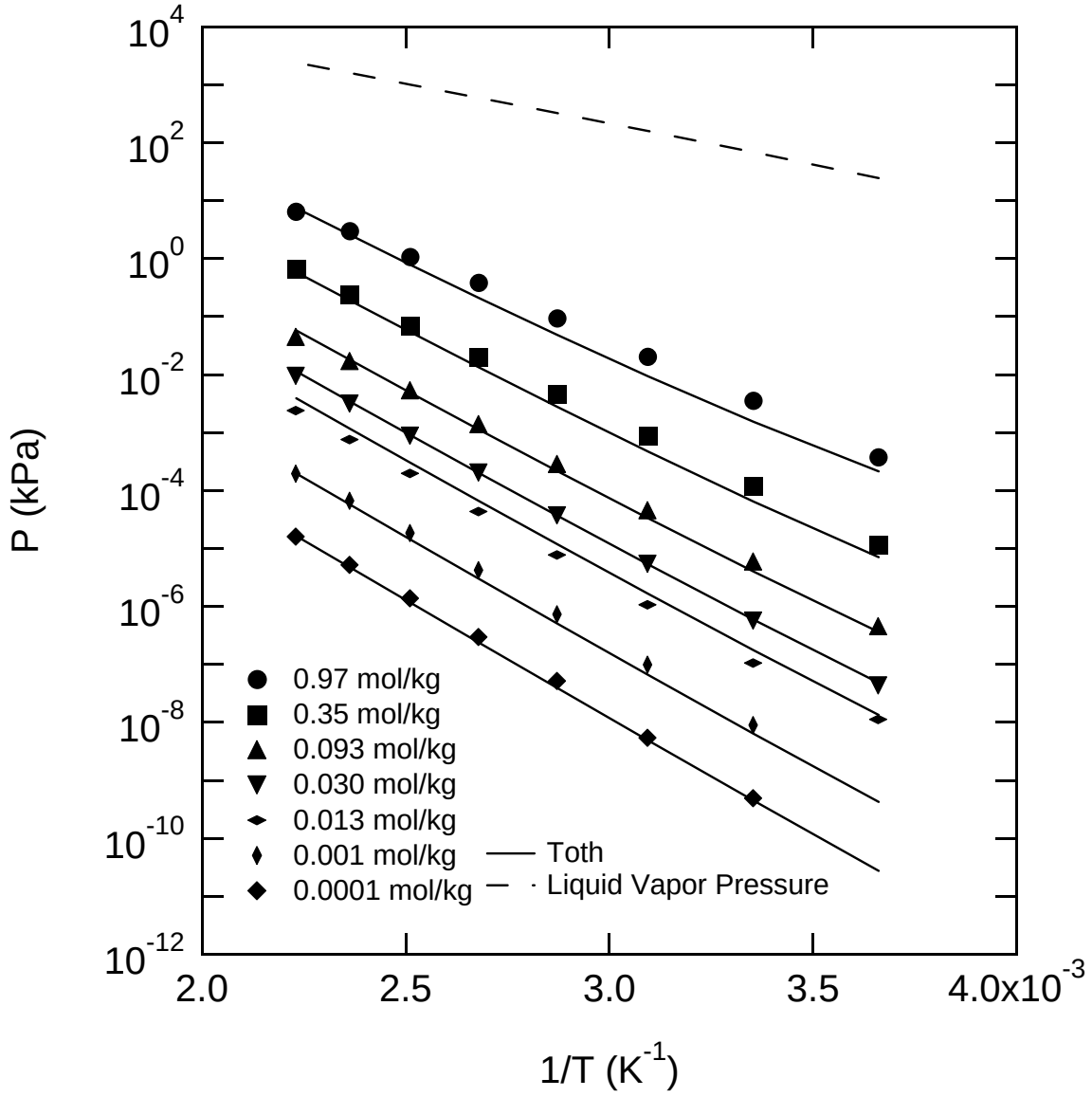

Figure 2.5: Adsorption isosteres for n-pentane on BPL activated carbon with liquid vapor pressure.

Table 2.3: Model parameters for the Langmuir and Toth equations

	n_o (mol/kg)	χ	b_o $(\text{kPa})^{-1}$	Q (kJ mol^{-1})	t_o	α
Langmuir	3.68		1.00×10^{-10}	74.5		
Toth	3.68	9.0×10^{-11}	8.85×10^{-10}	80.2	0.217	0.205

Table 2.4: Calculated isosteric heats of adsorption

Loading (mol kg^{-1})	ΔH_a (kJ mol^{-1})
0.97	59.7
0.35	66.5
0.093	69.9
0.030	72.1
0.013	73.3
0.001	74.1
0.0001	77.3

The isosteric heat of adsorption is shown as a function of loading in Figure 2.6, where it increases with a decrease in loading down to about 0.01 mol kg^{-1}. Below this loading, the curves in Fig. 2.5 are becoming parallel, showing that as the isotherm enters the Henry's law region, the isosteric heat of adsorption asymptotically approaches Q, the isosteric heat at zero loading.

2.4 Conclusions

We have measured adsorption equilibrium for n-pentane on BPL activated carbon over a wide range of loadings. The data extend down into the Henry's law region. The transition into the Henry's law region occurs over a range of loadings near 0.01 mol kg^{-1} for all temperatures.

Our measurements were accomplished by new methods of preparing samples at known constant loadings. At loadings of 0.01 mol kg^{-1} and above, carbon samples were prepared via a liquid injection method, whereas for loadings of 0.01 mol kg^{-1} to 0.0001 mol kg^{-1} samples were prepared by a gas dosing procedure.

The samples were analyzed by a purge and trap method. A carrier gas was used to sweep the adsorbate in the gas phase into a thermal desorption unit, which concentrated the trace organic chemical for measurement of concentration by gas chromatography.

The data were compared with three different adsorption isotherms to examine the transition into the Henry's law region: the DR equation, the Langmuir equation, and the Toth equation. The DR equation is known not to have a proper Henry's law region, and it was shown to deviate from the data. The Langmuir equation has a proper Henry's law region, but the equation does not describe the data. The Toth equation also has a proper Henry's law region and describes the data well. The isosteric heat of adsorption, calculated from $\ln P$ plotted versus $1/T$, increases as the loading decreases but approaches a constant value as the system enters the Henry's

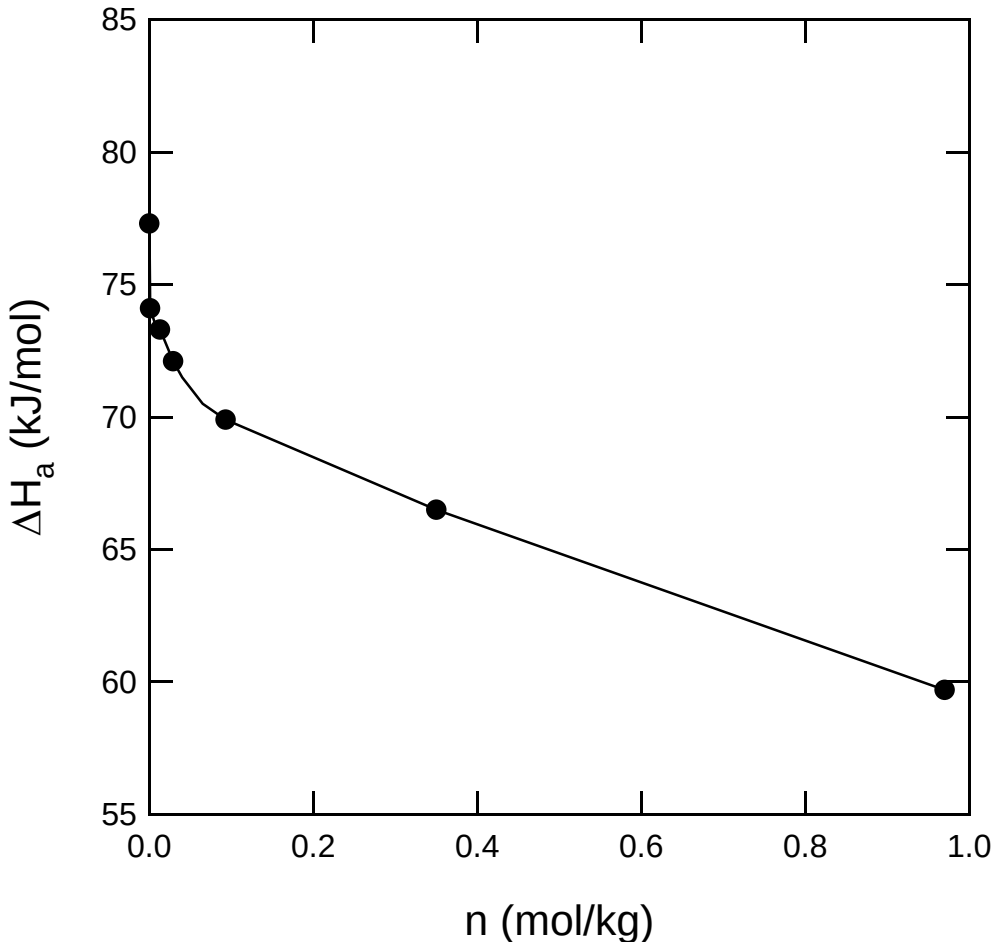

Figure 2.6: Isosteric heat of adsorption vs. loading. These can be compared with the heat of vaporization of 25.79 kJ mol^{-1} for n-pentane at the normal boiling point.[33]

law region.

References

[1] Foster KL, Fuerman RG, Economy J, Larson SM, Rood MJ. Adsorption Characteristics of Trace Volatile Organic Compounds in Gas Streams onto Activated Carbon Fibers. Chem. Mater. 1992; 4:1068–1073

[2] Pinto ML, Pires J, Carvalho AP, de Carvalho MB. On the Difficulties of Predicting the Adsorption of Volatile Organic Compounds at Low Pressures in Microporous Solid: The Example of Ethyl Benzene. J. Phys. Chem. B 2006; 110:250–257

[3] Kuro-oka M, Suzuki T, Nitta T, Katayama T. Adsorption Isotherms of Hydrocarbons and Carbon Dioxide on Activated Fiber Carbon. J. Chem. Eng. Japan 1984; 17:588–592

[4] Eissmann RN, LeVan MD. Coadsorption of Hydrocarbons and Water on BPL Activated Carbon. 2. 1,1,2-Trichloro-1,2,2-trifluoroethane and Dichloromethane. Ind. Eng. Chem. Res. 1993; 32:2752–2757

[5] Kaul BK. Modern Version of Volumeteric Apparatus for Measuring Gas-Solid Equilibrium Data. Ind. Eng. Chem. Res. 1987; 26:928–933

[6] Mahle JJ, Buettner LC, Friday DK. Measurement and Correlation of the Adsorption Equilibria of Refrigerant Vapors on Activated Carbon. Ind. Eng. Chem. Res. 1994; 33:346–354

[7] Russell BP, LeVan MD. Coadsorption of Organic Compounds and Water Vapor on BPL Activated Carbon. 3. Ethane, Propane, and Mixing Rules. Ind. Eng. Chem. Res. 1997; 36:2380–2389

[8] Karwacki CJ, Morrison RW. Adsorptive Retention of Volatile Vapors for Nondestructive Filter Leak Testing. Ind. Eng. Chem. Res. 1998; 37:3470–3480

[9] Pigorini, G. Periodic Behavior of Pressure Swing Adsorption Cycles and Coadsorption of Light and Heavy n–alkanes on Activated Carbon. Charlottsville VA USA, University of Virginia, PhD thesis, 2000

[10] Walton KS, Pigorini G, LeVan MD. Simple Group-Contribution Theory for Adsorption of Gases and Gas Mixtures in Nanoporous Carbons. Chem. Eng. Sci. 2004; 59:4425–4432

[11] LeVan MD, Pigorini G. Group-Contribution Theory for Coadsorption of Gases and Vapors on Solid Surfaces. Proceedings of the First International Conference on Molecular Modeling and Simulation, Keystone, Colorado; Cummings, P. T., Westmoreland, P. R., Eds.; 2001, 296–299

[12] Zhu W, Groen JC, Kapteijn F, Moulijn JA. Adsorption of Butane Isomers and SF_6 on Kureha Activated Carbon: 1. Equilibrium. Langmuir 2004; 20:5277–5284

[13] Zhu W, Groen JC, van Miltenburg A, Kapteijn F, Moulijn JA. Comparison of Adsorption Behavior of Light Alkanes and Alkenes on Kureha Activated Carbon. Carbon 2005; 43:1416–1423

[14] Golden TC, Kumar R. Adsorption Equilibrium and Kinetics for Multiple Trace Impurities in Various Gas Streams on Activated Carbon. Ind. Eng. Chem. Res. 1993; 32:159–165

[15] Do HD, Do DD. Structural Heterogeneity in the Equilibrium Data for Hydrocarbons and Carbon Oxides on Activated Carbons. Gas Separation & Purification 1994; 8:77–93

[16] Rudisill NR, Hacskaylo JJ, LeVan MD. Coadsorption of Hydrocarbons and Water on BPL Activated Carbon. Ind. Eng. Chem. Res. 1992; 31:1122–1130

[17] Yun JH, Hwang KY, Choi DK. Adsorption of Benzene and Toluene Vapors on Activated Carbon Fiber at 298, 323, and 348 K. J. Chem. Eng. Data 1998; 43:843–845

[18] Taqvi SM, Appel AS, LeVan MD. Coadsorption of Organic Compounds and Water Vapor on BPL Activated Carbon. 4. Methanol, Ethanol, Butanol, and Modeling. Ind. Eng. Chem. Res. 1997; 36:2380–2389

[19] Qi N, LeVan MD. Coadsorption of Organic Compounds and Water Vapor on BPL Activated Carbon. 5. Methyl Ethyl Ketone, Methyl Isobutyl Ketone, Toluene, and Modeling. Ind. Eng. Chem. Res. 1997; 36:2380–2389

[20] Yang RT, Long RQ, Padin J, Takahashi A, Takahashi T. Adsorbents of Dioxins: A New Technique for Sorbent Screening for Low-Volatile Organics. Ind. Eng. Chem. Res. 1999; 38:2726–2731

[21] Mayfield PLJ, Do DD. Measurement of the Single-Component Adsorption Kinetics of Ethane, Butane, and Pentane onto Activated Carbon Using a Differential Adsorption Bed. Ind. Eng. Chem. Res. 1991; 30:1262–1270

[22] Linders MJG, Van Den Broeke LJP, Van Bokhoven JJGM, Duisterwinkel AE, Kapteijn F, Moulijn JA. Effect of the Adsorption Iostherm on One-and Two-Component Diffusion in Activated Carbon. Carbon 1997; 35:1415–1425

[23] Himeno S, Urano K. Measurement and Correlation of Single and Binary Gas Adsorption Equilibria of Volatile Organic Compounds in Trace Concentrations using Headspace Gas Chromatography Method. Kagaku Kogaku Ronbunshu 2003; 29:653–659

[24] Himeno S, Kohei U. Determination and Correlation of Binary Gas Adsorption Equilibria of VOCs. J. of Environ. Eng. 2006; 132:301–308

[25] Karwacki CJ, Buettner LC, Buchanan JH, Mahle JJ, Tevault DE. Low-Concentration Adsorption Studies for Low-Volatility Vapors. Fundamentals of Adsorption. Meunier, F.; Ed.; Elsevier: Amsterdam, The Netherlands, 1998: 315–320

[26] Karwacki CJ, Tevault DE, Mahle JJ, Buchnan JH, Buettner LC. Adsorption of Equilibria of Isopropyl Methylphosphonofluoridate (GB) on Activated Carbon at Ultralow Relative Pressures. Langmuir 1999; 15:6343–6345

[27] LeVan MD, Carta G.(2008). Section 16: Adsorption and Ion Exchange. In: Green, DW (Ed.) Perry's Chemical Engineers' Handbook, 8th ed., McGraw-Hill, New York, 16.31–32

[28] Myers AL, Prausnitz JM. Thermodynamics of mixed-gas adsorption. AIChE J. 1965; 11:121–127

[29] Meredith MM, Plank CA. Adsorption of Carbon Dioxide and Nitrogen on Charcoal at 30° and 50 °C. J. Chem. Eng. Data 1967; 12:259–261

[30] Ye XH, Qi N, Ding YQ, LeVan MD. Prediction of Adsorption Equilibrium using a Modified D-R Equation: Pure Organic Compounds on BPL Carbon. Carbon 2003; 41:681–686

[31] De Boer JH. The Dynamical Character of Adsorption, 2nd ed. Oxford: Clarendon Press; 1970

[32] Do DD. Adsorption Analysis: Equilbria and Kinetics. London: Imperial College Press; 1998

[33] Poling BE, Prausnitz JM, O'Connell JP. The Properties of Gases and Liquids. 5th ed. New York:McGraw-Hill;2001

CHAPTER III

THE THEORETICAL MAXIMUM ISOSTERIC HEAT OF ADSORPTION IN THE HENRY'S LAW REGION FOR SLIT-SHAPED CARBON NANOPORES

3.1 Introduction

The isosteric heat of adsorption can yield important information about the mechanism and properties of adsorption. This is especially true for the isosteric heat of adsorption in the Henry's law region, q_{st}^o. From this we can determine the pore size to which the molecules are most strongly attracted.

The Henry's law region for adsorption equilibria is the low-loading region where the isotherm becomes linear. In this regime, each gas molecule can explore the whole adsorbent surface independently, as adsorbate-adsorbate molecule interactions are negligible because of low densities. In the Henry's law region, the gases in the fluid phase will be most strongly attracted to the adsorption sites with the highest energies. However, for a heterogeneous adsorbent, even in the Henry's law region, adsorption will occur over a range of pore sizes, although the distribution will be narrower than at higher pressures. This means that if a material had a single pore size equal to the pore width where q_{st}^o is a maximum, the q_{st}^o calculated would be equal to the maximum theoretical value.

Knowledge of the isosteric heat of adsorption for a molecule as a function of the pore width can help in the design of new materials. It is important in many ongoing efforts to create new synthetic carbonaceous materials such as carbon nanotubes, carbon fibers, metal organic frameworks, and carbon-silica composites. Specifically, it is important to know the pore widths that would be desirable or undesirable for the material, as determined from the process for which the materials are being designed. For some applications, such as air filters, an adsorbent material with a high heat of adsorption would be desired to provide as strong a hold on contaminant molecules

as possible. For gas storage applications, knowing the maximum isosteric heat of adsorption will help screen potential materials for the application.[1,2] For example, Bhatia and Myers[2] have calculated that for hydrogen storage on carbon materials, if the system is run between pressures of 1.5 bar and 30 bar, a change in the isosteric heat of adsorption of 15.1 kJ/mol is needed for optimum delivery. In contrast, in a pressure swing adsorption process, a lower isosteric heat of adsorption would be desired to reduce the thermal swings in the process and allow for a more efficient regeneration.

Steele[3] developed an equation to calculate q_{st}^o using statistical thermodynamics. Steele's equation has been applied by Vernov and Steele[4] to calculate q_{st}^o for benzene adsorbed on graphite. Pikunic *et al.* [5] also used the equation to calculate q_{st}^o for nitrogen adsorbed on graphitic carbon at different temperatures. Do *et al.* [6] used Henry's constants to fit the solid-fluid attractive potential for various gases at different temperatures and also calculated q_{st}^o. Pan *et al.* [7] calculated the isosteric heat of adsorption for propane and butane using density functional theory for a variety of loadings, temperatures, and pore sizes; q_{st}^o was calculated as a function of pore width, which shows a sharp increase for small pores, but a maximum was not found. Floess and VanLishout[8] calculated q_{st}^o for argon as a function of pore width. A maximum was found at 6.8 Å by integrating the Lennard-Jones 6-12 potential over 3 layers of carbon to form the pore walls. In this paper q_{st}^o is calculated as a function of the pore width for nitrogen, argon, carbon dioxide, methane, helium, and hydrogen. We determine where q_{st}^o is a maximum and also where it is equal to zero. We show general results of the pore width where q_{st}^o is a maximum as a function of the solid-fluid collision diameter σ_{sf} and the solid-fluid well depth potential ϵ_{sf}. The theoretical values are compared with q_{st}^o calculated from adsorption isotherms for nitrogen, argon, carbon dioxide, and methane on various activated carbons. Results for helium and hydrogen are not compared with experimental results due to a lack of reliable data.

3.2 Theory

We calculate the isosteric heat of adsorption for various compounds on activated carbon simulated by parallel slit pores. The isosteric heat of adsorption is calculated using the Clausius-Clapeyron equation written at constant adsorbed-phase concentration

$$q_{st} = RT^2 \left.\frac{\partial \ln P}{\partial T}\right|_n \tag{3.1}$$

where R is the ideal gas constant, T is temperature, and P is pressure. Using statistical thermodynamics, Steele[3] developed the following model to calculate q_{st}^o. In the Henry's law region with the isotherm written $n = K_H P$, eq. 3.1 becomes

$$q_{st}^o = -RT^2 \left.\frac{\partial \ln K_H}{\partial T}\right|_n \tag{3.2}$$

The Henry's law constant can be written

$$K_H = \frac{1}{A}\left(\frac{Z_1^{(s)}}{kT}\right) \tag{3.3}$$

where k is Boltzman's constant, A is the surface area of the adsorbent, and

$$Z_1^{(s)} = \int_{V^{(s)}} \exp\left[-V_{ext}(\mathbf{r}_1)/kT\right] d\mathbf{r}_1 \tag{3.4}$$

is the configuration integral for one molecule. Substituting eq. 3.3 and eq. 3.4 into eq. 3.2 we get

$$q_{st}^o = RT - N_a \frac{\int_0^{H_c} V_{ext}(z) \exp\left[-V_{ext}(z)/kT\right] dz}{\int_0^{H_c} \exp\left[-V_{ext}(z)/kT\right] dz} \tag{3.5}$$

where N_a is Avagadro's number and V_{ext} is the external wall potential, which is described by

$$V_{ext}(z) = \phi_{sf}(z) + \phi_{sf}(H - z) \tag{3.6}$$

with

$$\phi_{sf}(z) = 2\pi\epsilon_{sf}\rho_s\sigma_{sf}^2\Delta\left[\frac{2}{5}\left(\frac{\sigma_{sf}}{z}\right)^{10} - \left(\frac{\sigma_{sf}}{z}\right)^4 - \frac{\sigma_{sf}^4}{3\Delta(z + 0.61\Delta)^3}\right] \tag{3.7}$$

where σ_{sf} and ϵ_{sf} are the solid-fluid collision diameter and the solid-fluid well depth potential, respectively. For graphitic activated carbon, $\Delta = 3.35$ Å is the separation

between the graphite planes and $\rho_s = 0.114$ Å^{-3} is the density of the solid.[18] Steele[3] derived eq. 3.7 because integrating a Lennard-Jones 6-12 potential over just a few layers of adsorbent did not give good results. The pore width H_c is the distance between the center of the carbon atoms on opposing walls of the pore, and the pore width $H = H_c - \sigma_{ss}$ is the shortest distance between the surface of the carbon atoms on opposing walls, where $\sigma_{ss} = 3.38$ Å is the size of a carbon atom. See Figure 3.1 for a diagram of the pore.

3.3 Results

We examine q_{st}^o for six different molecules: nitrogen, argon, methane, carbon dioxide, helium, and hydrogen. The parameters used to describe these molecules are given in Table 3.1, with all calculations done at $T = 298.15$ K. The fluid-fluid parameters are included for comparison, but were not used in calculating q_{st}^o because fluid-fluid molecule interactions are negligible in the adsorbed phase in the Henry's law regime. The solid-fluid parameters for all molecules except hydrogen were found in the literature. The solid-fluid parameters were calculated for hydrogen using the Lorentz-Berthelot combining rules

$$\sigma_{sf} = (\sigma_{ff} + \sigma_{ss})/2 \qquad \text{and} \qquad \epsilon_{sf} = \sqrt{\epsilon_{ff}\epsilon_{ss}} \tag{3.8}$$

where $\epsilon_{ss}/k = 27.97$ K. We consider the isosteric heat of adsorption for the six selected molecules to determine where the isosteric heat of adsorption reaches a maximum value and also where the isosteric heat of adsorption is equal to zero.

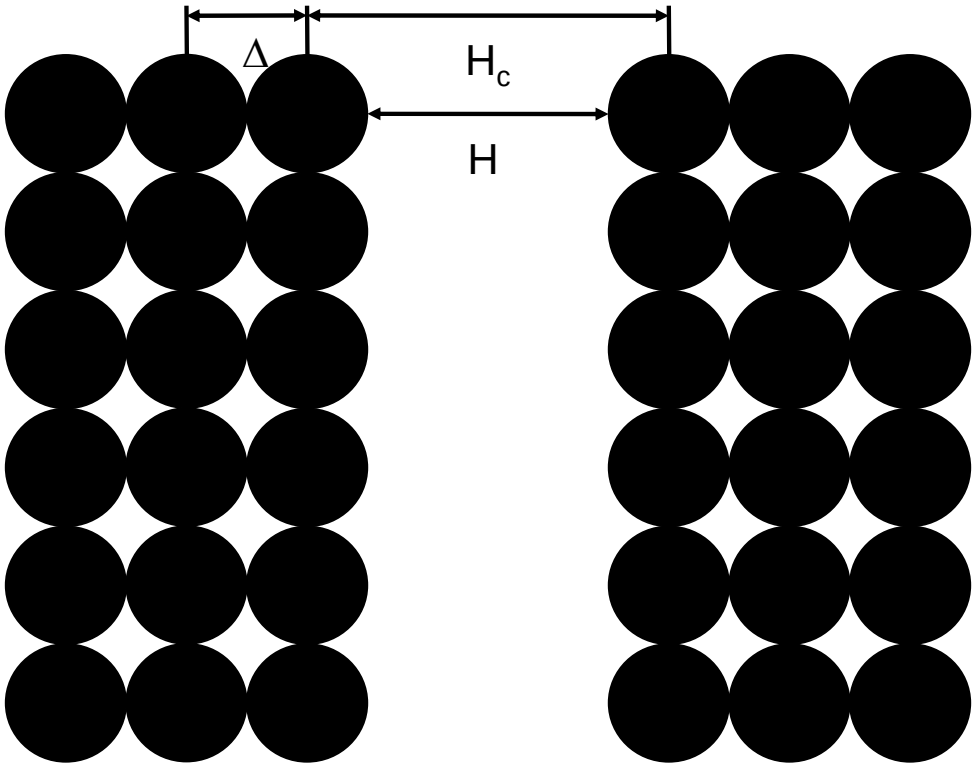

Figure 3.1: Model of graphite parallel slit pore. Carbon atoms continue deep into solid.

Table 3.1: Model Parameters for Different Molecules

Molecule	σ_{ff} (Å)	ϵ_{ff}/k (K)	σ_{sf} (Å)	ϵ_{sf}/k (K)	Reference
N_2	3.575	94.45	3.494	53.22	18
Ar	3.305	118.05	3.35	55.0	18
CO_2	3.454	235.9	3.43	81.5	18
CH_4	3.82	148.2	3.60	64.4	19
He	2.56	10.21	2.98	16.90	3
H_2	2.83	59.7	3.10	40.87	20

We also compare the maximum value of q_{st}^o determined from eq. 3.5 with q_{st}^o calculated from experimental adsorption isotherms. We consider nitrogen adsorbed on Norit R1[9] and Columbia Grade L;[10] argon adsorbed on Norit R1;[9] carbon dioxide adsorbed on BPL,[11] PCB,[12] and Nuxit-AL;[13] and methane adsorbed on Norit R1,[9] BPL,[11,14,15] PCB,[12] Nuxit-AL,[13] and Columbia Grade G.[16] All of the data were described using a multi-temperature Toth isotherm[17] to calculate q_{st}^o. Figure 3.2 shows the isosteric heat calculated using eq. 3.5 as a function of the pore width H. A rapid change in q_{st}^o occurs for pores that are smaller than the pore for which q_{st}^o is a maximum. For larger pores, there is an initial rapid decrease followed by a more gradual decline as the pores get larger. Figure 3.3 shows the pore size of the maximum q_{st}^o as a function of the solid-fluid collision diameter and the solid-fluid well depth potential. The pore size where q_{st}^o is a maximum is a strong function of collision diameter but only a weak function of well depth potential for $\epsilon_{sf}/k > 40$ K. For $\epsilon_{sf}/k < 40$ K, the pore size of maximum q_{st}^o increases appreciably in width. The results shown in Figure 3.3 allow for the easy prediction of the pore size where q_{st}^o is a maximum for various gases.

It can be noted that eq. 3.7 gives the external potential solely in terms of σ_{sf} and ϵ_{sf}. These are the only parameters that enter into the analysis. By coincidence, for our results, the pore width of maximum q_{st}^o plotted versus the fluid-fluid collision diameter σ_{ff} gives a line with a slope of roughly unity with some exceptions, for example helium deviates from the general trend. Additionally, if eq. 3.8 applies, the pore width of maximum q_{st}^o plotted versus σ_{sf} should have a slope of roughly two.

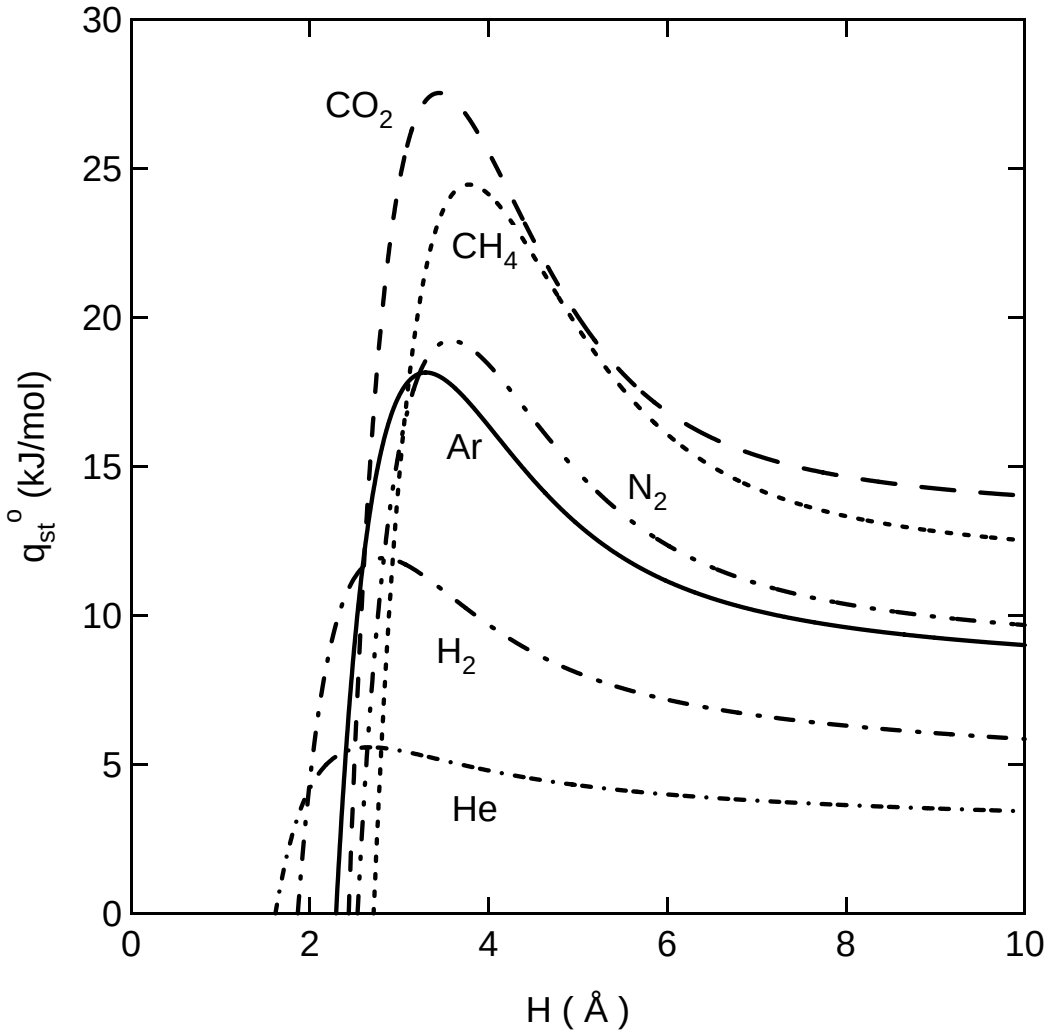

Figure 3.2: The isosteric heat of adsorption in the Henry's law region as a function of pore width.

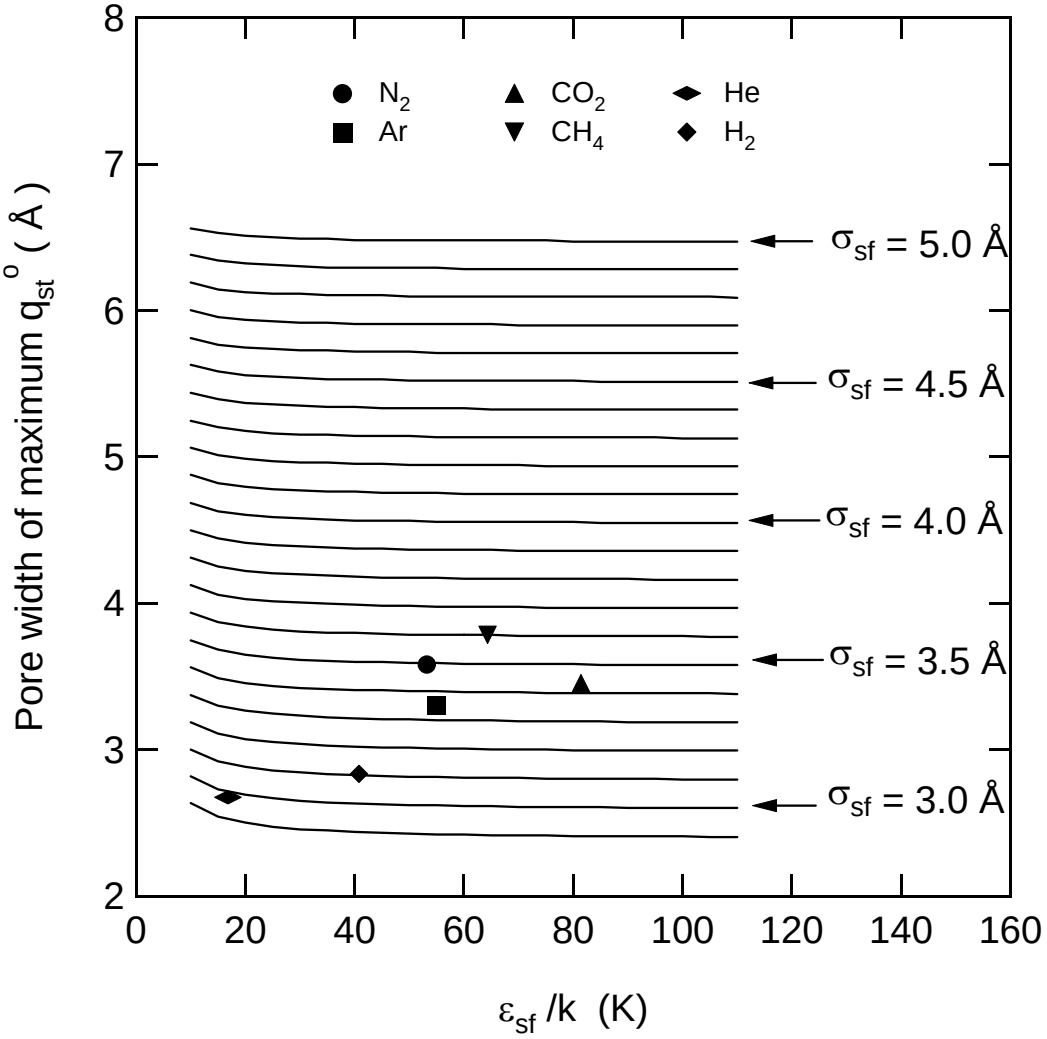

Figure 3.3: The effects of σ_{sf} and ϵ_{sf} on the pore width of the maximum heat of adsorption.

Table 3.2: Isosteric Heat of Adsorption in the Henry's Law Region

Molecule	Pore width of maximum q_{st}^o H (Å)	Pore width of zero q_{st}^o H (Å)	Maximum q_{st}^o (kJ/mol)	q_{st}^o from data (kJ/mol)	Reference
N_2	3.58	2.53	19.23	16.64	9
				15.92	10
Ar	3.30	2.29	18.16	15.22	9
CO_2	3.45	2.43	27.55	21.38	11
				20.55	12
				23.77	13
CH_4	3.78	2.71	24.47	15.80	9
				19.30	11
				20.29	12
				20.34	13
				18.33	14
				20.88	15
				16.26	16
He	2.67	1.61	5.58		
H_2	2.83	1.87	11.93		

For argon the maximum value of q_{st}^o occurs in a pore of width 3.30 Å, which is much smaller than the value calculated by Floess and VanLishout[8] of 6.8 Å. Most of this difference in pore size can be attributed to the differences in the way the pore size is calculated. The pore size of Floess and VanLishout[8] is equivalent to H_c in this paper, the distance from the center of the carbon atoms on opposing sides of the slit pore. If the value of the pore size is changed from H_c to H, the actual slit width between the carbon atoms, the pore size of Floess and VanLishout[8] becomes 3.42 Å. The remaining differences can be attributed to different external potentials and different parameters.

Also of interest is the pore size where q_{st}^o is equal to zero. This point is interesting because the molecules will not adsorb appreciably and adsorption begins to become thermodynamically unfavorable. These pore widths, given in Table 3.2, are smaller than σ_{sf} and correspond roughly to pores for which the external potential is zero at the center, indicating a balance between attractive and repulsive effects. q_{st}^o is equal to zero for argon in a pore of width 2.29 Å. If the same procedure is applied to the pore width for which q_{st}^o is equal to zero as was applied to the pore width of the maximum q_{st}^o, the value of Floess and VanLishout[8] changes from 5.8 Å to 2.42 Å.

The results obtained from eq. 3.5 are compared with q_{st}^o calculated from adsorption isotherms[9–16] in Table 3.2. The values calculated using eq. 3.5 are 15%–55% higher than the values calculated from the adsorption data. These differences can be attributed to the pore size distribution. Even though the isotherm is in the Henry's law region, adsorption occurs in a range of pore sizes. The pore size range will be narrower in the Henry's law region than at higher pressures because the molecules will be exposed to a higher percentage of the adsorption sites with the highest energies. As the pressure increases, because of the energy distribution of adsorption sites and higher loadings, the molecules will fill a broader range of pore sizes including those with lower energies.

The value of the maximum q_{st}^o is important for the design of new materials for processes such as adsorptive storage. As mentioned earlier, Bhatia and Myers[2] calculated the change in the heat of adsorption between two pressures that is needed to reach the Department of Energy's goals for hydrogen[21] and the 180 v/v goal for methane. For hydrogen, adsorbed on carbon materials between the pressures of 1.5 bar and 30 bar at 298 K, the change in the heat of adsorption needs to be 15.1 kJ/mol for optimal delivery. This change in the isosteric heat of adsorption is higher than the maximum q_{st}^o for hydrogen of 11.93 kJ/mol, which occurs in a pore of width 2.83 Å. Also, the optimal value for methane is equal to 18.8 kJ/mol at the same conditions, which is lower than the maximum value of 24.47 kJ/mol, which we found in a pore of width 3.78 Å. This agrees with the conclusion of Bhatia and Myers[2] that carbon materials will not be acceptable for hydrogen storage at ambient temperatures. However, methane could reach the Department of Energy's goal with properly designed materials.

3.4 Conclusions

In this paper we have calculated q_{st}^o as a function of pore width for nitrogen, argon, carbon dioxide, methane, helium, and hydrogen. We have compared the maximum value calculated from eq. 3.5 with the isosteric heat calculated from data adsorbed on various activated carbons. The calculated theoretical maximum was 15%–55% higher than the values calculated from the adsorption isotherms.

The pore size where q_{st}^o is a maximum was calculated as a general function of the collision diameter and the well depth potential, thus allowing for the easy prediction of the pore size where q_{st}^o is a maximum for molecules not discussed in this paper. We have demonstrated that the pore where q_{st}^o is a maximum is a strong function of the collision diameter and a weak function of the well depth potential when ϵ_{sf}/k is greater than 40 K. We have shown that under the conditions set forth

by Bhatia and Myers[2] for adsorptive storage, carbon materials will not be suitable for hydrogen but could be acceptable for methane if designed correctly.

References

[1] Gigras A, Bhatia SK, Anil Kumar AV, Myers AL. Feasibility of tailoring for high isosteric heat to improve effectiveness of hydrogen storage in carbons. Carbon 2007;45:1043–50.

[2] Bhatia SK, Myers AL. Optimum Conditions for Adsorptive Storage. Langmuir 2006;22:1688–1700.

[3] Steele WA. The Interaction of Gases with Solid Surfaces. Oxford:Pergamon Press;1974.

[4] Vernov A, Steele WA. Computer Simulations of Benzene Adsorbed on Graphite. 1. Langmuir 1991;7:3110–17.

[5] Pikunic J, Clinard C, Cohaut N, Gubbins KE, Guet J, Pellenq JM, *et al.* Structural Modeling of Porous Carbons: Constrained Reverse Monte Carlo Method. Langmuir 2003;19:8565–82.

[6] Do DD, Do HD, Tran KN. Analysis of Adsorption of Gases and Vapors on Nonporous Graphatized Thermal Carbon Black. Langmuir 2003;19:5656–68.

[7] Pan H, Ritter JA, Balbuena PB. Isosteric Heats of Adsorption on Carbon Predicted by Density Functional Theory. Ind. Eng. Chem. Res. 1998;37:1159–66.

[8] Floess JK, VanLishout Y. Calculation of Adsorption Energies in Carbon Micropores. Carbon 1992;30:967–73.

[9] Herbst A, Harting P. Thermodynamic Description of Excess Isotherms in High-Pressure Adsorption of Methane, Argon, and Nitrogen. Adsorption 2002;8:111–23.

[10] Ray GC, Box EO. Adsorption of Gases on Activated Charcoal. Ind. Eng. Chem. 1950;42:1315–18.

[11] Reich R, Ziegler WT, Rogers KA. Adsorption of Methane, Ethane, and Ethylene Gases and Their Binary and Ternary Mixtures and Carbon Dioxide on Activated Carbon at 212 – 301 K and Pressures to 35 Atmospheres. Ind. Eng. Chem. Process Des. Dev. 1980;19:336–44.

[12] Ritter JA, Yang RT. Equilibrium Adsorption of Multicomponent Gas Mixtures at Elevated Pressures. Ind. Eng. Chem. Res. 1987;26:1679–86.

[13] Szepesy L, Illes V. Adsorption of Gases and Gas Mixtures I. Acta Chim. Hung. 1963;35:37–51. ,Szepesy L, Illes V. Adsorption of Gases and Gas Mixtures II. Acta Chim. Hung. 1963;35:53–60.

[14] Belmabkhout Y, De Weireld G, Frére M. High-Pressure Adsorption Isotherms of N_2, CH_4, O_2, and Ar on Different Carbonaceous Adsorbents. J. Chem. Eng. Data 2004;49:1379–91.

[15] Pigorini G. Periodic Behavior of Pressure Swing Adsorption Cycles and Coadsorption of Light and Heavy n-Alkanes on Activated Carbon. Charlottesville VA USA, University of Virginia, Ph.D. thesis, 2000.

[16] Payne HK, Studervant GA, Leland TW. Improved Two-Dimensional Equation of State to Predict Adsorption of Pure and Mixed Hydrocarbons. Ind. Eng. Chem. Fundam. 1968;7:363–74.

[17] Do DD. Adsorption Analysis: Equilbria and Kinetics. London:Imperial College Press;1998.

[18] Ravikovitch PI, Nishnyakov A, Russo R, Neimark AV. Unified Approach to Pore Size Characterization of Microporous Carbonaceous Materials for N_2, Ar, and CO_2, Adsorption Isotherms. Langmuir 2000;16:2311–20.

[19] Ravikovitch PI, Nishnyakov A, Neimark AV. Density functional theories and molecular simulations of adsorption and phase transitions in nanopores. Physical Review E 2001;64:Art. No. 011602.

[20] Poling BE, Prausnitz JM, O'Connell JP. The Properties of Gases and Liquids. 5th ed. New York:McGraw-Hill;2001.

[21] DOE Hydrogen Program. 2006 Annual Program Report; Department of Energy; 2006. p. 273–279.

CHAPTER IV

MODELING ADSORPTION OF NITROGEN AND PENTANE ON ACTIVATED CARBON USING SAFT-DFT

4.1 Introduction

The introduction of density functional theory (DFT) to model inhomogeneous fluids represents a significant advance in fluid theory. The development of DFT was encouraged by the desire to accurately model phase transitions and has been used successfully to simulate the adsorption of spherical molecules and the vapor-liquid phase transition.[1,2] DFT was developed with the desire to model systems at the molecular level with fundamental parameters which include those needed to model the bulk fluid, the monolayer transition of the adsorbate on a sheet of graphite, and the pore size distribution(PSD) of the adsorbent.

Tarazona[3,4] developed a weighted density approximation for spherical molecules. A power series expansion in density was used to describe the direct correlation function. Although this method does not have a solid foundation in theory, it has been successfully applied to many situations.[5–19]

Another theory called Fundamental Measure Theory (FMT) was developed by Rosenfeld[20,21] and later improved by Roth *et al.*[22] as an extension of scaled particle theory for an inhomogeneous fluid. FMT uses simple geometric definitions to describe a series of densities that when combined correctly describe the direct correlation function. FMT has been used for a variety of applications.[11,23–26] A review of the development of DFT, both weighted density approximation and FMT, for spherical molecules is available.[27]

Pioneering work by Wertheim[28–31] on thermodynamic perturbation theory has led to the development of statistical associating fluid theory (SAFT). Much research has been performed on SAFT as an equation of state, and reviews are available.[32,33]

There have been many systems studied including alkanes of low molecular weight through simple polymers[34–38] and their binary mixtures,[39–48] perfluoroalkanes,[49–51] boron triflouride,[52] water,[53,54] refrigerant systems,[55] and carbon dioxide.[45,50,56–58]

There is much interest in expanding the use of DFT to systems of larger molecules, such as polymers and chain fluids. There has been an effort to include SAFT into DFT. The method has split into two distinct ways to calculate the grand potential. A method first proposed by Chandler *et al.*[59–61] uses a density expansion approach similar to integral equations. The second method is an extension of FMT. There have been a number of different ways that this was done, such as by Woodward,[62,63] Liu,[64,65] Chapman,[66–68] and Wu.[69–71] Yu and Wu[70] used FMT as a basis for a hard sphere chain fluid. Chapman[66] added terms for a first order attractive potential with a mean field approximation.

In this paper, we extend the theory of Yu and Wu[70] for adsorption in slit-shaped pores. We develop DFT for chain fluids with a first-order non-mean field approximation and second-order attractive perturbation term. Along the way we compare our results with published results of Monte Carlo simulations for hard-sphere chains near hard walls and chains with attractive potentials in the presence of hard walls and attractive walls. Then, we use the theory to model the density profiles of nitrogen in a carbon parallel slit pore. These data are used to calculate a PSD for BPL activated carbon. Then we will apply the model to pentane adsorption in the same system. Using the PSD and the pentane density profiles we calculate an isotherm for pentane.

4.2 Theory

Model

Density functional theory is used to calculate the density profile that minimizes the grand potential function $\Omega[\rho_M(\mathbf{R})]$, where $\rho_M(\mathbf{R})$ is the density profile of a chain

molecule as a function of segment position $\mathbf{R} \equiv (\mathbf{r}_1, \mathbf{r}_2, \cdots, \mathbf{r}_M)$ and M is the number of segments in the chain. This is done by setting the functional derivative with respect to the density equal to zero. The grand potential is calculated by

$$\Omega[\rho_M(\mathbf{R})] = F[\rho_M(\mathbf{R})] + \int \rho_M(\mathbf{R})[V_{ext}(\mathbf{R}) - \mu_M]d\mathbf{R} \tag{4.1}$$

where $F[\rho_M(\mathbf{R})]$ is the Helmholtz free energy, μ_M is the chemical potential for the chain molecule calculated by the SAFT equation of state, and $V_{ext}(\mathbf{R})$ is the external potential.

The Helmholtz free energy is calculated by an ideal term and excess terms. The excess terms consist of hard sphere repulsion, chain connectivity, and a first and second order perturbation for the attractive terms. The ideal term is calculated by

$$F_{id} = kT \int \rho(\mathbf{r}) \left[\ln(\Lambda^3 \rho(\mathbf{r})) - 1\right] d\mathbf{r} \tag{4.2}$$

where Λ is the de Broglie wave length. The density $\rho(\mathbf{r})$ is used instead of $\rho_M(\mathbf{R})$ because we are solving for the segment density, not the molecular density. The chemical potential of the ideal term is calculated from

$$\mu_{id} = kT \ln(\rho_M \Lambda^3) \tag{4.3}$$

where ρ_M is the molecular density, which is equal to $M \times \rho_b$, where ρ_b is the segment density.

The hard sphere repulsive term is calculated by FMT as developed by Rosenfeld[20] and improved upon later by Roth *et al.*[22] for a Mansoori-Carnahan-Starling-Leland (MCSL) fluid. Using the improved equations for a MCSL fluid, the hard sphere free energy is written

$$F_{hs} = kT \int \Phi^{hs}[n_\alpha(\mathbf{r}')]d\mathbf{r}' \tag{4.4}$$

where

$$\begin{aligned}\Phi^{hs}[n_\alpha(\mathbf{r})] = -n_0 \ln(1-n_3) + \frac{n_1 n_2 - \mathbf{n}_{V1} \cdot \mathbf{n}_{V2}}{1-n_3} + \\ \frac{(n_2^3 - 3n_2 \mathbf{n}_{V2} \cdot \mathbf{n}_{V2})(n_3 + (1-n_3)^2 \ln(1-n_3))}{36\pi n_3^2 (1-n_3)^2}\end{aligned} \tag{4.5}$$

Following the definitions of FMT, a series of scalar and vector densities are defined as

$$n_i(\mathbf{r}) = \int \rho(\mathbf{r}')\omega_i(\mathbf{r}-\mathbf{r}')d\mathbf{r}' \tag{4.6}$$

where the subscript $i = 0, 1, 2, 3, V1, V2$ denote different weighting functions. The six different weighting functions are related to the geometry of a particle:

$$\omega_3(r) = \Theta(R-r) \tag{4.7}$$

$$\omega_2(r) = |\nabla\Theta(R-r)| = \delta(R-r) \tag{4.8}$$

$$\omega_1(r) = \frac{\omega_2(r)}{4\pi R} \tag{4.9}$$

$$\omega_0(r) = \frac{\omega_2(r)}{4\pi R^2} \tag{4.10}$$

$$\omega_{V2}(\mathbf{r}) = \nabla\Theta(R-r) = \frac{\mathbf{r}}{r}\delta(R-r) \tag{4.11}$$

$$\omega_{V1}(\mathbf{r}) = \frac{\omega_{V2}(\mathbf{r})}{4\pi R} \tag{4.12}$$

where the vector terms $\mathbf{n}_{V1}$ and $\mathbf{n}_{V2}$ vanish in the bulk. The chemical potential for the hard sphere term is calculated from

$$\mu_{hs} = MkT\sum_i \frac{\partial\phi_b^{hs}}{\partial n_{i,b}}\frac{\partial n_{i,b}}{\partial\rho_b} \tag{4.13}$$

where in the bulk $n_{3,b} = 4/3\pi R^3\rho_b$, $n_{2,b} = 4\pi R^2\rho_b$, $n_{1,b} = R\rho_b$, and $n_{0,b} = \rho_b$.

The chain term, developed by Yu and Wu[70] is described by

$$F_{chain} = kT\int \Phi^{chain}[n_\alpha(\mathbf{r}')]d\mathbf{r}' \tag{4.14}$$

where

$$\Phi^{chain}[n_\alpha(\mathbf{r})] = \frac{1-M}{M}n_0\zeta\ln y^{hs}(\sigma, n_\alpha) \tag{4.15}$$

with

$$\zeta = 1 - \frac{\mathbf{n}_{V2}\cdot\mathbf{n}_{V2}}{n_2^2} \tag{4.16}$$

and

$$y^{hs}(\sigma, n_\alpha) = \frac{1}{1-n_3} + \frac{n_2\sigma\zeta}{4(1-n_3)^2} + \frac{n_2^2\sigma^2\zeta}{72(1-n_3)^3} \tag{4.17}$$

The chemical potential for the chain term is described by

$$\mu_{chain} = kT(1-M)\sum_i \frac{\partial \phi_b^{chain}}{\partial n_i}\frac{\partial n_i}{\partial \rho_b} \tag{4.18}$$

For the attractive terms we used a perturbation analysis, neglecting a mean field assumption, and expanding out to the second order term. The first-order term is

$$F_1 = \frac{1}{2}\int \rho(\mathbf{r}')\int \rho(\mathbf{r}'')g_{hs}[n_3(\mathbf{r}'');\mathbf{r}'']\phi(|\mathbf{r}'-\mathbf{r}''|)d\mathbf{r}''d\mathbf{r}' \tag{4.19}$$

where the attractive potential is a square-well

$$\phi(r;\lambda) = \begin{cases} -\epsilon_{ff} & \text{if} \quad \sigma \le r < \lambda\sigma \\ 0 & \text{if} \quad r \ge \lambda\sigma \end{cases} \tag{4.20}$$

and the hard sphere radial distribution function, g_{hs}, developed by Chang and Sandler[72] with a Verlet-Weis[73] correction, is a function of distance and density. The chemical potential for the first-order term is

$$\mu_1 = -4M\epsilon(\lambda^3-1)\left(2n_{3,b}g_e^{hs} + n_{3,b}^2\frac{\partial g_e^{hs}}{\partial \eta_e}\frac{\partial \eta_e}{\partial n_3}\right) \tag{4.21}$$

where the hard sphere radial distribution function is calculated by

$$g_e^{hs} = \frac{1-\eta_e/2}{(1-\eta_e)^3} \tag{4.22}$$

and the effective density is calculated for an extended value up to $\lambda = 3$ using the relation of Patel *et al.*[74]

$$\eta_e = \frac{c_1 n_{3,b} + c_2 n_{3,b}^2}{(1+c_3 n_{3,b})^3} \tag{4.23}$$

with

$$\begin{pmatrix} c_1 \\ c_2 \\ c_3 \end{pmatrix} = \begin{pmatrix} -3.16492 & 13.35007 & -14.80567 & 5.70286 \\ 43.00422 & -191.66232 & 273.89683 & -128.93337 \\ 65.04194 & -266.46273 & 361.04309 & 162.69963 \end{pmatrix} \begin{pmatrix} 1/\lambda \\ 1/\lambda^2 \\ 1/\lambda^3 \\ 1/\lambda^4 \end{pmatrix} \tag{4.24}$$

The second-order term, developed by Zhang,[75–77] is a macroscopic compressibility approximation that takes neighboring shells into account. It is given by

$$F_2 = -\frac{1}{4kT}\int \rho(\mathbf{r}')\int \rho(\mathbf{r}'')(1+2\xi n_3^2)[\phi(|\mathbf{r}'-\mathbf{r}''|)]^2 K_{hs}(\mathbf{r}'')g_{hs}[n_3(\mathbf{r}'');\mathbf{r}'']d\mathbf{r}'d\mathbf{r}'' \tag{4.25}$$

where $\xi = 1/0.493^2$. The hard sphere isothermal compressibility for a MCSL fluid is calculated from

$$K_{hs} = \frac{(1-n_3)^4}{1+4n_3+4n_3^2-4n_3^3+n_3^4} \tag{4.26}$$

with the chemical potential calculated by

$$\begin{aligned}\mu_2 = \frac{-2M\epsilon^2(\lambda^3-1)}{kT}\left[4\xi n_{3,b}^3 K^{hs} g_e^{hs} + \left(1+2\xi n_{3,b}^2\right)\right. \\ \left.\left(2n_{3,b}K^{hs}g_e^{hs} + n_{3,b}^2\left[\frac{\partial K^{hs}}{\partial n_{3,b}}g_e^{hs} + K^{hs}\frac{\partial g^{hs_e}}{\partial \eta_e}\frac{\partial \eta_e}{\partial n_{3,b}}\right]\right)\right]\end{aligned} \tag{4.27}$$

The equation used for the external potential depends on the situation being described. The interaction between a hard-sphere chain and a hard wall is described by

$$V_{ext}(z) = \begin{cases} 0, & z \geq 0 \\ \infty, & z < 0 \end{cases} \tag{4.28}$$

The interaction with a square-well attractive wall is described by

$$V_{ext}(z) = \begin{cases} 0, & z > \sigma \\ -\epsilon_w, & 0 < z < \sigma \\ \infty, & z < 0 \end{cases} \tag{4.29}$$

The carbon wall is described by a 10-4-3 wall[78]

$$V_{ext} = \phi_{sf}(z) + \phi_{sf}(H-z) \tag{4.30}$$

where

$$\phi_{sf}(z) = 2\pi\epsilon_{sf}\rho_s\sigma_{sf}^2\Delta\left[\frac{2}{5}\left(\frac{\sigma_{sf}}{z}\right)^{10} - \left(\frac{\sigma_{sf}}{z}\right)^4 - \frac{\sigma_{sf}^4}{3\Delta(z+0.61\Delta)^3}\right] \tag{4.31}$$

with $\rho_s = 0.114$ Å^{-3} and $\Delta = 3.35$ Å.

Taking the functional derivative of eq. 4.1 and rearranging results in the equation used to calculate the segment equilibrium density profile

$$\rho(z) = \frac{1}{\Lambda^3}\exp(\mu)\sum_{i=1}^{M}\exp\left[-\frac{\psi(z)}{kT}\right]G^i(z)G^{M+1-i}(z) \tag{4.32}$$

where M is the number of segments and μ is the chemical potential. The solution method involves iterating on the segment density. In eq. 4.32, we have

$$\psi(z) = \frac{\delta F_{hs}}{\delta\rho(\mathbf{r})} + \frac{\delta F_{chain}}{\delta\rho(\mathbf{r})} + \frac{\delta F_1}{\delta\rho(\mathbf{r})} + \frac{\delta F_2}{\delta\rho(\mathbf{r})} + V_{ext} \tag{4.33}$$

and

$$G^i = \int \exp\left[-\frac{\psi(z)}{kT}\right] \frac{\Theta(\sigma - |z - z'|)}{2\sigma} G^{i-1} dz' \tag{4.34}$$

where $G^1(z) = 1$. Due to the summation term in eq. 4.32, the value of the parameter M is limited to integer values.

The equilibrium value of the density, calculated from eq. 4.32, is then used to calculate the average excess density in the pore using

$$\rho(H, P) = \frac{1}{H} \int_0^H \left[\frac{\rho(z)}{M} - \rho_b\right] dz \tag{4.35}$$

where ρ_b is the bulk density, $H = H_c - \sigma_{ss}$ is the pore width and H_c is the distance between the center of the carbon atoms on opposing walls, and $\sigma_{ss} = 3.38$Å is the diameter of the carbon atom. The average excess density is calculated for all pore widths h and all pressures P.

The PSD of the material is calculated by integrating the average densities in pores over the range of pore widths and pressures using the adsorption integral equation

$$n(P_i) = \int_0^h \rho(h, P_i) f(h) dh \ldots i = 1, n \tag{4.36}$$

where $\rho(h, P_i)$ is the average density in the pore and $f(h)$ is the pore size distribution.

The model used for the PSD is a log normal distribution

$$f(h) = \sum_{i=1}^{m} \frac{\alpha_i}{\gamma_i h \sqrt{2\pi}} \exp\left[\frac{-(\ln(h) - \beta_i)^2}{2\gamma_i^2}\right] \tag{4.37}$$

where m is the number of modes and α_i, β_i, and γ_i are parameters.

Model Validation

As the model was being developed, results were compared with a variety of different examples in the literature for validation. The model was compared against a set of hard-sphere chain results against hard-walls. Fig. 4.1 compares the segment density profiles of the model against a series of Monte Carlo simulations by Kierlik

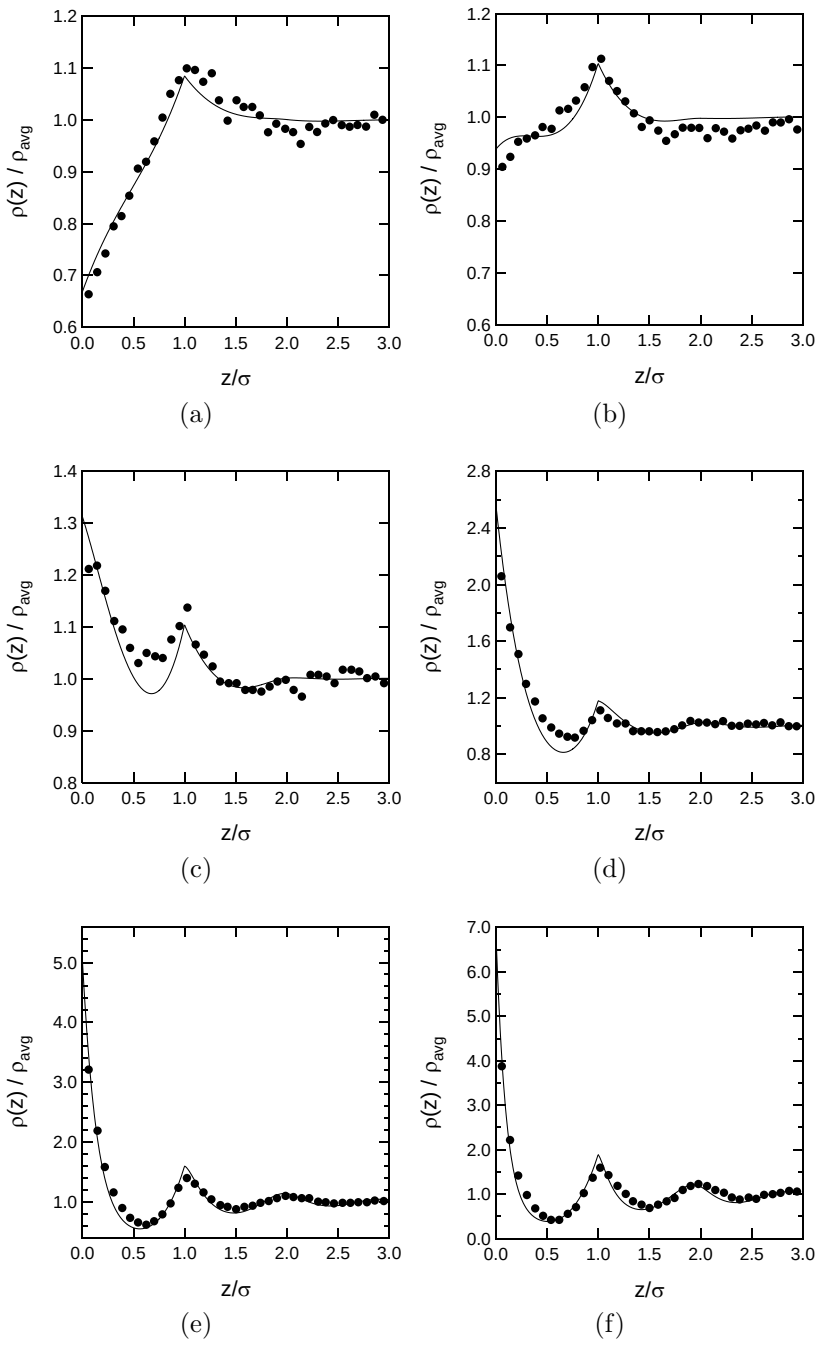

Figure 4.1: Hard sphere 3-mer against a hard wall. Monte Carlo simulations from Kierlik and Rosinberg.[79] The average packing fractions are (a) η =0.1, (b) η =0.15, (c)η =0.2, (d) η =0.3, (e) η =0.4, (f) η =0.45. The solid curve is the model.

and Rosinberg[79] for 3-mer chains at packing fractions from $\eta = 0.1$ to 0.45. Fig. 4.2 shows the results for the segment density profiles for the model with simulations of 4-mer chains by Dickman and Hall[80] at packing densities from 0.107 to 0.417. Fig. 4.3 shows the model results compared with simulations of 20-mer chains by Yethiraj and Woodward[81] at packing fractions from 0.1 to 0.35. It is apparent from these that the model shows agreement with Monte Carlo simulation results over a wide range of bulk densities and chain lengths.

Then, an attractive potential was added to the model by the addition of eq. 4.19 and eq. 4.25 with $\epsilon_{ff}/kT = 3.0$. Results were compared with Monte Carlo simulations by Ye *et al.*,[64] who modeled a 3-mer fluid with an attractive potential near both a hard wall and an attractive wall. The interaction with the hard wall was simulated by eq. 4.28, while the attractive wall was simulated by eq. 4.29. The model results shown in Fig. 4.4 show good quantitative agreement with the Monte Carlo simulations near both the hard wall and the attractive wall. The effects of the second order attractive term tend to be an order of magnitude lower than the first order attractive term, and the first order attractive term tends to be an order of magnitude lower than the hard sphere and chain terms. The effects of adding the attractive terms can be seen by comparing the density profiles of Figs. 4.1a and 4.4a, and Figs. 4.1d and 4.4b. At lower densities shown in, Figs. 4.1a and 4.4a, the attractive term tends to flatten out the density profiles, but at higher densities shown in, Figs. 4.1d and 4.4b, it lowers the contact density with the wall and increases the number of layers of molecules at the wall.

Parameter Estimation for Real Fluids

The parameters for the model fall into two different categories, fluid-fluid interactions and solid-fluid interactions. The parameters shown in Table 4.1 for nitrogen and n-pentane were determined by two different methods. First, the fluid-fluid param-

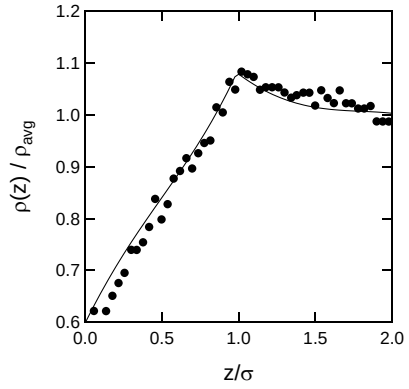

(a)

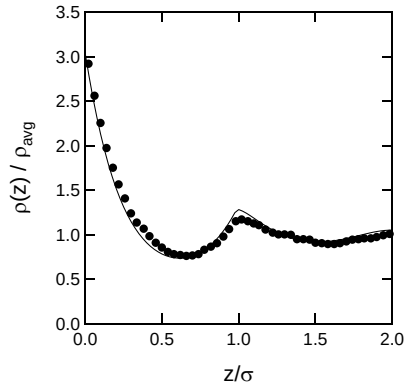

(b)

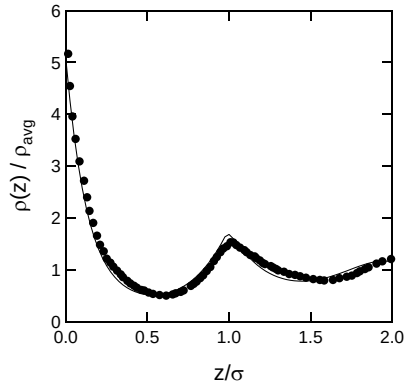

(c)

Figure 4.2: Hard sphere 4-mer against a hard wall. Monte Carlo simulations from Dickman and Hall.[80] The average packing fractions are (a) η =0.107, (b) η =0.34, (c)η =0.417. The solid curve is the model.

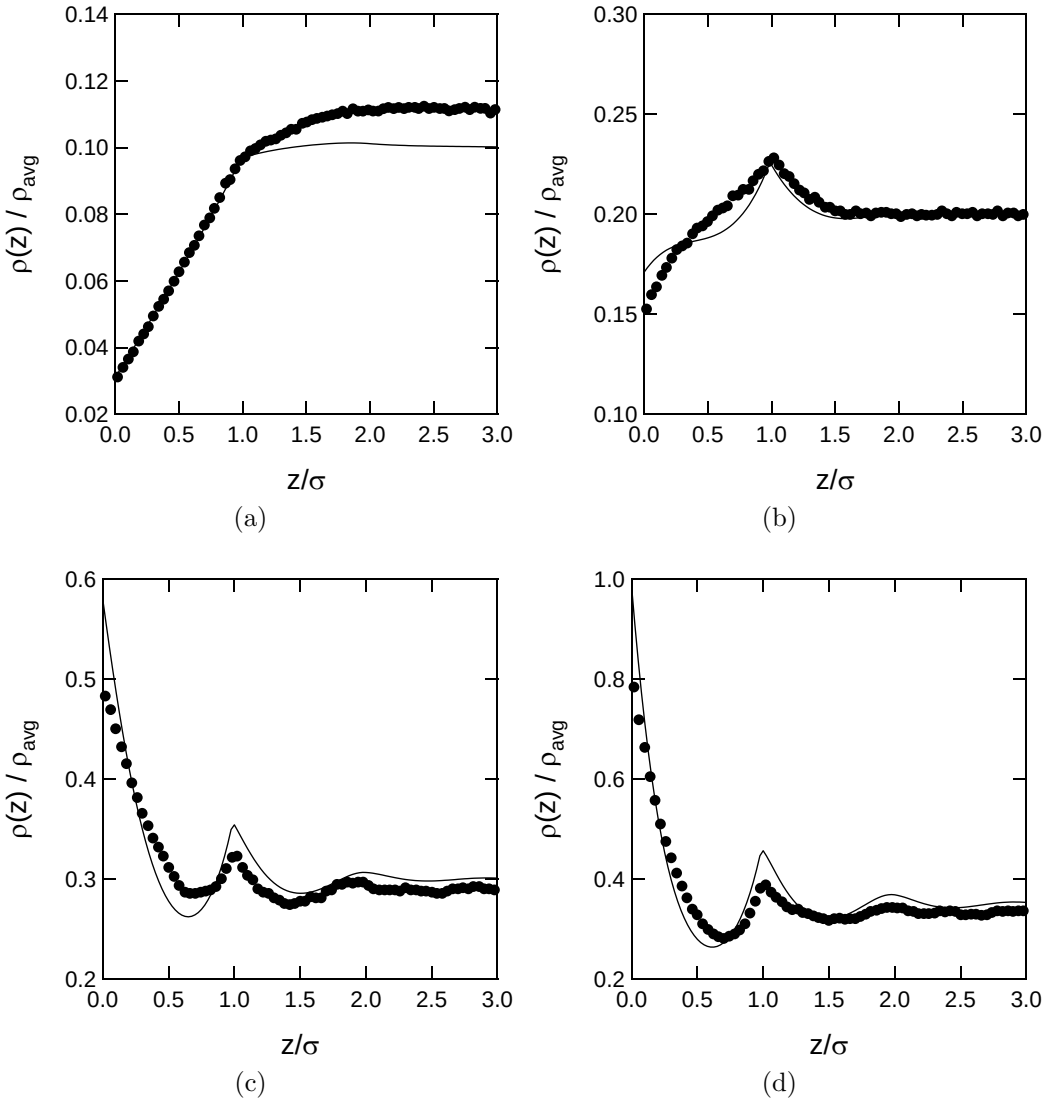

Figure 4.3: Hard sphere 20-mer against a hard wall. Monte Carlo simulations from Yethiraj and Woodward.[81] The average packing fractions are (a) η =0.1, (b) η =0.2, (c)η =0.3, (d) $\eta = 0.35$. The solid curve is the model.

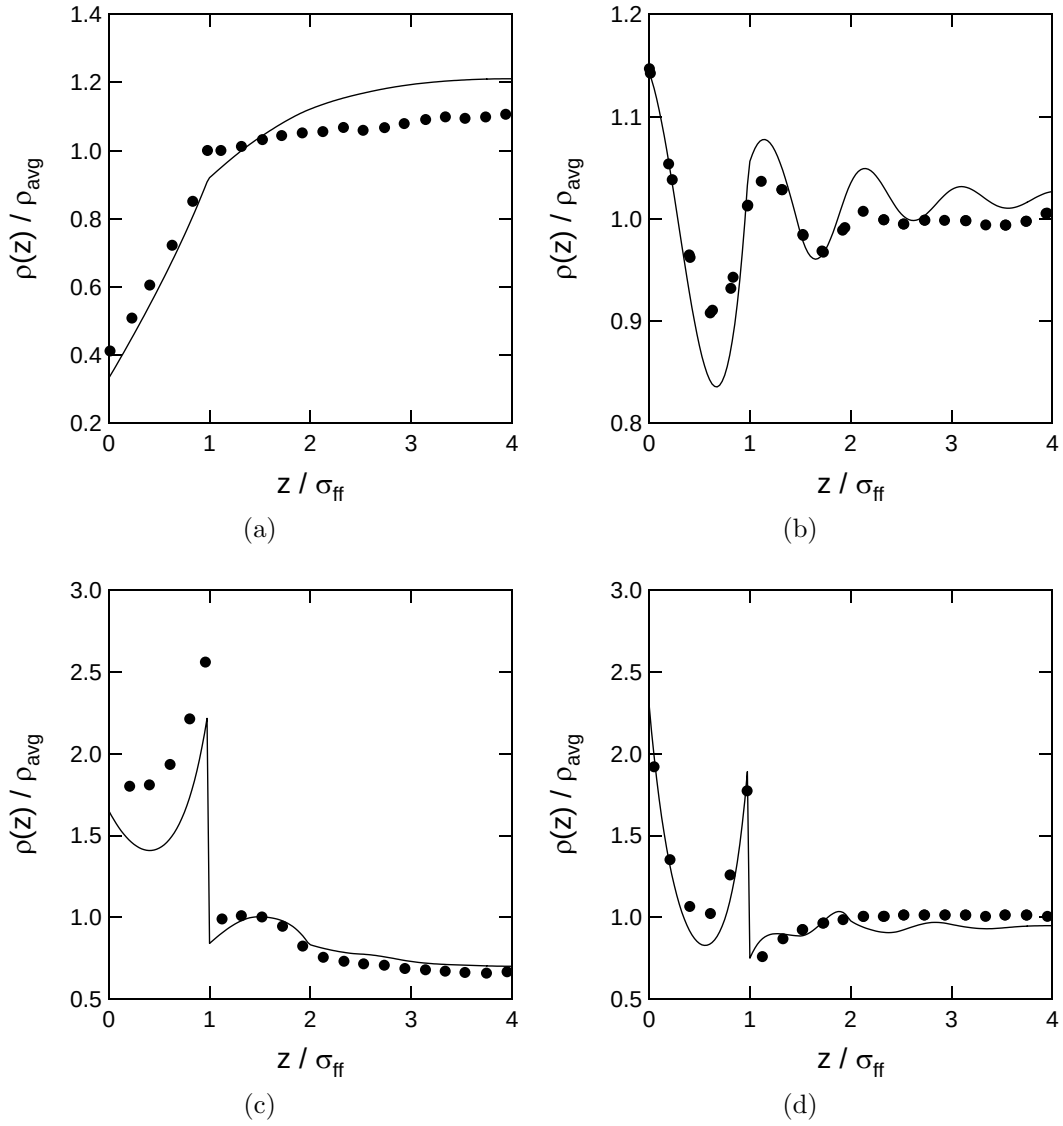

Figure 4.4: Attractive sphere 3-mer against a hard and attractive wall. Monte Carlo simulations from Ye *et al.*[64] The average packing fractions are (a) η =0.1 hard wall, (b) η =0.3 hard wall, (c) η =0.1 attractive wall, (d) η =0.3 attractive wall. For the attractive wall, the potential between the wall and the fluid is $\epsilon_w/kT = -1.0$. The solid curve is the model.

Table 4.1: Model parameters

molecule	σ_{ff} (Å)	ϵ_{ff}/k (K)	λ	M	σ_{sf} (Å)	ϵ_{sf}/k (K)
nitrogen	2.657	40.282	1.83	2	3.0185	42.98
n-pentane	2.791	57.083	2.163	5	3.086	74.63

eters were estimated using the saturated vapor pressure curve and the liquid-vapor coexistence curve. Then, the solid-fluid parameters were determined by a method described by Lastoskie *et al.*[5] The solid-fluid molecular diameter σ_{sf} was calculated using the Lorentz-Berthelot mixing rules (arithmetic mean) using the fluid-fluid molecular diameter σ_{ff} and the solid molecular diameter σ_{ss}. The solid-fluid potential ϵ_{sf} was determined from fitting the onset of the monolayer transition. Results for parameter estimation will be discussed in the next sections.

4.3 Results

Nitrogen

To estimate the solid-fluid parameters, the process discussed above was used. For nitrogen, we used data from Kruk *et al.*[82] on Carbopack F, a commercially available graphitized carbon black with a BET surface area of 6.2 m^2/g. A large pore of half width $h = 20\ \sigma_{ff}$ was used to simulate a non-porous surface, and the results are shown in Fig. 4.5. The solid-fluid potential chosen was the value that best described the curve over the entire range of pressures, up to a reduced pressure of 4×10^{-3}.

Solving eq. 4.32 gives a density profile. In the next few paragraphs we will be discussing density profiles for three different pore sizes. They will be shown at three different pressures for each pore size. We will be showing one before the monolayer transition, one after the monolayer transition but before the freezing transition, and one after the freezing transition.

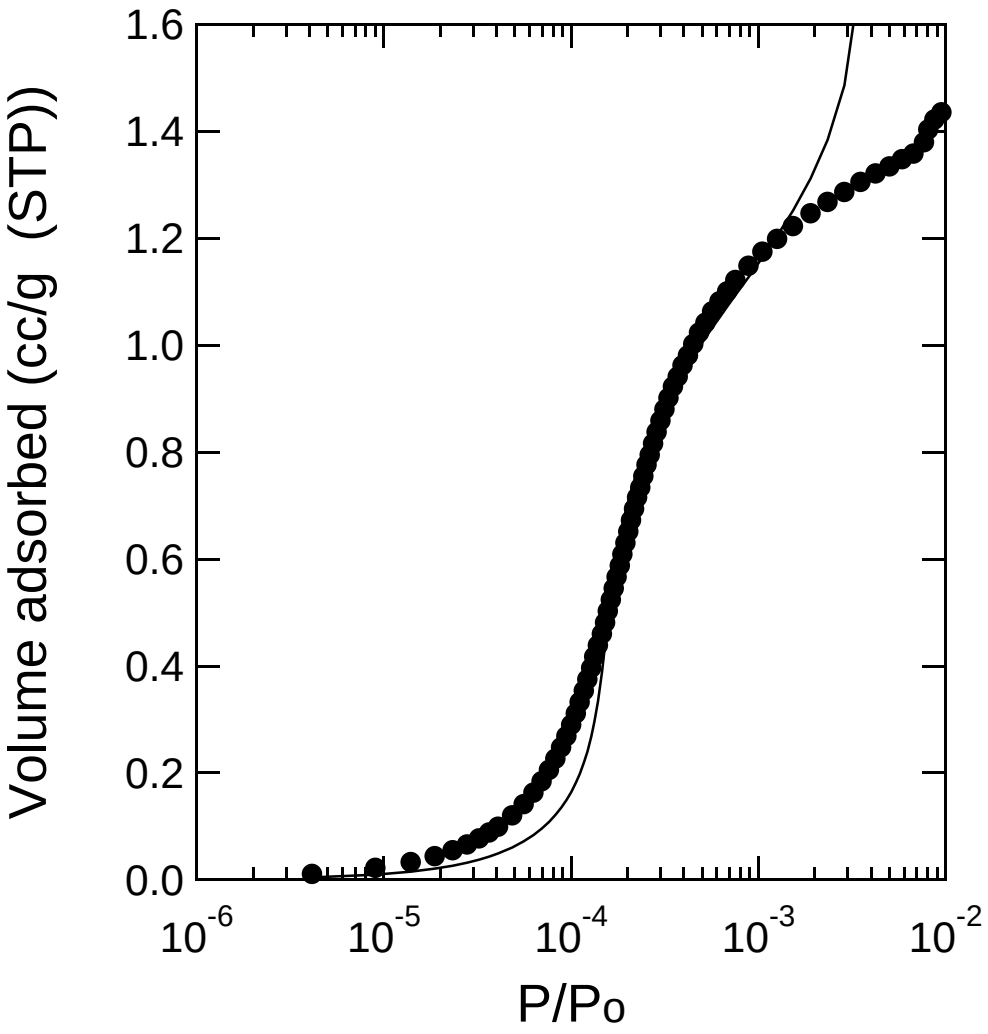

Figure 4.5: Comparison of experimental and theoretical adsorbed volumes of nitrogen on nonporous carbon black at 77 K. The points are experimental data. The solid line is the nitrogen prediction.

Figs. 4.6, 4.7, and 4.8 show the density profiles for nitrogen in pores of widths 0.564 nm, 0.991 nm, and 1.03 nm, respectively. These correspond to pores with total widths of 3.175 σ_{ff}, 4.825 σ_{ff}, and 4.975 σ_{ff}. A pore wall exists at $z = 0$ and, except when noted, only a half pore is shown, extending out to the centerline.

Figs. 4.6a, 4.7a, and 4.8a show density profiles for pressures that are below the monolayer transition. Fig. 4.6a shows the density profile when the reduced pressure is 1.0×10^{-6}, Fig. 4.7a is the density profile at a reduced pressure of 1.0×10^{-5}, and Fig. 4.8a is at a reduced pressure of 5.0×10^{-5}. It should be noted in these figures that the first peak does not occur at z = σ_{ff}. This is because the solid and the fluid segments have different sizes; i.e., $\sigma_{sf} = 3.018$ Å differs from $\sigma_{ff} = 2.657$ Å. Thus, the first peak occurs at z somewhat greater than σ_{ff}, usually around $z = 1.1$.

Figs. 4.6b, 4.7b, and 4.8b show the density profiles at pressures above the monolayer transition but below the freezing transition. Fig. 4.6b is at a reduced pressure of 1.0×10^{-5}; the peak has narrowed and the height has increased significantly resulting from pore condensation. Fig. 4.7b is at a reduced pressure of 1.0×10^{-5} and shows pore condensation. There is also a shoulder on the peak near 2 σ, which is the result of the peak interacting with its corresponding peak across the center line which originates from the right wall (not shown). While Fig. 4.8b is at a reduced pressure of 2.5×10^{-4}, it does not show pore condensation.

Figs. 4.6c, 4.7c, and 4.8c are density profiles above the freezing point transition. Fig. 4.6c is at a reduced pressure of 1.0×10^{-3}. The base of the peak has narrowed considerably and the height has more than doubled as it transversed the freezing point transition. Fig. 4.7c has a reduced pressure of 1.0. The height of the peaks has increased significantly and the shoulder on the peak at 2 σ has become a peak itself. This will be discussed in greater detail later. Fig. 4.8c is at a reduced pressure of 1.0×10^{-3}. It shows a second peak near 2 σ with a smaller peak next to it. This smaller peak is resulting from the larger peak interacting with its mirror image across

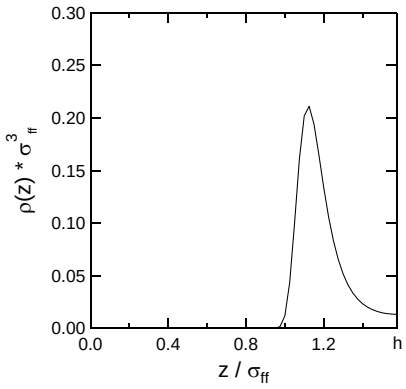

(a)

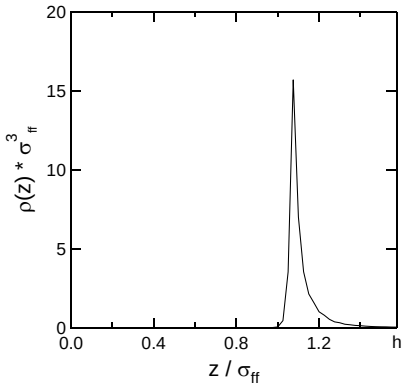

(b)

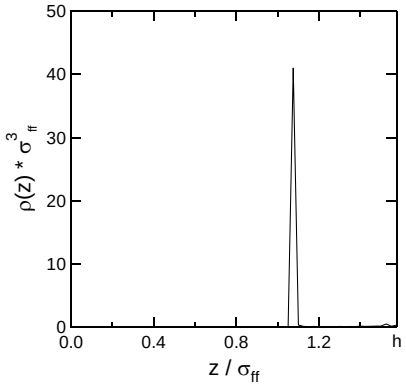

(c)

Figure 4.6: Nitrogen density profiles in a 0.564 nm pore, h = 1.575. a) $P/P_o = 1.0\times10^{-6}$, b) $P/P_o = 1.0\times10^{-5}$, c) $P/P_o = 1.0\times10^{-3}$.

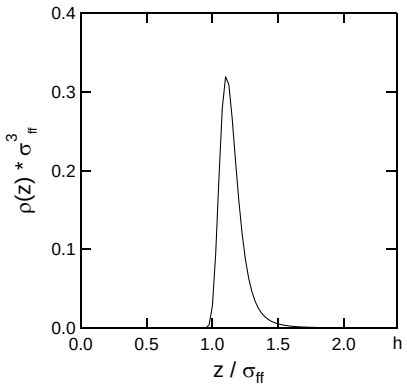

(a)

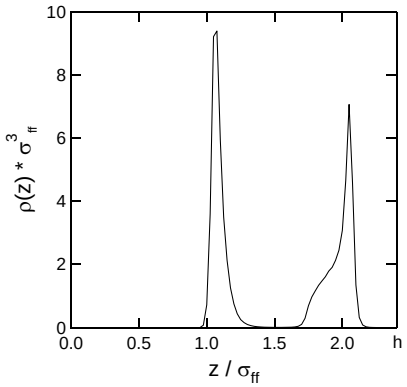

(b)

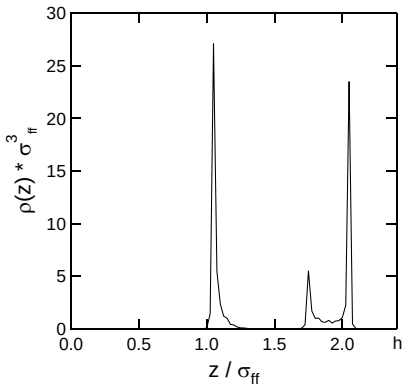

(c)

Figure 4.7: Nitrogen density profiles in a 0.991 nm pore, h = 2.4. a) $P/P_o = 1.0\times10^{-5}$, b) $P/P_o = 1.0\times10^{-2}$, c) $P/P_o = 1.0$.

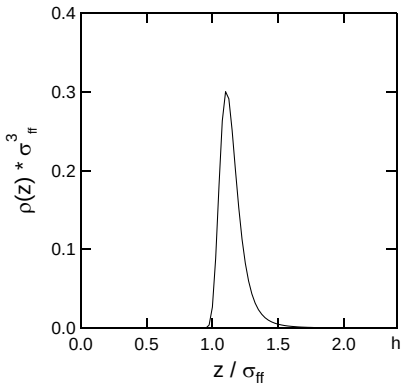

(a)

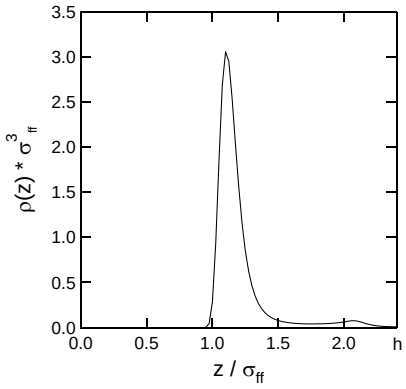

(b)

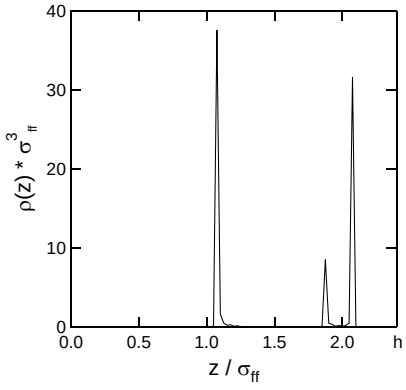

(c)

Figure 4.8: Nitrogen density profiles in a 1.03 nm pore, h = 2.475. a) P/P_o = 5.0×10^{-5}, b) $P/P_o = 2.5\times10^{-4}$, c) $P/P_o = 1.0\times10^{-3}$.

the center line.

Fig. 4.9 shows the density profile of Figs. 4.6c, 4.7c, and 4.8c, but as a full pore width. This was done to demonstrate the interactions of the larger peaks across the centerline which results in the smaller peaks. Fig. 4.9a shows the full pore profile of Fig. 4.6c. It shows two distinct peaks. There are no shoulders, or smaller peaks, because the two peaks are 1 σ apart. For pores that are slightly off the 0.564 Å pore there is no evidence of the freezing transition. The peak is broader and more diffuse. Fig. 4.9b is the full pore profile of Fig. 4.7c. The interactions of the large pores in the center of the pore with the smaller pores becomes easier to see. The large peak at 2 σ and the small peak at 3σ are 1 σ apart, the same is true for the reverse. Fig. 4.9c is the full pore profile of Fig. 4.8c. The peaks just after 1 σ, 2 σ, and just before 3 σ, and 4 σ correspond to the main centers of the molecules, whereas the small peaks just before 2 σ and 3 σ are induced by the larger peaks after 2 σ and just before 3 σ, respectively. The peak before 2 σ and just before 3 σ are separated by a distance of 1 σ. The same applies to the other set of peaks. Thus, Figs. 4.9b and 4.9c each show three peaks a distance σ_{ff} apart emanating from the left wall and three peaks a distance σ_{ff} apart emanating from the right wall.

The average excess density in the pores is calculated by integrating density profiles over the pore width using eq. 4.35. Fig. 4.10 shows the average density for nitrogen in a 0.564 nm, 0.991 nm, and 1.03 nm pore. The isotherm for the 0.564 nm pore shows the monolayer transition occurring at a reduced pressure of 1×10^{-6} with the freezing transition at 1×10^{-5}. The 0.991 nm pore isotherm has the monolayer transition around 1×10^{-4} with the condensation step near 3×10^{-4} and the freezing transition happening over a broad range of pressures. For the 1.03 nm pore the formation of the monolayer starts at a reduced pressure of 1×10^{-4} and the transition into the solid phase at a reduced pressure of 3×10^{-4}. This shows that as the pore size increases, the monolayer transition shifts to higher pressures. The shifting of the

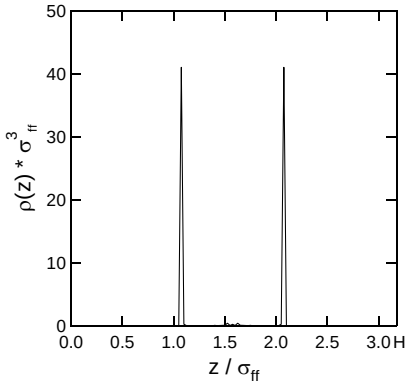

(a)

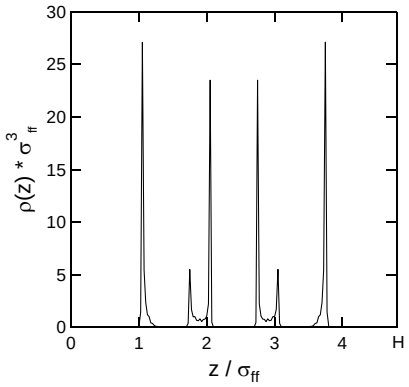

(b)

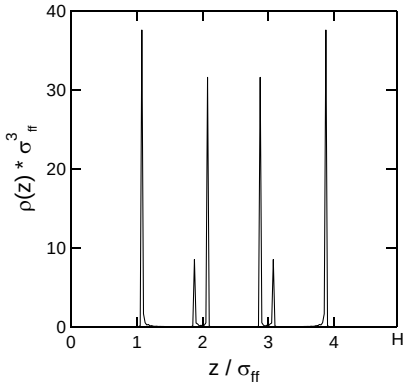

(c)

Figure 4.9: Full pore width density profile of nitrogen at 77 K. a) a 0.564 nm pore at $P/P_o = 1.0\times10^{-3}$, H = 1.575, b) a 0.991 nm pore at $P/P_o = 1.0$, H = 2.4, c) a 1.03 nm pore at $P/P_o = 1.0\times10^{-3}$, H = 2.475.

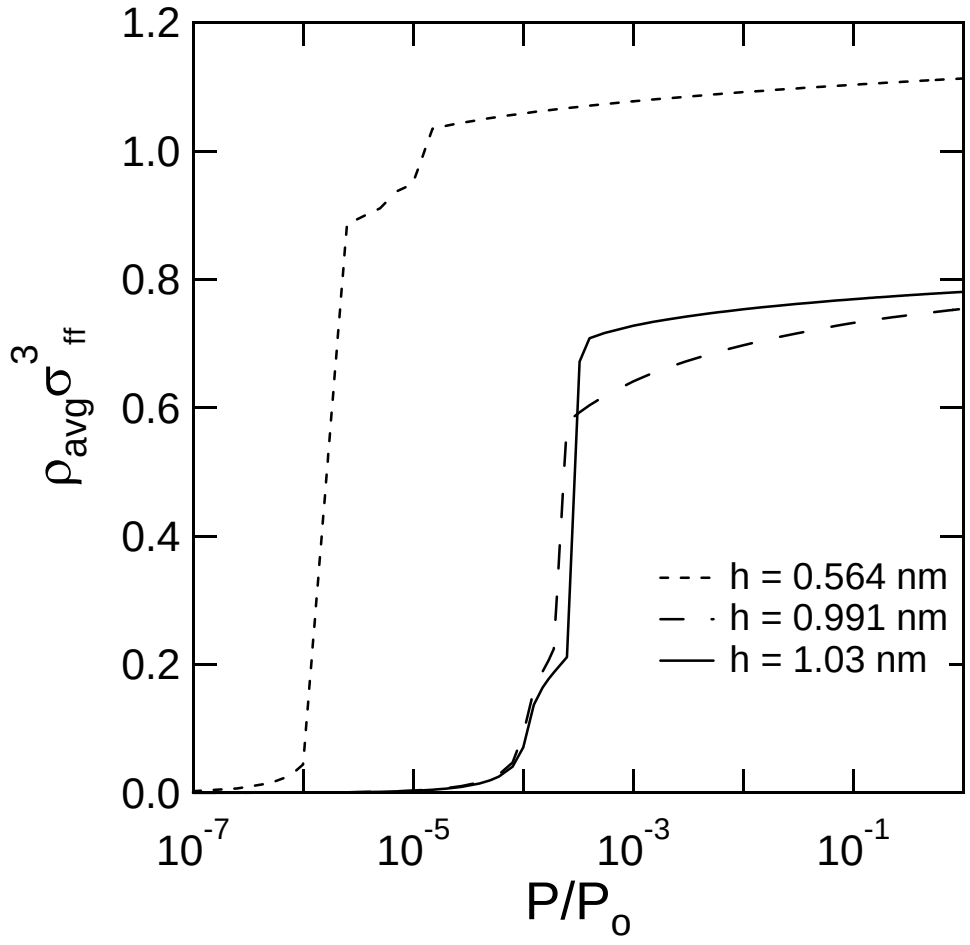

Figure 4.10: Average density of nitrogen in a 0.564nm, 0.991 nm, and 1.03 nm pore at 77 K.

monolayer transition continues up to pores near 1 nm. For pores larger than 1 nm the monolayer transition remains in the same place, but the pore condensation and freezing transitions are moved to higher pressures.

Fig. 4.11 shows the PSD calculations for eq. 4.37 with three modes. Thirty different pore isotherms like those shown in Fig. 4.10 were used in the calculations, with 4 Å pores used as the minimum size. The nitrogen isotherm used in the calculations was from Russell and LeVan.[83] There is a peak centered at 5.6 Å with a broad tail in larger pores. The PSD was also run with four modes but no substantial differences were seen.

Fig. 4.12 is the calculated isotherm based on the calculated PSD with three modes. The calculated isotherm describes the data well.

Pentane

For n-pentane the data from Avgul and Kiselev[85] were used to estimate the parameters, using the procedure described in Section . Results are given Table 4.1. The parameters were fit using the pressure range from 0.01 up to 10 kPa. The carbon used was a graphatized carbon black with a BET surface area of 12.2 m^2/g. Again, a pore with a half width of $h = 20\ \sigma_{ff}$ was used to simulate a non-porous surface, with results shown in Fig. 4.13.

Fig. 4.14 shows the density profiles, calculated using eq. 4.32, for a pore width of 4.81 Å. Fig. 4.14a shows the density profile of n-pentane at a pressure of 6.2×10^{-7} kPa; the system is well below the monolayer transition. Fig. 4.14b shows the density profile at a pressure of 1.16×10^{-4} kPa; at this pressure the system has gone through condensation. Fig. 4.15 shows the density profiles for a pore of width 6.07 Å. Fig. 4.15a is at a pressure of 6.2×10^{-7} kPa, which is well below the monolayer transition. Fig. 4.15b is at a pressure of 3.5×10^{-3} kPa, and the fluid in the pore has condensed. Fig. 4.16 shows the average density profiles, calculated with eq. 4.10,

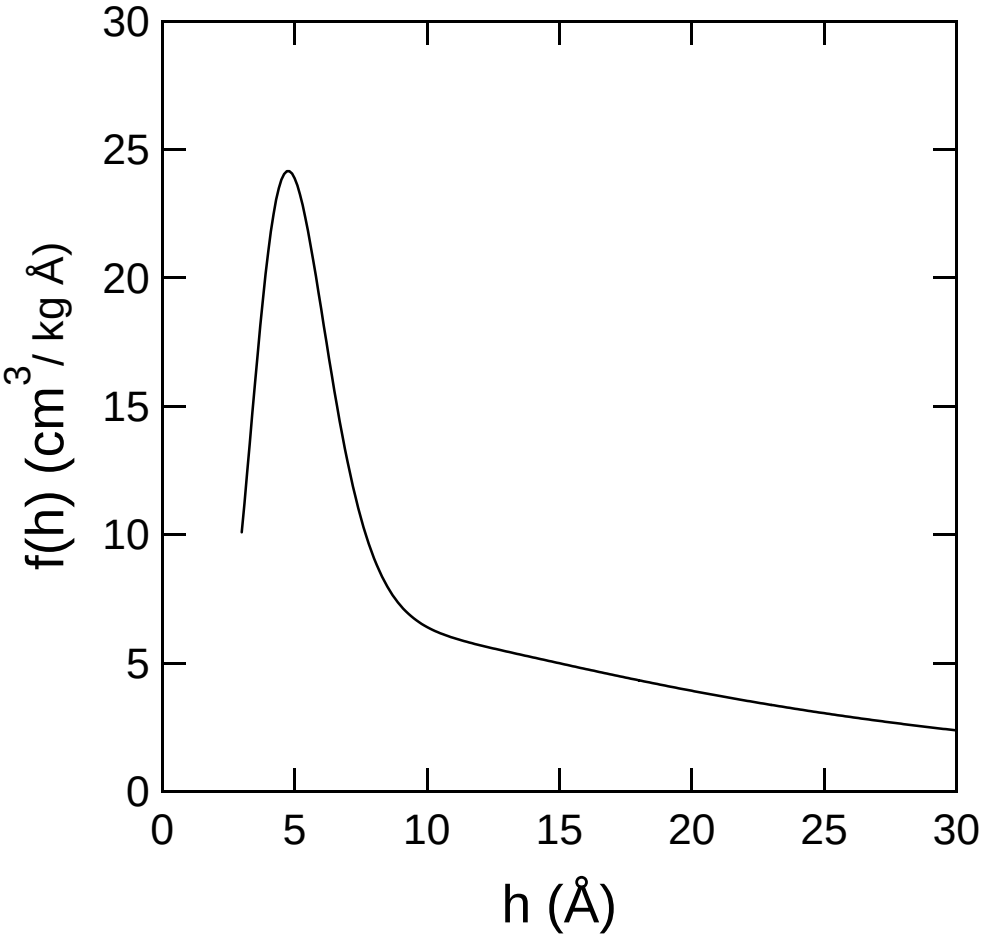

Figure 4.11: Pore size distribution calculated from nitrogen density profiles with three modes in eq. 4.37.

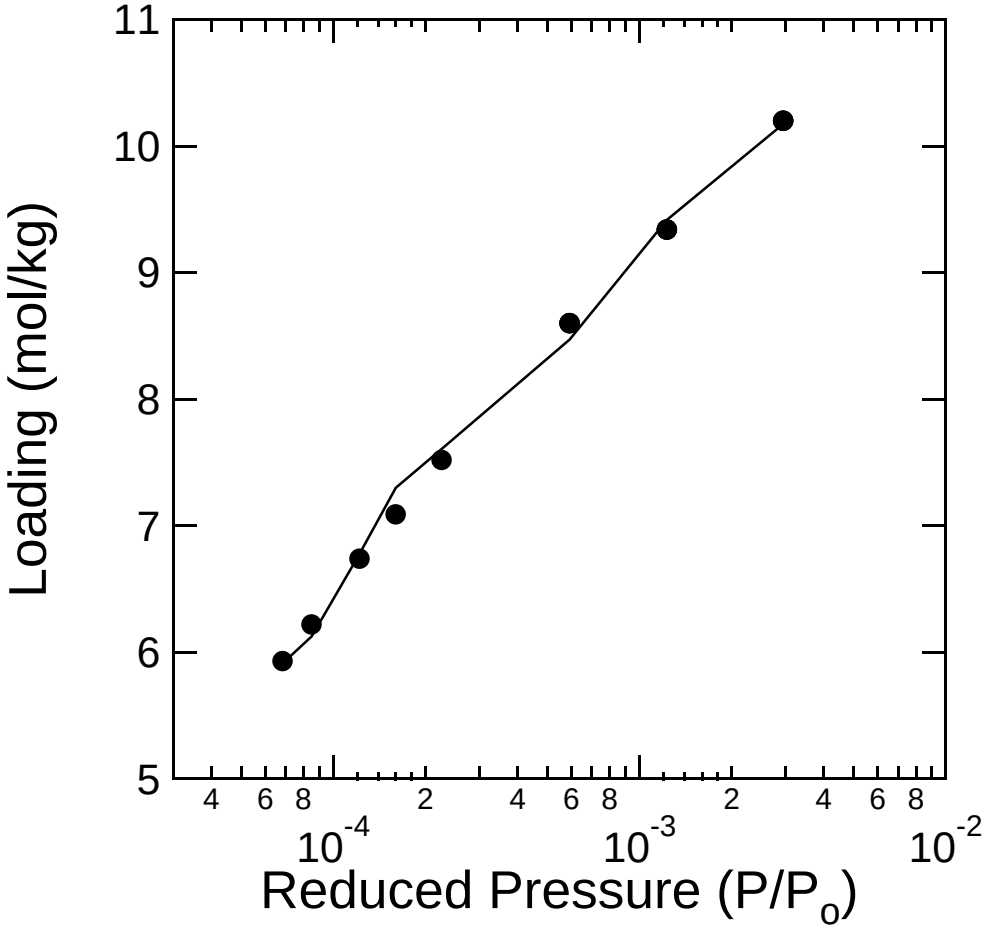

Figure 4.12: Nitrogen isotherm at 77 K on BPL activated carbon. Solid line is the calculated isotherm.

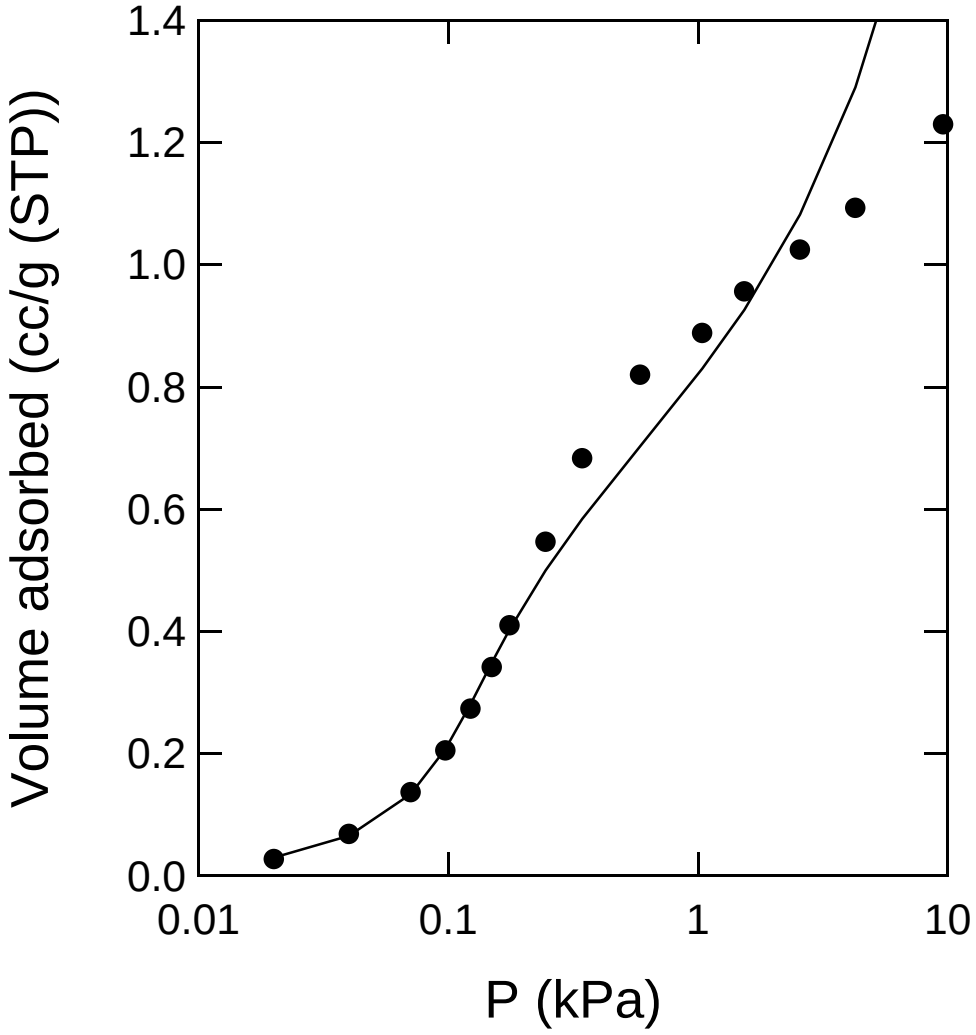

Figure 4.13: Comparison of experimental and theoretical adsorbed volumes of pentane on nonporous carbon black at 293.15 K. The points are experimental data. The solid line is the model predictions.

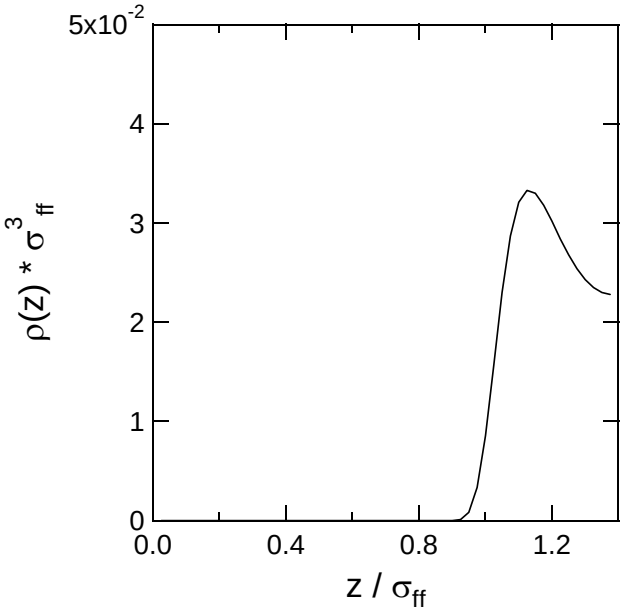

(a)

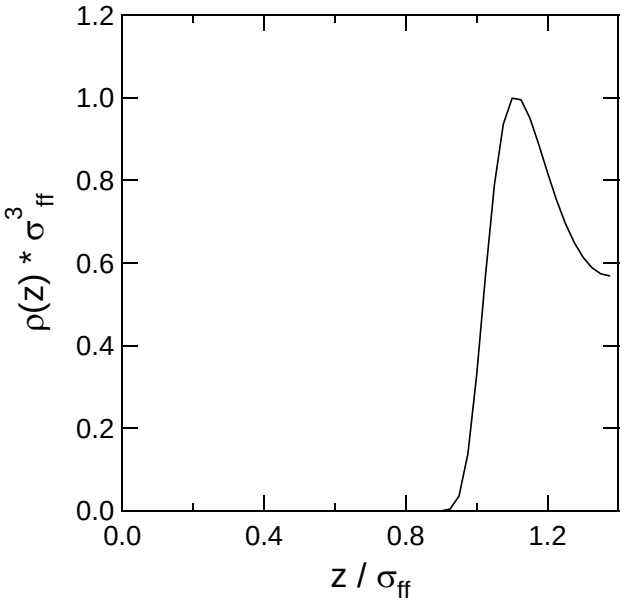

(b)

Figure 4.14: n-pentane density profiles in a 4.81 Å pore. a) P = 6.2×10^{-7} kPa, b) P = 1.16×10^{-4} kPa.

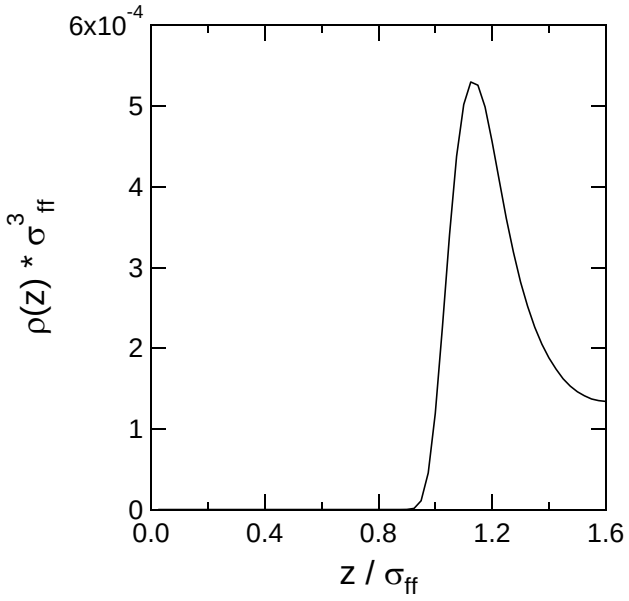

(a)

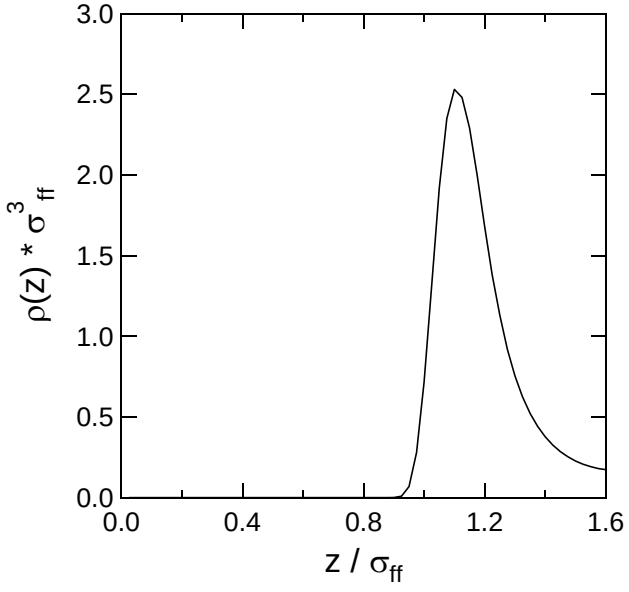

(b)

Figure 4.15: n-pentane density profiles in a 6.07 Å pore. a) P = 6.2×10^{-7} kPa, b) P = 3.5×10^{-3} kPa.

for pores of size 4.81 Å, 6.07 Å, and 9.98 Å. The position at which the condensation steps ends in the pores of width 4.81 Å and 6.07 Å, with the isotherms flattening out, are apparent. Also, it can be seen that fluid in the pore of width 9.98 Å does not go through condensation. This follows also for larger pores in the pressure range examined.

The density profiles were calculated at 25 °C and compared with adsorption data for n-pentane on BPL activated carbon from Schindler *et al.*[86] Using the PSD calculated with the nitrogen model an isotherm for n-pentane was determined by combining the PSD, eq. 4.37, with the adsorption integral equation, eq. 4.36, using forty calculated pore isotherms for pentane. The calculated isotherm is shown in Fig. 4.17 as the solid curve. There is good agreement between the data and the model predictions over a wide range of pressures. However, the data points of Schindler *et al.*[86] are not for pure n-pentane, but a binary mixture of n-pentane in nitrogen carrier gas. If the ideal adsorbed solution theory is used to calculate the effect of the nitrogen at the lowest loadings, it shows that the n-pentane partial pressure is increased significantly. However, we believe that this is not entirely correct because of a few reasons. Ideal adsorbed solution theory was developed for a homogeneous surface. In the Henry's law region, n-pentane is finding the high energy sites to adsorb on in the heterogeneous BPL carbon, and these sites are not influenced much by nitrogen. In the loading just above 0.01 mol kg^{-1}, where the n-pentane is out of the Henry's law region, we may see the effects of the nitrogen. The n-pentane is adsorbing on lower energy sites and is competing with the nitrogen causing the partial pressure of n-pentane to increase slightly. A difference can be seen between the measured and predicted values in this range. Also, as the loading approaches 1 mol kg^{-1} the effects of the nitrogen are diminishing because the n-pentane is dominating in the system. This is demonstrated by the convergence of the predicted and measured isotherms.

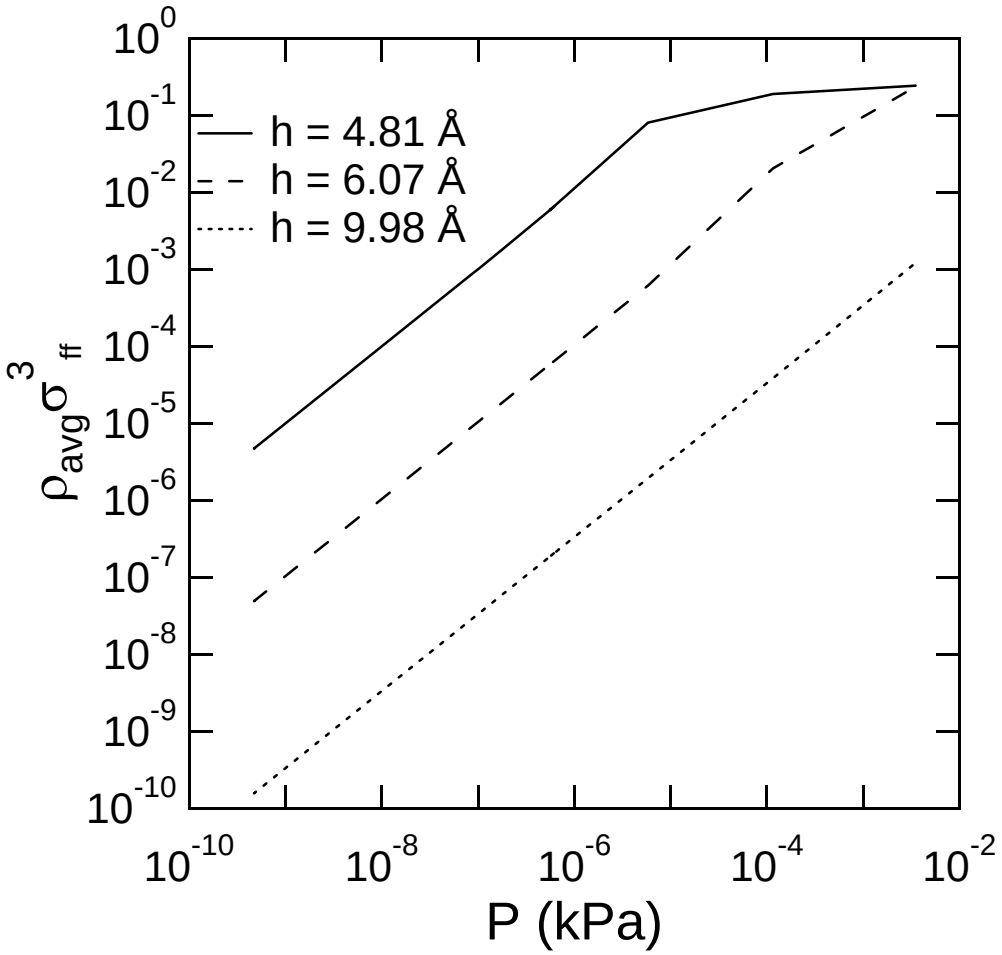

Figure 4.16: Average density of n-pentane in 4.81 Å, 6.07 Å, and 9.98 Å pores at 298.15 K.

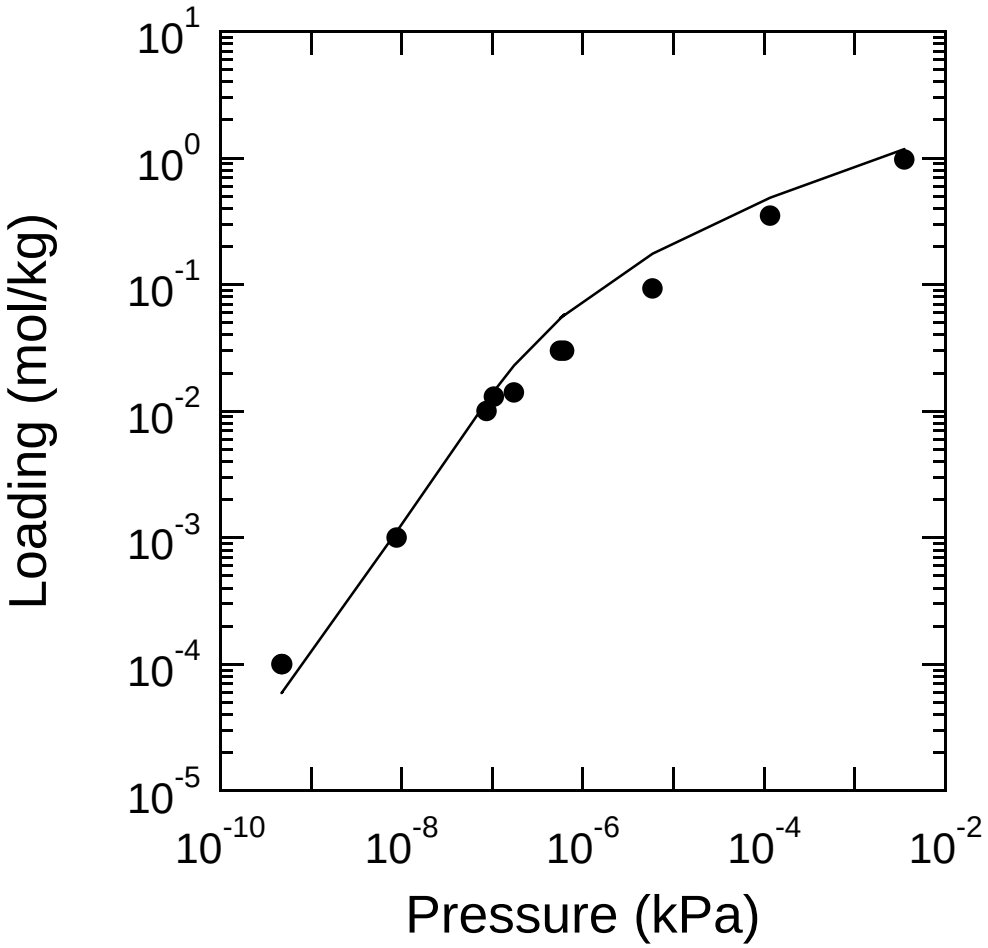

Figure 4.17: Calculated n-pentane isotherm at 25°C on BPL activated carbon. The circles are the data from Schindler *et al.*[86] The solid line is the isotherm based on the pore size distribution calculated by nitrogen.

4.4 Conclusions

A model was developed that adds the SAFT equation of state to DFT. This was achieved by adding, for the first time, a first order attractive term where a mean-field was not assumed, and by the addition of a second order attractive term. This addition allows molecules to be treated as chain molecules, as opposed to just spherical molecules. The model shows agreement with published Monte Carlo simulation models for hard sphere chains of 3, 4, and 20 monomers near a hard wall. The model was also compared with a 3-mer with a square-well attractive potential near both a hard wall and an attractive wall.

The model was then used to determine the interaction parameters of nitrogen and n-pentane with a carbon wall. The calculated density profiles show the presence of the monolayer transition, pore condensation, and the freezing transition. When the pore size places the larger peaks closer than 1 σ apart in the center of the pore, apparent layering interactions are created. These turn into minor peaks surrounding the major peak. The freezing transition has also been observed with the bases of the peaks narrowing and the heights of the peaks increasing.

The PSD was calculated for BPL activated carbon using a log normal distribution with three modes and measured data for nitrogen at 77 K. The nitrogen isotherm was described well using the pore size distribution.

Density profiles were then calculated for n-pentane. Pore condensation was observed in the smallest pores. An isotherm for n-pentane at 25°C on BPL activated carbon was calculated using the density profiles and the pore size distribution calculated from the nitrogen data. There is good agreement between the measured and predicted isotherms. However, the data points are for a mixture of nitrogen and n-pentane. This is believed to affect only the data in the mid range, out of the Henry's law region but before the n-pentane begins to dominate the adsorption space.

References

[1] G. J. Gloor, G. Jackson, F. J. Blas, E. M. Rio, and E. Miguel, J. Chem. Phys. **121**, 12740 (2004).

[2] G. J. Gloor, F. J. Blas, E. M. Rio, E. Miguel, and G. Jackson, Fluid Phase Equil. **194-197**, 521 (2002).

[3] P. Tarazona, Phys. Rev. A **31**, 2672 (1985); **32**, 3148 (1985).

[4] P. Tarazona, U. Marini Bettolo Marconi; and R. Evans, Mol. Phys. **60**, 573 (1987).

[5] C. Lastoskie, K. E. Gubbins, and N. Quirke, J. Phys. Chem. **97**, 4786 (1993).

[6] C. Lastoskie, K. E. Gubbins, and N. Quirke, Langmuir **9**, 2693 (1993).

[7] R. J. Dombrowski, D. R. Hyduke, and C. M. Lastoskie, Langmuir **16**, 5041 (2000).

[8] D. L. Valladares, F. R. Reinoso, and G. Zgrablich, Carbon **36**, 1491 (1998).

[9] P. I. Ravikovitch, A. Vishnyakov, R. Russo, and A. V. Neimark, Langmuir **16**, 2311 (2000).

[10] M. El-Merraoui, M. Aoshima, and K. Kaneko, Langmuir **16**, 4300 (2000).

[11] P. I. Ravikovitch, A. Vishnyakov, and A. V. Neimark, Phys. Rev. E **64**, 011602 (2001).

[12] M. B. Sweatman, and N. Quirke, Langmuir **17**, 5011 (2001).

[13] S. K. Bhatia, Langmuir **18**, 6845 (2002).

[14] T. Ohba, D. Nicholson, and K. Kaneko, Langmuir **19**, 5700 (2003).

[15] Jagiello, J.; Thommes, M. *Carbon* **2004**, 1227 .

[16] T. X. Nguyen, and S. K. Bhatia, Langmuir **20**, 3532 (2004).

[17] E. A. Ustinov, and D. D. Do, Langmuir **20**, 3791 (2004).

[18] P. I. Ravikovitch, S. C. Ó Domhnaill, A. V. Neimark, F. Schüth, and K. K. Unger, Langmuir **11**, 4765 (1005).

[19] E. A. Ustinov, and D. D. Do, J. Chem. Phys. **120**, 9769 (2004).

[20] Y. Rosenfeld, Phys. Rev. Lett. **63**, 980 (1989).

[21] Y. Rosenfeld, M. Schmidt, H. Lowen, and P. Tarazona, Phys. Rev. E **55**, 4245 (1997).

[22] R. Roth, R. Evans, A. Lang, and G. Kahl, J. Phys: Condens. Matter **14**, 12063 (2002).

[23] P. Bryk, R. Roth, K. R. Mecke, and S. Dietrich, Phys. Rev. E, **68**, 031602 (2003).

[24] S. Figueroa-Gerstenmaier, F. J. Blas, J. B. Avalos, and L. F. Vega, J. Chem. Phys., **118**, 830 (2003).

[25] E. Kierlik, M. L. Rosinberg, Y. Fan, and P. A. Monson, J. Chem. Phys., **101**, 10947 (1994).

[26] A. Malijevsky, J. Chem. Phys., **126**, 134710 (2007).

[27] R. Evans,*Fundamentals of Inhomogenous Fluids* (Marcel Dekker, New Yoork, 1992).

[28] M. S. Wertheim, J. Stat. Phys. **35**, 19 (1984).

[29] M. S. Wertheim, J. Stat. Phys. **35**, 35 (1984).

[30] M. S. Wertheim, J. Stat. Phys. **42**, 459 (1986).

[31] M. S. Wertheim, J. Stat. Phys. **42**, 477 (1986).

[32] E. A. Müller, K. E. Gubbins, Ind. Eng. Chem. Res. **40**, 2193 (2001).

[33] I. G. Economou, Ind. Eng. Chem. Res. **41**, 953 (2002).

[34] A. Gil-Villegas, A. Galindo, P. J. Whitehead, S. J. Mills, G. Jackson, and A. N. Burgess, J. Chem. Phys. **106**, 4168 (1997).

[35] C. McCabe, and G. Jackson, PCCP Phys. Chem. Chem. Phys. **1**, 2057 (1999).

[36] C. McCabe, A. Galindo, and M. N. Garcia-Lisbona, Ind. Eng. Chem. Res. **40**, 3835 (2001).

[37] C. McCabe, and S. B. Kiselev, Fluid Ph. Equil. **219**, 3 (2004).

[38] C. McCabe, and S. B. Kiselev, Ind. Eng. Chem. Res. **43**, 2839 (2004).

[39] C. McCabe, A. Galindo, A. Gil-Villegas, and G. Jackson, Int. J. Thermophys. **19**, 1511 (1998).

[40] C. McCabe, A. Gil-Villegas, and G. Jackson, J. Phys. Chem. B **102**, 4183 (1998).

[41] A. Galindo, L. J. Florusse, and C. J. Peters, Fluid Ph. Equil. **160**, 123 (1999).

[42] E. J. M. Filipe, E. de Azevedo, L. F. G. Martins, V. A. M. Soares, J. C. G. Calado, C. McCabe, and G. Jackson, J. Phys. Chem. B **104**, 1315 (2000).

[43] E. J. M. Filipe, L. F. G. Martins, J. C. G. Calado, C. McCabe, and G. Jackson, J. Phys. Chem. B **104**, 1322 (2000).

[44] L. M. B. Dias, E. J. M. Filipe, C. McCabe,and J. C. G. Calado, J. Phys. Chem. B **108**, 7377 (2004).

[45] L. X. Sun, H. G. Zhao, S. B. Kiselev, and C. McCabe, Fluid Ph. Equil. **228**, 275 (2005).

[46] L. X. Sun, H. G. Zhao, S. B. Kiselev, and C. McCabe, J. Phys. Chem. B **109**, 9047 (2005).

[47] H. Zhao, P. Morgado, C. McCabe, and A. Gil-Villegas, J. Phys. Chem. B **110**, 24083 (2006).

[48] L. X. Sun, H. G. Zhao, and C. McCabe, AIChE J. **53**, 720 (2007).

[49] C. McCabe, A. Galindo, A. Gil-Villegas, and G. Jackson, J. Phys. Chem. B **102**, 8060 (1998).

[50] P. Morgado, C. McCabe, and E. J. M. Filipe, Fluid Ph. Equil. **228**, 389 (2005).

[51] P. Morgado, H. Zhao, F. J. Blas, C. McCabe, L. P. N. Rebelo, and E. J. M. Filipe, J. Phys. Chem. B **111**, 2856 (2007).

[52] L. M. B. Dias, R. P. Bonifacio, E. J. M. Filipe, J. C. G. Calado, C. McCabe, and G. Jackson, Fluid Ph. Equil. **205**, 163 (2003).

[53] C. McCabe, A. Galinod, and P. T. Cummings,J. Chem. Phys. B **107**, 12307 (2003).

[54] A. Valtz, A. Chapoy, C. Coquelet, P. Paricaud, and D. Richon, Fluid Ph. Equil. **226**, 333 (2004).

[55] A. Galindo, A. Gil-Villegas, P. J. Whitehead, G. Jackson, and A. N. Burgess, J. Phys. Chem. B **102**, 7632 (1998).

[56] A. Galindo, and F. J. Blas, J. Phys. Chem. B **106**, 4503 (2002).

[57] C. M. Colina, G. Galindo, F, J. Blas, and K. E. Gubbins, Fluid Ph. Equil. **222**, 77 (2004).

[58] C. M. Colina, and K. E. Gubbins, J. Phys. Chem. B **109**, 2899 (2005).

[59] D. Chandler, J. D. McCoy, and S. J. Singer, J. Chem. Phys. **85**, 5971 (1986).

[60] D. Chandler, J. D. McCoy, and S. J. Singer, J. Chem. Phys. **85**, 5977 (1986).

[61] J. D. McCoy, S. J. Singer, and D. Chandler, J. Chem. Phys. **87**, 4853 (1987).

[62] J. Forsman, and C. E. Woodward, J. Chem. Phys. **119**, 1889 (2003).

[63] A. Yethiraj, and C. E. Woodward, J. Chem. Phys. **102**, 5499 (1995).

[64] Z. C. Ye, J. Cai, H. L. Liu, and Y. Hu, J. Chem. Phys. **123**, 194902 (2005).

[65] Z. C. Ye, H. Y. Chen, H. L. Liu, Y. Hu, and J. W. Jiang, J. Chem. Phys. **126**, 134903 (2007).

[66] S. Tripathi, and W. G. Chapman, J. Chem. Phys. **122**, 094506 (2005).

[67] A. Dominik, S. Tripathi, and W. G. Chapman, Ind. Eng. Chem. Res. **45**, 6785 (2006).

[68] S. Jain, A. Dominik, and W. G. Chapman, J. Chem. Phys. **127**, 244904 (2007).

[69] Y. X. Yu, and J. Z. Wu, J. Chem. Phys. **116**, 7094 (2002).

[70] Y. X. Yu, and J. Z. Wu, J. Chem. Phys. **117**, 2368 (2002).

[71] Y. X. Yu, J. Z. Wu, Y. X. Xin, and G. H. Gao, J. Chem. Phys. **121**, 1535 (2004).

[72] J. Chang, and S. I. Sandler, Molecular Physics **81**, 735 (1994).

[73] L. Verlet, and J. J. Weis, Phys. Rev. A **5**, 939 (1972).

[74] B. H. Patel, H. Docherty, S. Varga, A. Galindo, and G. C. Maitland, Molecular Physics **103**, 129 (2005).

[75] B. J. Zhang, Chem. Phys. Lett. **296**, 266 (1998).

[76] B. J. Zhang, Fluid Phase Equil. **154**, 1 (1999).

[77] B. J. Zhang, Fluid Phase Equil. **180**, 182 (2001).

[78] Steele, W. A. *Surf. Sci.* **1973**, 36, 317 .

[79] E. Kierlik, M. L. Rosinberg, J. Chem. Phys. **100**, 1716 (1994).

[80] R. Dickman, C. K. Hall, J. Chem. Phys. **89**, 3168 (1988).

[81] A. Yethiraj, C. E. Woodward, J. Chem. Phys. **102**, 5499 (1995).

[82] M. Kruk, Z. Li, and M. Jaroniec, Langmuir **15**, 1435 (1999).

[83] B. P. Russell, and M. D. LeVan, Carbon **32**, 845 (1994).

[84] N. A. Seaton, J. P. R. B. Walton, and N. Quirke, Carbon **27**, 853 (1989).

[85] N. N. Avgul, and A. V. Kiselev.(1970) In. Chemistry and Physics of Carbon. P. Walker (Eds.) Vol. 6, M. Dekker, New York, pg 1-124.

[86] B. J. Schindler, L. C. Buettner, and M. D. LeVan, Carbon, **46**, 1285 (2008).

CHAPTER V

CONCLUSIONS AND RECOMMENDATIONS

The research in this dissertation is centered around three main themes. The first is the measurement of adsorption equilibrium data into the Henry's law region. The second area is the isosteric heat of adsorption calculated as a function of the pore width in the Henry's law region and determination of the pore width for which the isosteric heat is a maximum. Finally, the third area is in the modification of density functional theory to model chain fluids.

Chapter II

In this chapter, two new methods were used to prepare pre-equilibrated adsorption samples at known loadings down to loadings of 0.0001 mol kg^{-1}. The samples were analyzed using a purge and trap method that allowed measurement into the Henry's law region. The adsorption data were compared with three known adsorption isotherms and how well they fit the data as it transitions into the Henry's law region. This is the first time that adsorption was measured into the Henry's law region for an adsorbate that is a liquid at room temperature. The conclusions for this chapter can be summarized as

- A new method for preparing samples at known loading from 1.0 down to 0.0001 mol kg^{-1} by liquid or gas injections was introduced.
- Isotherms for n-pentane on BPL activated carbon at temperatures from 0 to 175^{o} were measured using a purge and trap method.
- The measured isotherms entered into the Henry's law region.
- The transition into the Henry's law region happened near a loading of 0.01 mol kg^{-1} for all temperatures.

- The DR equation and the Langmuir equation were shown not to describe the data well over its range.
- The Toth equation was shown to describe the data well over the range of pressure and temperature.
- The isosteric heat of adsorption was shown to increase with decreased loading, but levels off entering the Henry's law region.

Chapter III

In this section the isosteric heat of adsorption was calculated as a function of pore width in the Henry's law region for parallel slit pores. The conclusions are

- The isosteric heat of adsorption was calculated as a function of the pore width.
- The theoretical maximum isosteric heat of adsorption is 15 - 50 % higher than the values typically calculated from adsorption isotherms of materials with pore size distributions.
- The pore size of the maximum isosteric heat of adsorption is a strong function of the collision diameter and a weak function of the well depth potential. It occurs in a pore size only slightly larger than the collision diameter.
- Carbon materials with parallel slit pores used for adsorptive storage will not be suitable for hydrogen but could be acceptable for methane, if designed correctly.

Chapter IV

This section examined the modification of density functional theory to model chain molecules in parallel slit pores. The statistical associating fluid theory equation of state was included to achieve this. We conclude the following

- DFT was modified to include the ability to model chains with a first and second order attractive potential.
- The model was used to estimate parameters for nitrogen and n-pentane adsorption in carbon parallel slit pores.
- The monolayer transition was observed as a function of pore width, along with condensation and the freezing transition.
- To the best of our knowledge, the freezing transitions observed have the sharpest density profiles that have been found for adsorption in a slit pore.
- The nitrogen model was used to calculate a pore size distribution for BPL activated carbon.
- The calculated pore size distribution was used to calculated an isotherm for n-pentane.

Recommended future work

There are many possibilities for this work to be extended in the future.

- The n-pentane isotherms can be measured with helium as a carrier gas, eliminating the effect of nitrogen. The pure n-pentane data, along with the data in this work can be used to explore how the ideal adsorbed solution theory works when one component is in the Henry's law region while the other is not.
- The experimental techniques developed for ultralow concentration adsorption equilibrium of n-pentane on BPL activated carbon can also be used in the study of other adsorbates and adsorbents and also for mixtures.
- The maximum value of the isosteric heat of adsorption can be calculated for different pore geometries, such as cylindrical.

- Isotherms for different molecules can be calculated from density functional theory at higher pressures and loadings than those in this work.

APPENDIX A

SAMPLE PREPARATION

A.1 Initial preparation work

The activated carbon was ground from a 6 × 16 mesh to a 40 × 50 mesh with a mortar and pestle and sieved to separate. A large amount of activated carbon was regenerated by placing it in an adsorption bed in an oven at 200 °C. Helium gas was used as a carrier gas at a flow rate of 0.5 L/min for 8 hours. While the carbon was regenerating, a number was scratched on the bottom of the glass vial for identification purposes. The glass vial was then weighed empty and the weight was recorded. After the activated carbon was regenerated, approximately 2 grams were placed in the vial and weighed. The weight of the amount of carbon placed in the vial was calculated and recorded. For samples of 0.01 mol kg^{-1} and above liquid injections were used. For samples with loadings 0.01 mol kg^{-1} or lower gas injections were used.

After the samples were prepared by the methods described in the following two sections, the ampules were leak checked by submersion in water. The samples were then strapped to a ferris wheel arrangement in an environmental chamber, heated to 150 °C, and rotated end-over-end at 4 rpm for days to months to increase the mixing of the solid and gas phases as equilibrium was established.

A.2 Liquid Injection

This section is for the preparation of samples with loadings of 0.01 mol kg^{-1} or greater. The glass ampule mentioned in the previous section, which contains 2 grams of regenerated carbon, was connected to the apparatus designed to prepare samples by liquid injection, see Fig. 2.1a. The sample was then heated to 150° and a vacuum was applied to the system for 8 hours, until the system reached a pressure of

0.05 mbar. The sample was removed from the heat, while maintaining a vacuum, and placed in an ice bath. A syringe was used to inject a known amount of n-pentane into the system. Before the syringe was used it was weighed and the system was removed from the vacuum. After the syringe was used it was weighed again to determine the weight of pentane injected into the system. The ampule was then sealed using a micro-torch and the entire sample was weighed to calculate the mass of carbon used.

A.3 Gas Injection

This section is for the preparation of samples with loadings of 0.01 mol kg^{-1} or lower. Instead of injecting a liquid with a syringe, a system was designed to inject a saturated vapor, thus allowing control of the amount injected into the system. This system was designed because of the inability to control the amount injected for amounts less then 1 μL. The system used a temperature bath to control the temperature of a reservoir of pentane allowing us to control the concentration of the vapor phase by use of saturated vapor. The saturated vapor was injected into the system using a six-port valve and a sample loop. The temperature of the bath and the size of the sample loop were determined by the sample size and the desired loading.

The ampule with the regenerated activated carbon was connected to the apparatus shown in Fig. 2.1b. The sample was placed under vacuum and heated to 150°C for 8 hours, until the system reached a pressure of 0.05 mbar. The vacuum downstream of the six-port valve was used to evacuate the system of any impurities. Once the temperature bath was at the desired temperature and the measured pressure was the vapor pressure of the pentane, the ampule was removed from the heat and placed in an ice bath. The sample was removed from the vacuum and the valve was switched exposing the system to the vapor in the sample loop. The ampule was then sealed with a micro-torch and weighed to calculate the mass of activated carbon.

APPENDIX B

OPERATION PROCEDURE FOR THE DYNATHERM SYSTEM

The operating procedure for running the Dynatherm system through the LabVIEW program was important for measuring accurate data into the Henry's law region. Before starting, the program PCswitch needs to be set to "GConly" and the GC is on. The GC software program ChemStation is started. As the software is booting up, it asks about addons, click yes. In the Run Control menu for ChemStation, click on Sample Info option. Give the samples a name. To name the samples I used a format of MMDDYY#, where the # is the number of samples run that day; I started with A. Do not forget to reset the counter number to 1, this is the number of runs done on that sample; it will automatically increase after each run. On the Dynatherm set the value for Dry, Heat, Cool, Trap, and Recyle. Set Dry to zero minutes. The value of Heat was determined by experimentation to determine the time step that fully regenerates the sample tube, but the sample does not break through the focusing trap; it was set to four minutes. Set Cool to zero minutes. The value of Trap was determined by them same method as the value of Heat; it was set to four minutes. The value of Recycle determines the system recovery time if it is desired to run the system without the labview program.

The following procedure is how to set and use the LabVIEW program that controls the Dynatherm.

1. Open program LV7_0VaporPressure_II_mod3.vi

2. On front page

    - Hit the run button
    - GC Run time box

- Set the value to the length of the GC run. The value *must* be smaller than the total run time set in the method file.

- Dynatherm Runtime box
  - Sets the value the dynatherm runs. Is equal to the sum of external, Dry, Heat, and Cool.

3. Go to the Configure menu

   (a) Click on Sampling

   - Make sure that the mode is set to continous
   - In the operate menu, click Apply now
   - In the file menu, click done

   (b) Click on Experiments

   - Check the operator name, change if necessary
   - In the General section change to following if necessary
     i. Chemical name
     ii. Retention time
     iii. Tol (+/-)
   - In the Profiles section change
     i. External Sample time. Set to the value that the dynatherm will be collecting sample.
     ii. Cylcle time. This is equal to the total of the dynatherm run time (external+dry+heat+cool) plus the GC run time plus any time to let the system cool down
     iii. The temp, MFC settings are for the report only, does not change anything
   - Click on the Write File button.

- Name the file
- Use Dynatherm = yes
- Water bath present = no
- SCXI Present = no

4. In the operate menu click Run Now
5. When ready click start

To make permanent changes to the tables in the experiment section

1. Hit the stop button to stop the program
2. In the Browse menu go to the menu of This VI's sub VI's
   - Click on the VI "WriteSetUp_Plot_II.vi"
     - In the browse menu click on This VI's sub VI's
       * Click on the VI "SetUpGlobal_Plot_II.vi"
       * Make the changes in the tables as necessary
         · To remove all entries from the table. Place cursor on the left side of the table. Right click and chose data operations and click on Empty Table
       * In the operate menu click on make current values default
       * In the file menu click on save
       * Close the vi
     - Close the vi

APPENDIX C

EXPERIMENTAL SETTINGS

Table C.1: HP 5890 Series II GC Settings

Column Type:	HP-VOC Capillary (75 m × 0.53mm × μm)			
Method name	PENTANE.M			
Carrier Gas:	Nitrogen: 10 cc/min			
	initial temperature °C	Ramp Rate (°C / min)	Final Temperature °C	Hold time (min)
Oven Temp:	35	0	35	4
	35	70	100	5
	100	50	195	0
	195	-70	35	0
Inlet Temp:	175 °C			
Detector A:	Flame Ionization Detector (FID)			
Det A Temp:	250 °C			
Air Pressure:	36.3 PSI			
H_2 Pressure:	19.0 PSI			

Table C.2: Dynatherm settings

Temperature Settings (°C):	Valve	Transfer line
	150	175
	Tube	Trap
	Desorb 310	350
	Idle 25	25

Time Settings (min) :	Ext	Dry
	—	0
	Heat	Cool
	4	0
	Trap	Recycle
	4	—

APPENDIX D

DENSITY FUNCTIONAL EQUATIONS

D.1 DFT

Density functional theory is based on a grand potential function

$$\Omega[\rho(\mathbf{R})] = F + \int \rho(\mathbf{R})[V_{ext}(\mathbf{R}) - \mu]d\mathbf{R} \tag{D.1}$$

where $\rho_M(\mathbf{R})$ is the density profile of a chain molecule and $\mathbf{R} \equiv (\mathbf{r}_1, \mathbf{r}_2, \cdots, \mathbf{r}_M)$ is the position vector. We are solving

$$\frac{\delta\Omega[\rho(\mathbf{r})]}{\delta\rho(\mathbf{r})} = 0 \tag{D.2}$$

where $\rho(\mathbf{r})$ is the segment density profile, and the Helmholtz free energy F is split up into the ideal part

$$F_{id}[\rho(\mathbf{r})] = kT \int \rho(\mathbf{r}) \left[\ln(\Lambda^3\rho(\mathbf{r})) - 1\right] d\mathbf{r} \tag{D.3}$$

and

$$\frac{\delta F_{id}[\rho(\mathbf{r})]}{\delta\rho(\mathbf{r})} = kT \ln(\Lambda^3\rho(\mathbf{r})) \tag{D.4}$$

where Λ is the deBroglie wavelength, T is the temperature, and k is Boltzmann's constant. The hard sphere energy is

$$F_{hs}[\rho(\mathbf{r})] = kT \int \Phi_{hs}[n_i(\mathbf{r})]d\mathbf{r} \tag{D.5}$$

and

$$\frac{\delta F_{hs}[\rho(\mathbf{r})]}{\delta\rho(\mathbf{r})} = \int \sum_i \frac{\partial\Phi_{hs}}{\partial n_i(\mathbf{r})}\bigg|_{\mathbf{r}'} \frac{\delta n_i(\mathbf{r}')}{\delta\rho(\mathbf{r})} d\mathbf{r}' \tag{D.6}$$

where

$$\Phi_{hs}(\mathbf{r}) = \Phi_{hs1} + \Phi_{hs2} + \Phi_{hs3} \tag{D.7}$$

$$\Phi_{hs1} = -n_0 \ln(1 - n_3) \tag{D.8}$$

$$\Phi_{hs2} = \frac{n_1 n_2 - \mathbf{n}_{V1} \cdot \mathbf{n}_{V2}}{1 - n_3} \tag{D.9}$$

$$\Phi_{hs3} = \frac{(n_2^3 - 3n_2 \mathbf{n}_{V2} \cdot \mathbf{n}_{V2})(n_3 + (1 - n_3)^2 \ln(1 - n_3))}{36\pi n_3^2 (1 - n_3)^2} \tag{D.10}$$

where

$$n_i(\mathbf{r}) = \int \rho(\mathbf{r}') \omega_i(\mathbf{r} - \mathbf{r}') d\mathbf{r}' \tag{D.11}$$

$$i = 0, 1, 2, 3, V1, V2$$

$$\omega_3(r) = \Theta(R - r) \tag{D.12}$$

$$\omega_2(r) = |\nabla \Theta(R - r)| = \delta(R - r) \tag{D.13}$$

$$\omega_1(r) = \frac{\omega_2(r)}{4\pi R} \tag{D.14}$$

$$\omega_0(r) = \frac{\omega_2(r)}{4\pi R^2} \tag{D.15}$$

$$\omega_{V2}(\mathbf{r}) = \nabla \Theta(R - r) = \frac{\mathbf{r}}{r} \delta(R - r) \tag{D.16}$$

$$\omega_{V1}(\mathbf{r}) = \frac{\omega_{V2}(\mathbf{r})}{4\pi R} \tag{D.17}$$

$$n_3(z) = \pi \int_{z-R}^{z+R} \rho(z')[R^2 - (z' - z)^2] dz' \tag{D.18}$$

$$n_2(z) = 2\pi R \int_{z-R}^{z+R} \rho(z') dz' \tag{D.19}$$

$$\mathbf{n}_{V2}(z) = \left(-2\pi \int_{z-R}^{z+R} \rho(z')(z' - z) dz' \right) \hat{\mathbf{z}} \equiv n_{V2} \hat{\mathbf{z}} \tag{D.20}$$

$$\frac{\partial \Phi_{hs}}{\partial n_0} = -\ln(1 - n_3) \tag{D.21}$$

$$\frac{\partial \Phi_{hs}}{\partial n_1} = \frac{n_2}{1 - n_3} \tag{D.22}$$

$$\frac{\partial \Phi_{hs}}{\partial n_2} = \frac{n_1}{1 - n_3} + \frac{(n_2^2 - \mathbf{n}_{V2} \cdot \mathbf{n}_{V2})(n_3 + (1 - n_3)^2 \ln(1 - n_3))}{12\pi n_3^2 (1 - n_3)^2} \tag{D.23}$$

$$\frac{\partial \Phi_{hs}}{\partial n_3} = \frac{n_0}{1-n_3} + \frac{n_1 n_2 - \mathbf{n}_{V1}\cdot\mathbf{n}_{V2}}{(1-n_3)^2} + \frac{(n_2^3 - 3n_2\mathbf{n}_{V2}\cdot\mathbf{n}_{V2})(n_3 - 2(1-n_3)\ln(1-n_3))}{36\pi n_3^2(1-n_3)^2} - \frac{(n_2^3 - 3n_2\mathbf{n}_{V2}\cdot\mathbf{n}_{V2})(n_3 + (1-n_3)^2\ln(1-n_3))}{18\pi n_3^3(1-n_3)^2} + \frac{(n_2^3 - 3n_2\mathbf{n}_{V2}\cdot\mathbf{n}_{V2})(n_3 + (1-n_3)^2\ln(1-n_3))}{18\pi n_3^2(1-n_3)^3} \tag{D.24}$$

$$\frac{\partial \Phi_{hs}}{\partial n_{V1}} = -\frac{n_{V2}}{1-n_3} \tag{D.25}$$

$$\frac{\partial \Phi_{hs}}{\partial n_{V2}} = -\frac{n_{V1}}{1-n_3} - \frac{n_2 n_{V2}(n_3 + (1-n_3)\ln(1-n_3))}{6\pi n_3^2(1-n_3)^2} \tag{D.26}$$

$$\int \frac{\partial \Phi_{hs}}{\partial n_3}\omega_3(\mathbf{r}-\mathbf{r}')d\mathbf{r}' = \pi\int_{z-R}^{z+R}\left.\frac{\partial \Phi}{\partial n_3}\right|_{z'}[R^2-(z'-z)^2]dz' \tag{D.27}$$

$$\int \frac{\partial \Phi_{hs}}{\partial n_2}\omega_2(\mathbf{r}-\mathbf{r}')d\mathbf{r}' = 2\pi R\int_{z-R}^{z+R}\left.\frac{\partial \Phi}{\partial n_2}\right|_{z'}dz' \tag{D.28}$$

$$\int \frac{\partial \Phi_{hs}}{\partial n_{V2}}\omega_{V2}(\mathbf{r}-\mathbf{r}')d\mathbf{r}' = 2\pi\int_{z-R}^{z+R}\left.\frac{\partial \Phi}{\partial n_{V2}}\right|_{z'}(z'-z)dz' \tag{D.29}$$

the chain energy is

$$F_{chain}[\rho(\mathbf{r})] = kT\int \Phi_{chain}[n_\alpha(\mathbf{r})]d\mathbf{r} \tag{D.30}$$

and

$$\frac{\delta F_{chain}[\rho(\mathbf{r})]}{\delta\rho(\mathbf{r})} = \int\sum_i \left.\frac{\partial \Phi_{chain}}{\partial n_i(\mathbf{r})}\right|_{\mathbf{r}'}\frac{\delta n_i(\mathbf{r}')}{\delta\rho(\mathbf{r})}d\mathbf{r}' \tag{D.31}$$

where

$$\Phi_{chain}(n_\alpha) = \frac{1-M}{M}n_0\zeta\ln y_{hs} \tag{D.32}$$

$$\frac{\partial \Phi_{chain}}{\partial n_0} = \frac{1-M}{M}\zeta\ln y_{hs} \tag{D.33}$$

$$\frac{\partial \Phi_{chain}}{\partial n_2} = \frac{1-M}{M}n_0\left(\frac{\partial\zeta}{\partial n_2}\ln y_{hs} + \zeta\frac{\frac{\partial y_{hs}}{\partial n_2}}{y_{hs}}\right) \tag{D.34}$$

$$\frac{\partial \Phi_{chain}}{\partial n_{V2}} = \frac{1-M}{M}n_0\left(\frac{\partial\zeta}{\partial n_{V2}}\ln y_{hs} + \zeta\frac{\frac{\partial y_{hs}}{\partial n_{V2}}}{y_{hs}}\right) \tag{D.35}$$

$$\frac{\partial \Phi_{chain}}{\partial n_3} = n_0\zeta\frac{\frac{\partial y_{hs}}{\partial n_3}}{y_{hs}} \tag{D.36}$$

$$y_{hs} = \frac{1}{1-n_3} + \frac{n_2\sigma\zeta}{4(1-n_3)^2} + \frac{n_2^2\sigma^2\zeta}{72(1-n_3)^3} \tag{D.37}$$

$$\frac{\partial y_{hs}}{\partial n_2} = \frac{\sigma(\zeta + n_2\frac{\partial\zeta}{\partial n_2})}{4(1-n_3)^2} + \frac{\sigma^2 n_2(2\zeta + n_2\frac{\partial\zeta}{\partial n_2})}{72(1-n_3)^3} \tag{D.38}$$

$$\frac{\partial y_{hs}}{\partial n_{V2}} = \left(\frac{\sigma n_2}{4(1-n_3)^2} + \frac{\sigma^2 n_2^2}{72(1-n_3)^3}\right)\frac{\partial\zeta}{\partial n_{V2}} \tag{D.39}$$

$$\frac{\partial y_{hs}}{\partial n_3} = \frac{1}{(1-n_3)^2} + \frac{\sigma n_2\zeta}{2(1-n_3)^3} + \frac{\sigma^2 n_2^2\zeta}{24(1-n_3)^4} \tag{D.40}$$

and

$$\zeta = 1 - \frac{\mathbf{n}_{V2}\cdot\mathbf{n}_{V2}}{n_2^2} \tag{D.41}$$

$$\frac{\partial\zeta}{\partial n_2} = \frac{2n_{V2}\cdot n_{V2}}{n_2^3} \tag{D.42}$$

$$\frac{\partial\zeta}{\partial n_{V2}} = -\frac{2n_{V2}}{n_2^2} \tag{D.43}$$

The attractive potential is described by thermodynamic perturbation theory, using first-order and second-order terms. The first-order term is described by

$$F_1[\rho(\mathbf{r})] = \frac{1}{2}\int \rho(\mathbf{r}')\int \rho(\mathbf{r}'')g_{hs}[n_3(\mathbf{r}'');\mathbf{r}'']\phi(|\mathbf{r}'-\mathbf{r}''|)d\mathbf{r}''d\mathbf{r}' \tag{D.44}$$

and the derivative is

$$\begin{aligned}\frac{\delta F_1[\rho(\mathbf{r})]}{\delta\rho(\mathbf{r})} &= \int \rho(\mathbf{r}')g_{hs}[n_3(\mathbf{r}'');\mathbf{r}']\phi(|\mathbf{r}'-\mathbf{r}|) \\ &+ \int \rho(\mathbf{r}')\int \rho(\mathbf{r}'')\frac{\delta g_{hs}[n_3(\mathbf{r}'');\mathbf{r}'']}{\delta\rho(\mathbf{r}'')}\phi(|\mathbf{r}'-\mathbf{r}''|)d\mathbf{r}''d\mathbf{r}'\end{aligned} \tag{D.45}$$

where the attractive potential is a square-well potential

$$\phi(r;\lambda) = \begin{cases} -\epsilon_{ff} & \text{if} \quad \sigma \le r < \lambda\sigma \\ 0 & \text{if} \quad r \ge \lambda\sigma \end{cases} \tag{D.46}$$

and the hard sphere radial distribution function is calculated by

$$g(x) = \frac{1}{x}\sum_{n=0}^{\infty} U(x-n)H_n(x) \tag{D.47}$$

where $x = r/\sigma$ and $U(x-n)$ is the unit step function. For the first shell $1 \le x < 2$

$$H_1(x) = a_1\exp[A(x-1)] + a_2\exp[B(x-1)]\cos[C(x-1)] + a_3\exp[B(x-1)]\sin[C(x-1)] \tag{D.48}$$

where

$$A = \frac{-2\eta + z_d}{1-\eta} \tag{D.49}$$

$$B = \frac{-2\eta - z_d/2}{1-\eta} \tag{D.50}$$

$$C = \frac{\sqrt{3}z_s}{2(1-\eta)} \tag{D.51}$$

$$z_d = y_+ - y_- \tag{D.52}$$

$$z_s = y_+ + y_- \tag{D.53}$$

$$y_\pm = (2\eta f)^{1/3}\left[\left(\frac{2\eta^4}{f^2}+1\right)^{1/2} \pm 1\right]^{1/3} \tag{D.54}$$

$$f = 3 + 3\eta - \eta^2 \tag{D.55}$$

$$\eta = (\pi/6)\rho\sigma^3 \tag{D.56}$$

$$a_1 = \frac{-2\eta(1-\eta-3\eta^2) + (1-3\eta-4\eta^2)z_d + (1+\frac{\eta}{2})z_d^2}{3(2\eta^2+z_d^2)(1-\eta)^2} \tag{D.57}$$

$$a_2 = \frac{\eta(2+4\eta-3\eta^2) - (1-3\eta-4\eta^2)z_d + 2(1+\frac{\eta}{2})z_d^2}{3(2\eta^2+z_d^2)(1-\eta)^2} \tag{D.58}$$

$$a_3 = \frac{(1-3\eta-4\eta^2)(4\eta^2+z_d^2) + \eta(2-5\eta^2)z_d}{\sqrt{3}z_s(2\eta^2+z_d^2)(1-\eta)^2} \tag{D.59}$$

for the second and third shells see the work of Chang and Sandler[2]

The second-order attractive term is described by

$$F_2[\rho(\mathbf{r})] = -\frac{1}{4kT}\int \rho(\mathbf{r}')\int \rho(\mathbf{r}'')(1+2\xi n_3^2)[\phi(|\mathbf{r}'-\mathbf{r}''|)]^2 K_{hs}(\mathbf{r}'')g_{hs}[n_3(\mathbf{r}'');\mathbf{r}'']d\mathbf{r}'d\mathbf{r}'' \tag{D.60}$$

and the derivative is

$$\begin{aligned}\frac{\delta F_2[\rho(\mathbf{r})]}{\delta\rho(\mathbf{r})} &= -\frac{1}{2kT}\int \rho(\mathbf{r}')(1+2\xi n_3^2)[\phi(|\mathbf{r}-\mathbf{r}'|)]^2 K_{hs}(\mathbf{r}')g_{hs}[n_3(\mathbf{r}');\mathbf{r}']d\mathbf{r}' \\ &-\frac{1}{4kT}\int \rho(\mathbf{r}')\int \rho(\mathbf{r}'')[\phi(|\mathbf{r}'-\mathbf{r}''|)]^2\frac{\partial n_3}{\partial\rho}\left(4\xi n_3(\mathbf{r}'')K_{hs}(\mathbf{r}'')g_{hs}[n_3(\mathbf{r}'');\mathbf{r}''\right] \\ &+(1+2\xi n_3(\mathbf{r}''))\left[\frac{\partial K_{hs}(\mathbf{r}'')}{\partial n_3(\mathbf{r}'')}g_{hs}[n_3(\mathbf{r}'');\mathbf{r}''] + K_{hs}(\mathbf{r}'')\frac{\partial g_{hs}[n_3(\mathbf{r}'');\mathbf{r}'']}{\partial n_3(\mathbf{r}'')}\right]\Bigg)d\mathbf{r}'d\mathbf{r}''\end{aligned} \tag{D.61}$$

where

$$\xi = \frac{1}{\eta_{con}^2} \tag{D.62}$$

where $\eta_{con} = 0.493$ is the packing fraction where the fluid condenses.

$$K_{hs} = \frac{(1-n_3)^4}{1+4n_3+4n_3^2-4n_3^3+n_3^4} \tag{D.63}$$

$$\frac{\partial K_h s}{\partial n_3} = \frac{4(1-n_3)^3(-2-5n_3+n_3^2)}{(1+4n_3+4n_3^2-4n_3^3+n_3^4)^2} \tag{D.64}$$

The external potential is described by

$$V_{ext} = \phi_{sf}(z) + \phi_{sf}(H-z) \tag{D.65}$$

where

$$\phi_{sf}(z) = 2\pi\epsilon_{sf}\rho_{sol}\sigma_{sf}^2\Delta\left[\frac{2}{5}\left(\frac{\sigma_{sf}}{z}\right)^{10} - \left(\frac{\sigma_{sf}}{z}\right)^4 - \frac{\sigma_{sf}^4}{3\Delta(z+0.61\Delta)^3}\right] \tag{D.66}$$

The expansion and rearrangement of eq. D.2 leads to the following equation

$$\rho(z) = \frac{1}{\Lambda^3}\exp(\mu)\sum_{i=1}^{M}\exp\left[-\beta\psi(z)\right]G^i(z)G^{M+1-i}(z) \tag{D.67}$$

where $\beta = 1/kT$, μ is the chemical potential described in the next section, and

$$\psi(z) = \frac{\delta F_{hs}}{\delta\rho(\mathbf{r})} + \frac{\delta F_{chain}}{\delta\rho(\mathbf{r})} + \frac{\delta F_1}{\delta\rho(\mathbf{r})} + \frac{\delta F_2}{\delta\rho(\mathbf{r})} + V_{ext} \tag{D.68}$$

$$G^i = \int \exp[-\beta\psi(z')]\frac{\Theta(\sigma-|z-z'|)}{2\sigma}G^{i-1}dz' \tag{D.69}$$

where $G^1(z) = 1$

D.2 Bulk Fluid

The chemical potential for the system is calculated by the following equations for a bulk fluid. There are two different densities, the molecular density ρ_M and the segment density ρ_s, where $\rho_s = M\rho_M$. The chemical potential is calculated as the derivative for the Helmholtz free energy with respect to ρ_M.

$$\mu = \frac{\partial A}{\partial\rho_M} \tag{D.70}$$

For the ideal fluid the equations are

$$A_{id,b} = kT\rho_M \left[\ln(\Lambda^3\rho_M) - 1\right] \tag{D.71}$$

$$\mu_{id,b} = kT\ln(\Lambda^3\rho_M) \tag{D.72}$$

For the hard sphere fluid the equations are

$$A_{hs,b} = kT\left[-\rho_0\ln(1-\rho_3) + \frac{\rho_1\rho_2}{1-\rho_3} + \frac{\rho_2^3(\rho_3 + (1-\rho_3)^2\ln(1-\rho_3))}{36\pi\rho_3^2(1-\rho_3)^2}\right] \tag{D.73}$$

$$\begin{aligned}\mu_{hs,b} = MkT\Bigg[&-\ln(1-\rho_3)\frac{\partial\rho_0}{\partial\rho_s} + \frac{\rho_2}{1-\rho_3}\frac{\partial\rho_1}{\partial\rho_s} + \left(\frac{\rho_1}{1-\rho_3}\right.\\ &\left.+\frac{\rho_2^2(\rho_3 + (1-\rho_3)^2\ln(1-\rho_3))}{12\pi\rho_3^2(1-\rho_3)^2}\right)\frac{\partial\rho_2}{\partial\rho_s} + \left(\frac{\rho_0(1-\rho_3)+\rho_1\rho_2}{(1-\rho_3)^2} - \frac{\rho_2^3\ln(1-\rho_3)}{18\pi\rho_3^3}\right.\\ &\left.-\frac{\rho_2^3}{36\pi\rho_3^2(1-\rho_3)} - \frac{\rho_2^3}{36\pi\rho_3^2(1-\rho_3)^2} + \frac{\rho_2^3}{18\pi\rho_3(1-\rho_3)^3}\right)\frac{\partial\rho_3}{\partial\rho_s}\Bigg]\end{aligned} \tag{D.74}$$

where

$$\rho_0 = \rho_s \tag{D.75}$$

$$\rho_1 = R\rho_s \tag{D.76}$$

$$\rho_2 = 4\pi R^2\rho_s \tag{D.77}$$

$$\rho_3 = \frac{4}{3}\pi R^3\rho_s \tag{D.78}$$

For the chain term, the equation is

$$A_{chain,b} = kT\frac{1-M}{M}\rho_0\ln y_{hs,b} \tag{D.79}$$

$$\mu_{chain,b} = kT(1-M)\left(\ln y_{hs,b}\frac{\partial\rho_0}{\partial\rho_s} + \rho_0\frac{\frac{\partial y_{hs,b}}{\partial\rho_2}}{y}\frac{\partial\rho_2}{\partial\rho_s} + \rho_0\frac{\frac{\partial y_{hs,b}}{\partial\rho_3}}{y_{hs,b}}\frac{\partial\rho_3}{\partial\rho_s}\right) \tag{D.80}$$

where

$$y_{hs,b} = \frac{1}{1-\rho_3} + \frac{\sigma\rho_2}{4(1-\rho_3)^2} + \frac{\sigma^2\rho_2}{72(1-\rho_3)^3} \tag{D.81}$$

The first order attractive potentials is described by

$$A_{1,b} = -4\epsilon(\lambda^3 - 1)\eta\rho_s g_{hs,e} \tag{D.82}$$

$$\mu_{1,b} = -4M\epsilon(\lambda^3 - 1)\left(2\rho_3 g_{hs,e} + \rho_3^2 \frac{\partial g_{hs,e}}{\partial \rho_{3,e}} \frac{\partial \rho_{3,e}}{\partial \rho_3}\right) \tag{D.83}$$

where

$$g_{hs,e} = \frac{1 - \rho_{3,e}/2}{(1 - \rho_{3,e})^3} \tag{D.84}$$

$$\rho_{3,e} = \frac{C_1 n_3 + C_2 \rho_3^2}{(1 + C_3 \rho_3)^3} \tag{D.85}$$

$$\frac{\partial \rho_{3,e}}{\partial \rho_3} = \frac{C_1 + 2\rho_3(C_2 - C_1 C_3) - \rho_3 C_2 C_3}{(1 + C_3 \rho_3)^4} \tag{D.86}$$

and

$$\begin{pmatrix} C_1 \\ C_2 \\ C_3 \end{pmatrix} = \begin{pmatrix} -3.16492 & 13.35007 & -14.80567 & 5.70286 \\ 43.00422 & -191.66232 & 273.89683 & -128.93337 \\ 65.04194 & -266.46273 & 361.04309 & 162.69963 \end{pmatrix} \begin{pmatrix} 1/\lambda \\ 1/\lambda^2 \\ 1/\lambda^3 \\ 1/\lambda^4 \end{pmatrix} \tag{D.87}$$

The second-order attractive potential, derived by Zhang[1] is given by

$$A_{2,b} = -2\beta\epsilon^2(\lambda^3 - 1)\left[\rho_s \rho_3 (1 + \xi\rho_3^2) K_{hs} g_{hs,e}\right] \tag{D.88}$$

and the chemical potential is

$$\mu_{2,b} = -2M\beta\epsilon^2(\lambda^3 - 1)\left[4\xi\rho_3^3 K_{hs} g_{hs,e} + (1 + 2\xi\rho_3^2)\left(2\rho_3 K_{hs} g_{hs,e} + \rho_3^2\left[\frac{\partial K_{hs}}{\partial \rho_3} g_{hs,e} + K_{hs} \frac{\partial g_{hs,e}}{\partial \rho_{3,e}} \frac{\partial \rho_{3,e}}{\partial \rho_3}\right]\right)\right] \tag{D.89}$$

D.3 Model Validation

The model has been tested against reference data as it was developed. For a hard sphere system against a hard wall the model was tested against Monte Carlo simulations done by Snook and Henderson.[3] Fig. D.1 shows the model results for reduced densities of $\rho\sigma^3 = 0.57$, 0.755, and 0.81, respectively. For hard sphere chains against a hard wall and for systems with attraction, see Chapter IV.

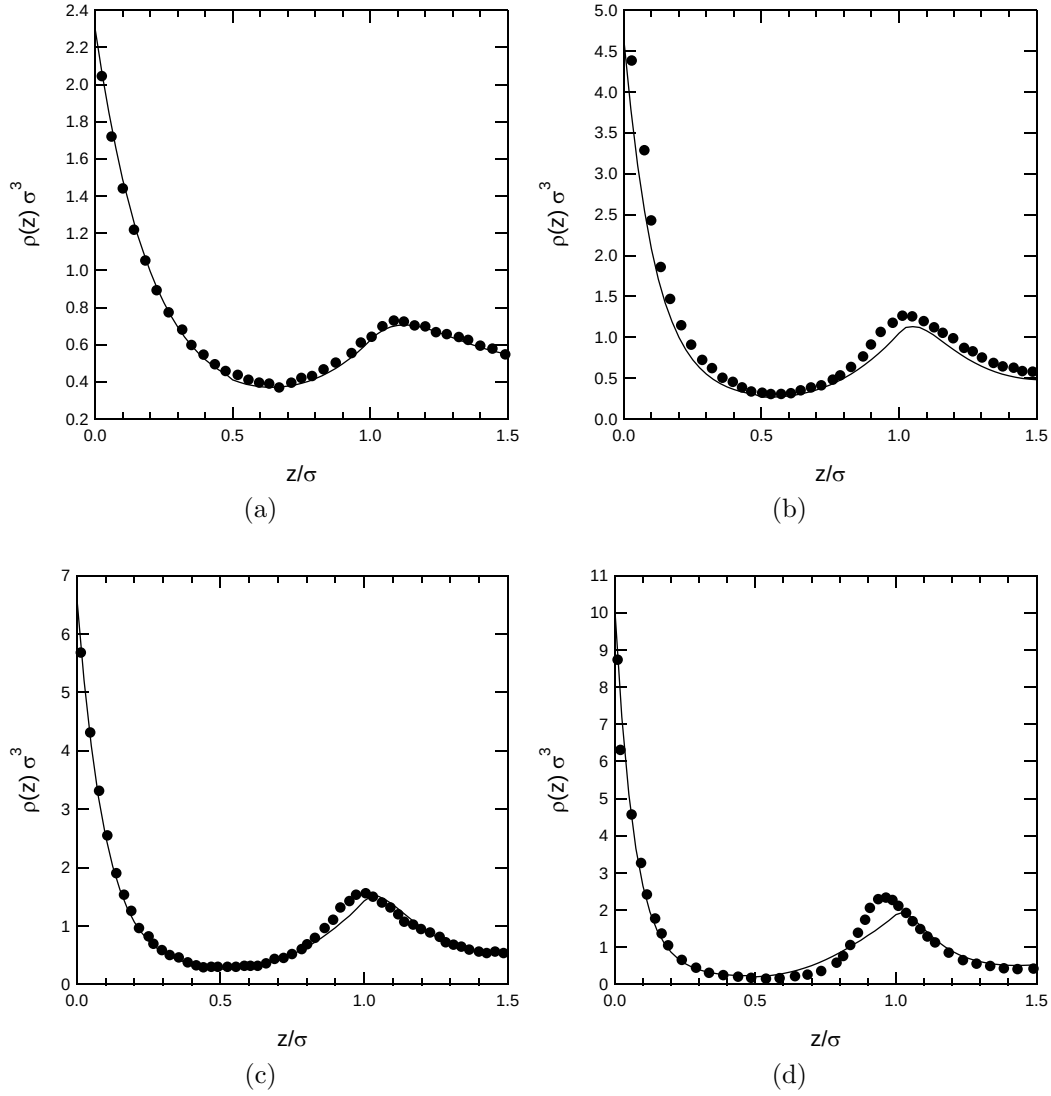

Figure D.1: Hard spheres on hard wall. Monte Carlo simulations are by Snook and Henderson.[3] The reduced densities are (a) 0.57, (b) 0.755, (c) 0.81, (d) 0.91. The solid curve is the model.

References

[1] Zhang BJ. Calculating thermodynamic properties from perturbation theory I. An analytical representation of square-well potential hard-sphere perturbation theory. Fluid Phase Equilibria 1999;154:1–10.

[2] Chang J, Sandler SI. A real function representation for the structure of the hard-sphere fluid. Molecular Physics 1994;81:735–44.

[3] Snook IK, Henderson D. Monte Carlo study of a hard-sphere fluid near a hard wall. J. Chem. Phys. 1978;68:2134–39.

APPENDIX E

ANALYSIS OF ALTERNATIVE NITROGEN ADSORPTION DATA BY SAFT-DFT

Data of Joseph A. Rehrmann, personal communication, 1996. File AS650801.RAW

On the following pages is presented an analysis of an alternative data set for nitrogen at 77 K on BPL activated carbon. Fig. E.1 shows the pore size distribution calculated from the nitrogen istotherm data. Fig. E.2 shows the calculated and measured isotherm for nitrogen on BPL activated carbon. Fig. E.3 shows the calculated pentane isotherm at 25 °C on BPL activated carbon using the calculated pore size distribution.

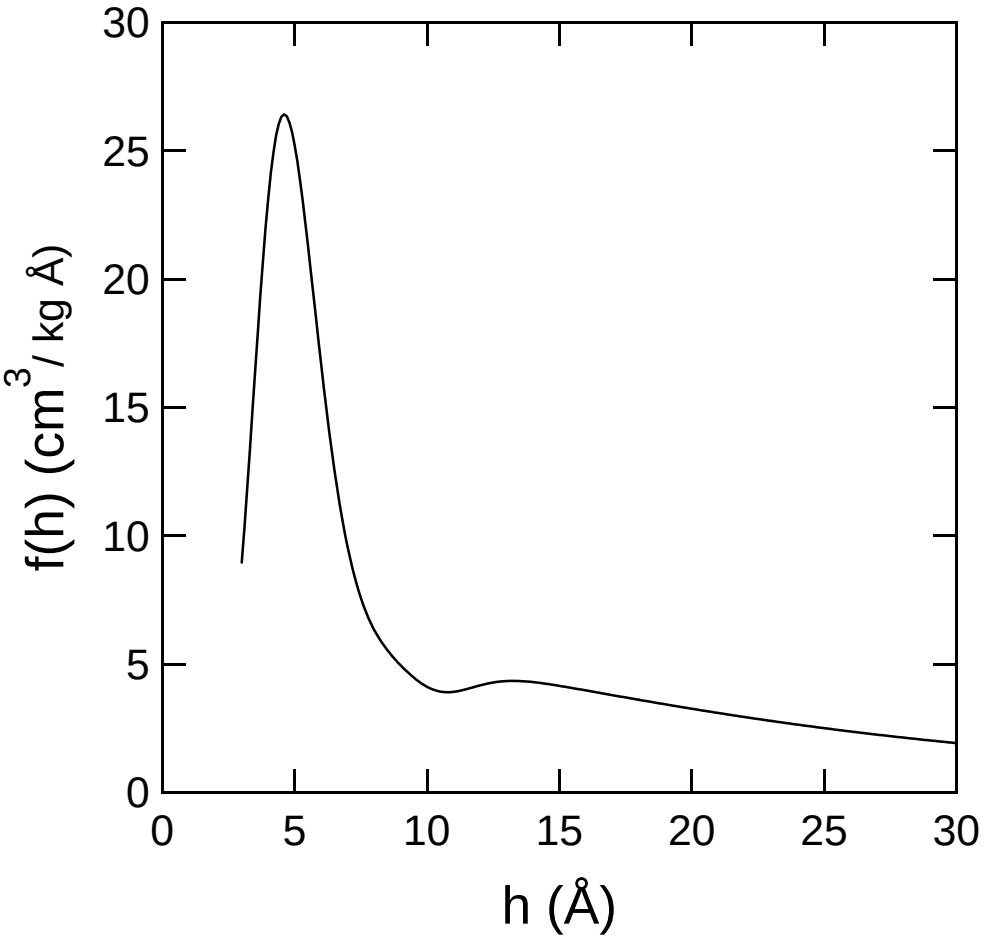

Figure E.1: Pore size distribution calculated from nitrogen density profiles with three modes in eq. 4.37.

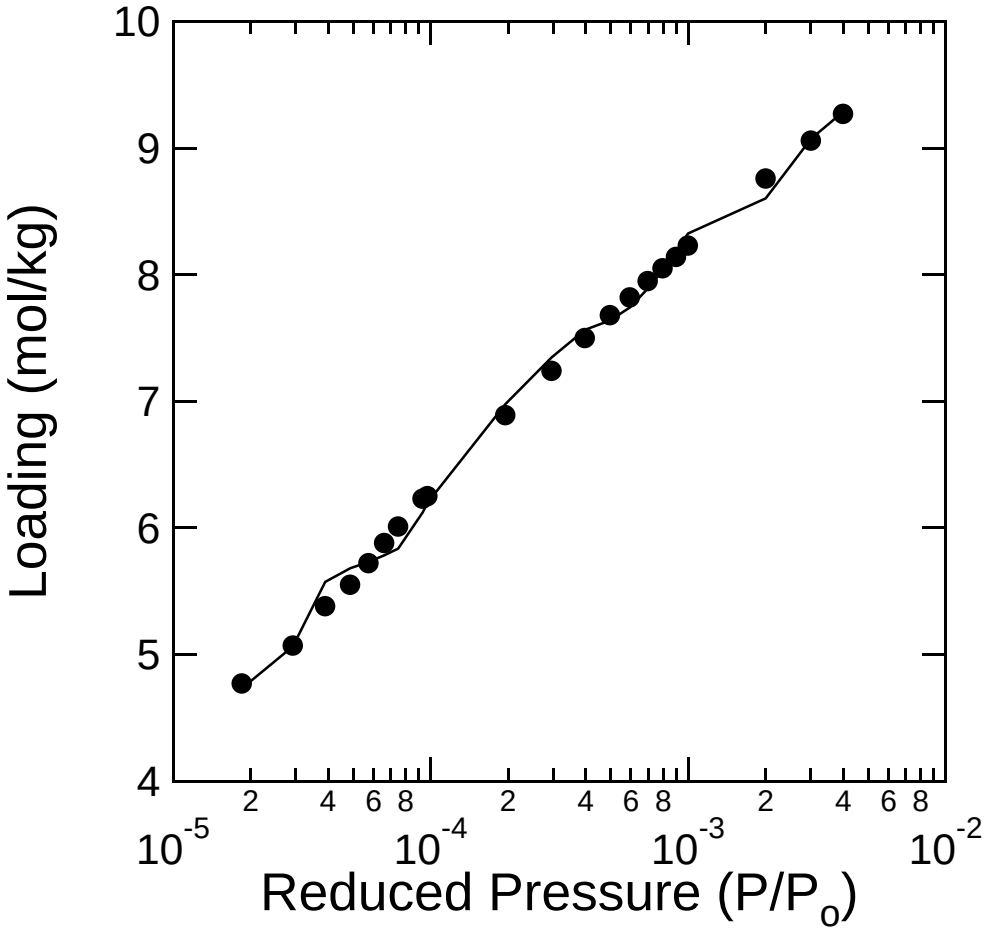

Figure E.2: Nitrogen isotherm at 77 K on BPL activated carbon. Solid line is the calculated isotherm.

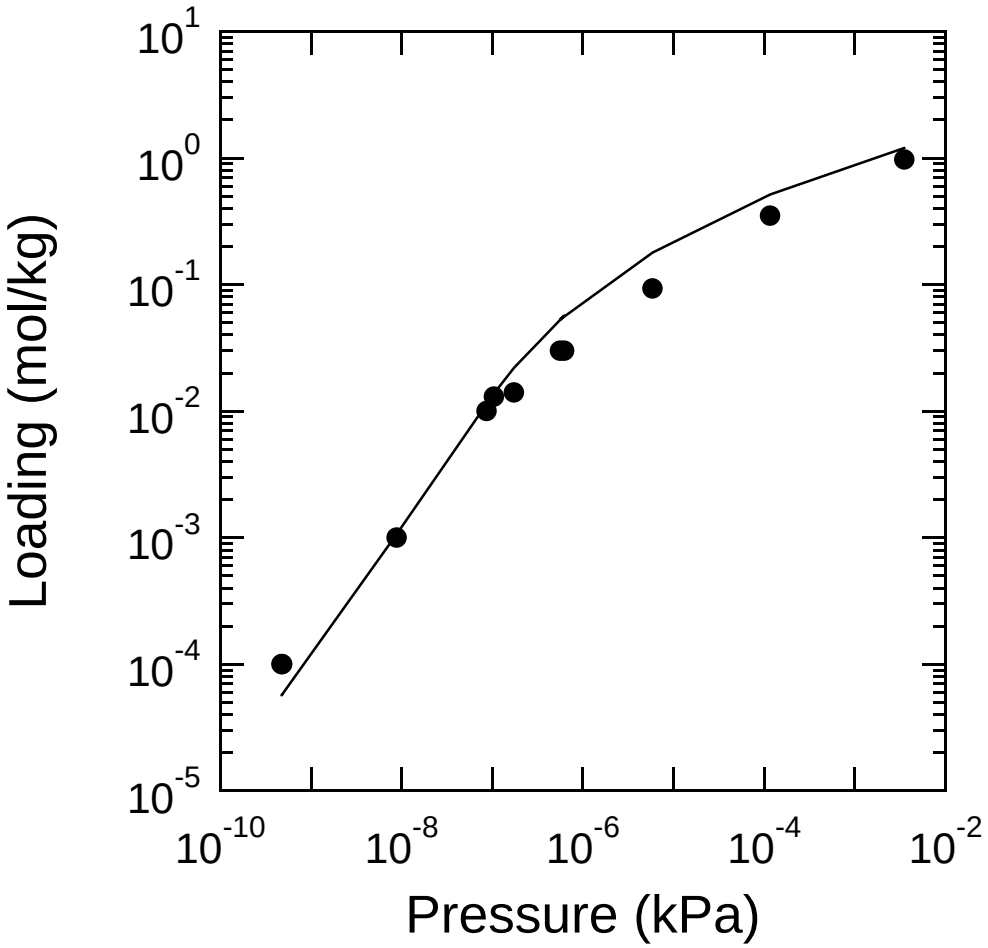

Figure E.3: Calculated n-pentane isotherm at 25°C on BPL activated carbon. The circles are the data from Schindler *et al.*[1] The solid line is the isotherm based on the pore size distribution calculated by nitrogen.

References

[1] B. J. Schindler, L. C. Buettner, and M. D. LeVan, Carbon, **46**, 1285 (2008).